Strain Engineering of Transition Metal Dichalcogenides: A Combined First-Principles and Experimental Study

Edward William Deleu III

Advisor: Professor Saien Xie

Submitted in partial fulfillment

of the requirements for the degree of

Bachelor of Science in Engineering

Department of Electrical and Computer Engineering

Princeton University

April 2026

I hereby declare that this thesis represents my own work in accordance with University guidelines and regulations.

I hereby declare this thesis does not include regulated human subjects research.

I hereby declare this thesis does not include regulated animal subjects research.

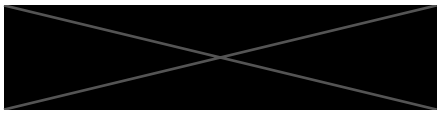

Edward Deleu

I authorize Princeton University to lend this thesis to other institutions or individuals for the purpose of scholarly research.

I further authorize Princeton University to reproduce this thesis by photocopying or by other means, in total or in part, at the request of other institutions or individuals for the purpose of scholarly research.



Edward Deleu

Strain Engineering of Transition Metal Dichalcogenides: A Combined First-Principles and Experimental Study

Edward William Deleu III

Abstract

Strain engineering is a powerful tool for tuning the electronic and optical properties of two-dimensional transition metal dichalcogenides (TMDs). This work presents a combined computational and experimental investigation of strain-induced band structure modulation in monolayer group-VI TMDs. First-principles density functional theory (DFT) calculations are performed for MoS_2, $MoSe_2$, $MoTe_2$, WS_2, and WSe_2 under biaxial strains from -10% to $+10\%$, revealing systematic trends in bandgap evolution according to transition metal and chalcogen elements, as well as strain classification (compressive or tensile). Among these materials, WS_2 exhibits the strongest bandgap tunability, while sulfide-based TMDs demonstrate consistently larger strain tunability compared to their selenide and telluride counterparts. Across materials, the strain-induced bandgap tunability is dominated by conduction-band modulation, with significantly weaker valence-band strain tunability. Complementary uniaxial tensile strain experiments are conducted for WS_2 using both elongation and bending techniques, probing optical bandgaps through photoluminescence (PL) spectroscopy. Using the bending method, a maximum A-exciton energy shift of -48.3meV is achieved; another bending experiment yields a maximal gauge factor of -19.62meV/%. These results clearly establish the viability of strain-induced band structure modulation of monolayer WS_2, validating trends predicted by first-principles calculations. Finally, guided by the computational and experimental findings, a $WS_2/MoSe_2$ heterostructure is proposed as a promising platform for strain-tunable optoelectronic devices, leveraging the favorable band alignment and large tunability difference between materials. This structure exhibits promising strain tunability under both compressive and tensile strains, for both electron and hole carriers. Overall, this work provides a thorough fundamental overview of strain engineering in TMD monolayers, with direct implications for the design of flexible and tunable nanoscale devices.

Acknowledgements

I thank Professor Jie Deng for the helpful discussions and insights for the computational aspects of my thesis, teaching computational atomistic modeling in GEO421. I also thank him for helping troubleshoot my VASP hybrid calculations. Next, I thank my postdoctoral mentor Jaehoon Ji for his intuitive explanations of transition metal dichalcogenides (TMDs), his weekly support of my experimental work, and his help conceptualizing my project. I thank both Jaehoon and Satya Butler for growing TMD samples for my use– without their direct support, none of my experimentation would be possible. I also thank Yin Liang for teaching me the fundamentals of Raman and photoluminescence spectroscopy, guiding me on using our group's custom setup and helping me interpret my results. Finally, I thank my research advisor Professor Saien Xie for guiding me through my thesis, helping immensely to understand the electronic-structure theory and underlying physical phenomena in TMDs. Everyone in the Xie lab has been instrumental to the progress of my thesis project, offering kindness and support.

The simulations presented in this report were performed on computational resources managed and supported by Princeton Research Computing, a consortium of groups including the Princeton Institute for Computational Science and Engineering (PICSciE) and Research Computing at Princeton University.

This research was supported by the Princeton University Andlinger Center's Sustainability Fund during the summer of 2025. This research was also supported by Princeton University's Office of Undergraduate Research senior thesis research funding program through the Round Table Senior Thesis Research Fund.

To my family, friends, and mentors.

Contents

Abstract . . . iii
Acknowledgements . . . iv

1 Introduction **1**

2 Background and Related Work **4**
2.1 DFT Simulation . . . 6
2.2 Experimental Strain Engineering . . . 6

3 Density Functional Theory Simulations **11**
3.1 Computational Approach . . . 11
3.1.1 Convergence Testing . . . 12
3.1.2 Applying Strain . . . 14
3.1.3 Band Structure Calculation . . . 14
3.1.4 Complete Computational Workflow . . . 15
3.2 Results and Discussion . . . 16
3.2.1 Optimized Unstrained Structures . . . 16
3.2.2 PBE Band Structures . . . 18
3.2.3 Hybrid Band Structures . . . 20
3.2.4 Trends in Electronic Band Gaps . . . 24
3.2.5 Band-Edge Evolution Under Strain . . . 29
3.3 Limitations and Future Work . . . 32

4 Experimental Methods **34**
4.1 Transfer Methods . . . 35
4.2 Spectroscopy . . . 41
4.3 Uniaxial Strain . . . 42

5 Experimental Results **45**
5.1 Strain Engineering . . . 49

5.1.1 Elongation 49
5.1.2 Bending 52
5.2 Limitations and Future Work 56

6 Future Applications **59**

7 Conclusion **62**

A Engineering and Industrial Standards **65**

B Density Functional Theory **67**
B.1 Theoretical Foundation 67
B.2 Supplemental DFT Data 71
B.2.1 PBE Band Structures Across Materials 71
B.2.2 MoS_2 Bandgaps vs. Strain Across DFT Methods 77
B.3 Example INCAR Files 78

C Supplemental Experimental Data **81**
C.1 Elongation Data 81
C.2 Bending Data 81

Chapter 1

Introduction

Transition metal dichalcogenides are a class of semiconducting materials that remarkably exhibit direct bandgap characteristics when isolated into monolayer form. Monolayer group-VI TMDs follow an MX_2 structure (with M = Mo or W, X = S, Se, Te) as shown in Fig. 1.1(a). They are direct-bandgap two-dimensional semiconductors, unlike graphene's zero-bandgap nature, making them highly attractive for transistors, photovoltaics, and sensing applications. Their electronic properties are highly sensitive to alloying, external electric fields, and mechanical strain, offering several pathways to precisely and continuously tune device characteristics [1]. The high strain limit of monolayer TMDs, reaching upwards of 12% in MoS_2, provides an effective means to precisely tune both the electronic and optical properties [2, 3].

There has been significant research activity on strain-induced effects on monolayer and few-layer TMDs, but slippage and fracture at just several percent of biaxial or uniaxial strain pose significant experimental difficulty, decreasing the ability for significant strain tunability [3, 8, 9]. Beyond these issues, most past experimental studies have suffered from low strain transfer efficiency, reaching the physical limitations of their strain apparatuses before significant modulation occurs [4, 10]. Fig. 1.2(a) displays the maximum uniaxial strain and band tunability across various experimental methods. The band tunability is given as a quantity called the "gauge factor", indicating the degree of band tunability per percent of strain given in meV per % strain. Across the different polymer substrates and encapsulation methods, the results vary widely, with most studies achieving maximum strains $< 3\%$ and attaining gauge factors significantly lower than theoretically expected. While experiments focus on fabricating high-quality TMD monolayers, improving substrate adhesion, and developing robust strain apparatuses, it also remains important to understand the theoretical capabilities of strain tunability in TMDs according to DFT simulation. Prior *ab initio* work showed that even small strains can widely tune the bandgap of monolayer

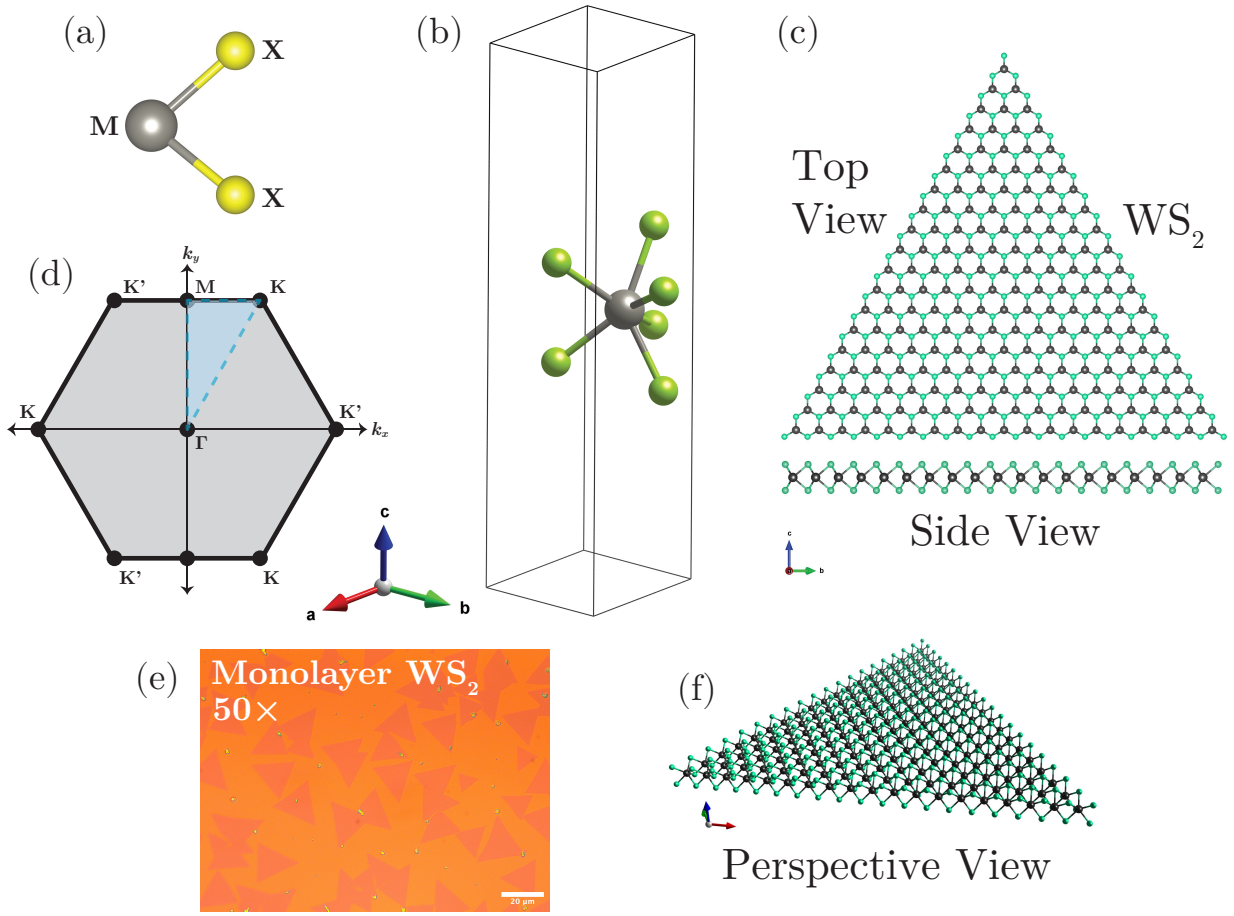

Figure 1.1: Structural diagrams and images of transition metal dichalcogenides. **(a)** Diagram of an MX_2 molecule. **(b)** Primitive unit-cell of an MX_2 monolayer with a large vacuum spacing. **(c)** Top and side schematic views of a zig-zag chalcogen edge-terminated MX_2 triangular flake. **(d)** Brillouin zone of the 1H crystal structure, with the irreducible Brillouin zone outlined in blue along with the high-symmetry points Γ, M, K, K′. **(e)** Optical microscope image of monolayer WS_2 flakes taken at 50× magnification. Scale bar is $20\mu m$. **(f)** Perspective view diagram of a WS_2 triangular flake.

TMDs, trigger direct-to-indirect bandgap transitions, and eventually cause a semiconductor to metal transition at large enough strain levels [11–13]. Past studies predict that in monolayer MoS_2, a 2% uniaxial tensile strain can drive a direct to indirect bandgap transition, while a 10% biaxial tensile strain can close the gap altogether. Under biaxial tensile strain, the bandgap of MoS_2 decreases by approximately 105 meV per % strain according to an experimental study [14]. Biaxial compressive strain also modifies band edges, generally requiring larger strain magnitude to induce similar modulation [13]. Fig. 1.2(b-f) display various methods of applying biaxial strain on TMD materials, including nano-indentation, physically deforming a cruciform substrate, bulging a polymeric substrate with pressurized

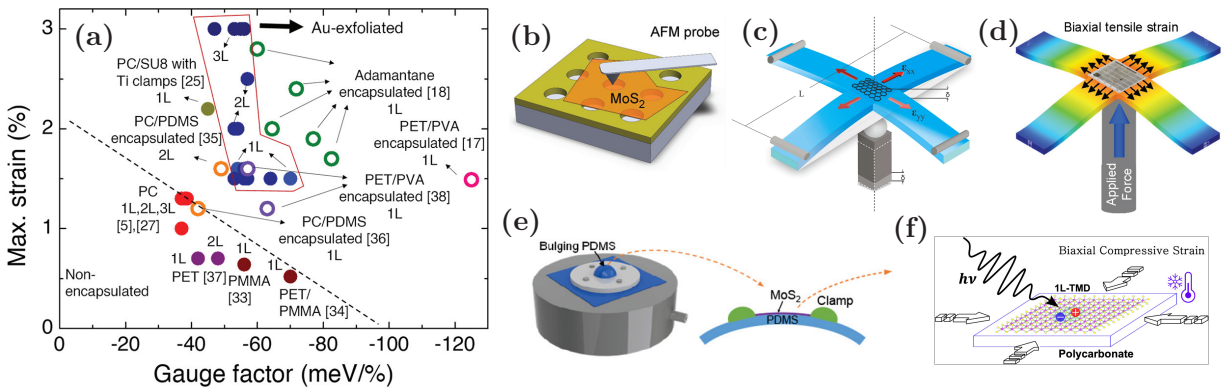

Figure 1.2: Survey of experimental strain results and methods for TMD materials. **(a)** Summary of the maximum strain and gauge factors reported on the A-exciton of MoS_2 upon applying uniaxial strain with photoluminescence spectroscopy, adapted from [4]. **(b)** Experimental method of applying strain on a suspended film of MoS_2 through nano-indentation with an AFM probe, reproduced from [2]. **(c-d)** Experimental method of biaxially straining TMD films by physical deformation of a cruciform sample, reproduced from [5] and [6]. **(e)** Experimental method of biaxially straining TMDs by bulging a polymer substrate with pressurized air, reproduced from [7]. **(f)** Experimental method of applying biaxial strain through the mismatch of thermal expansion coefficients with a polycarbonate substrate, reproduced from [8].

air, and taking advantage of thermal contraction and expansion. While many previous studies have explored strain effects in isolated TMD monolayers, a unified and systematic comparison across multiple compounds with a consistent computational approach and exploration of corrections still provides significant value.

This project launches a multi-faceted investigation of strain engineering across TMDs, exploring both computational and experimental behavior. Computationally, this project explores biaxial strain across five of the most widespread semiconducting TMDs, exploring their electronic behavior and band structures using VASP. Various DFT methods are explored to qualitatively determine the best way to model monolayer TMDs under strain. Experimentally, this work explores both elongation and bending methods for applying uniaxial tensile strain on WS_2, using photoluminescence (PL) spectroscopy to probe its strain tunability.

Chapter 2

Background and Related Work

Strain engineering may generally be defined as the mechanical deformation of a functional material to improve one or more of its properties [15]. Semiconductor strain engineering has seen significant popularity, with moderate strain levels able to improve carrier transport and therefore current in transistor devices. This field first saw attention with strained silicon transistors. Initial experiments grew silicon on SiGe substrates: since the SiGe substrates have a larger lattice constant than crystalline silicon, a biaxial compressive strain is imposed epitaxially on the silicon layer. By controlling the germanium content of the substrate, the lattice constant and hence strain can be effectively modulated. This construct allows for electron and hole mobility enhancement in excess of 30% in the silicon layer, thereby allowing improved device performance [15]. Ever since the 1990s, this discovery has fueled research interest in strain engineering, a crucial principle underlying modern semiconductor technologies.

Transition metal dichalcogenides (TMDs) have long been used as an inorganic equivalent of graphite, often used as a high-temperature lubricant. Research interest in TMDs sparked in 2010 when researchers first discovered the tunable bandgaps of TMDs with respect to sample thickness [16]. In addition to this discovery, the researchers found that the 1.3eV indirect bandgap of bulk MoS_2 transitions to a 1.9eV direct optical bandgap in monolayer form. In general, monolayer TMDs exhibit considerable electronic bandgaps, in the range from $1.6-2.5$eV [1]. Considering that visible light spans the range roughly between $1.6-3$eV, TMDs are highly attractive semiconductors for tunable optical and nanoelectronic applications.

Fig. 1.1(e) displays an optical microscope image of monolayer WS_2 flakes, displaying their characteristic equilateral triangular shape. This shape is dictated by the thermodynamics of their growth environment, specifically the ratio of gaseous precursors during the chemical vapor deposition (CVD) fabrication process [1]. Schematic views of TMD flakes are shown

in Fig. 1.1(c) and Fig. 1.1(f), displaying their typical hexagonal 1H lattice structure with space group 187 and trigonal prismatic coordination. This is the most thermodynamically stable structure under ambient conditions for MoS_2, $MoSe_2$, $MoTe_2$, WS_2, and WSe_2 [1, 12]. However, TMDs such as $MoTe_2$ may exist meta-stably in alternative crystal structures such as the 1T (octahedral coordination) or distorted 1T' (distorted octahedral coordination) phases, exhibiting metallic behavior, although these are beyond the scope of this work. It is important to note that WTe_2's most stable phase is not the 1H semiconducting structure, but rather the distorted 1T' structure (sometimes referred to as T_d) [17]: this material is hence excluded from analysis in this work. While past studies have also reported strain-mediated phase transitions in TMDs, this work considers only TMDs in the 1H structure [12].

Fig. 1.1(b) displays an example of the primitive unit-cell for monolayer 1H TMDs, with the corresponding Brillouin zone in Fig. 1.1(d) with the wedge-shaped irreducible zone highlighted in blue. This primitive cell has a large vacuum spacing in the z-direction, necessary to separate periodic monolayers of the two-dimensional structure during simulations. Under biaxial strain, the TMD lattice is stretched in the lateral direction, preserving the lattice symmetry. Consequently, the Brillouin zone and irreducible path are also preserved, allowing for simple analysis of band structures under different strains along the $\Gamma - \mathrm{M} - \mathrm{K} - \Gamma$ reciprocal lattice path. Monolayer TMDs lack inversion symmetry and are therefore non-centrosymmetric, resulting in a valley degree-of-freedom associated with the in-equivalent K and K′ Brillouin zone points. However, time-reversal symmetry (TRS) is preserved, enforcing the relation $E(\vec{k}, \uparrow) = E(-\vec{k}, \downarrow)$. In the hexagonal Brillouin zone $K' \equiv -K$ (modulo a reciprocal lattice vector), so TRS enforces that:

$$E(\mathrm{K}, \uparrow) = E(\mathrm{K}', \downarrow). \tag{2.1}$$

In the presence of spin-orbit-coupling where the electronic bands are spin-split at each valley, the spin ordering is flipped between the K and K′ points. The energy eigenvalues are otherwise equivalent between these high-symmetry points, so band structure calculations along $\Gamma - \mathrm{M} - \mathrm{K} - \Gamma$ fully capture the electronic dispersion and explicit inclusion of K′ is redundant.

Since uniaxial strain breaks the symmetry of the Brillouin zone, plotting band structures along high-symmetry paths becomes significantly more complex. As such, this work only focuses on DFT simulation of biaxially strained materials.

2.1 DFT Simulation

Density Functional Theory (DFT) simulations are the leading methodology for first-principles modeling of TMD behavior. Leading software packages include Vienna *ab initio* Simulation Package (VASP) and Quantum Espresso. VASP version 6.4.3 [18–21] and the helper-software VASPKIT [22, 23] are primarily utilized in this work. VASP is a widely used first-principles electronic-structure software based on density functional theory (DFT), employing plane-wave basis sets and projector-augmented-wave (PAW) potentials to efficiently treat core–valence interactions and solve the Kohn-Sham equations. DFT provides a quantum-mechanical description of materials using the electron density rather than complex many-body wavefunctions, allowing accurate predictions of structural and electronic properties without using system-specific empirical parameters. This makes DFT particularly suitable for systematically studying how external perturbations such as strain modify the electronic band structures of monolayer TMDs. A more thorough theoretical discussion of DFT and its fundamental limitations is provided in Appendix B.

VASP requires the following input files for running simulations:

- **INCAR**: The central input file for VASP simulations, describing exactly what simulations to perform and how. This file specifies the exact algorithms and input parameters used for calculation.
- **POSCAR**: The file defining the atomic positions and lattice vectors, constructing the unit-cell.
- **POTCAR**: The file defining the pseudo-potential for each atomic species present in simulation.
- **KPOINTS**: The file specifying the reciprocal-space points used to sample the Brillouin zone. The most common scheme is a Γ-centered mesh.

A simulation is run by calling vasp_gam, vasp_std, or vasp_ncl for gamma-only, standard, or non-collinear calculations, respectively, from the directory containing the above input files.

2.2 Experimental Strain Engineering

There has been significant work in experimental strain engineering of TMD monolayers, especially under uniaxial tensile strain. There have been far fewer studies of biaxial strains

due to the complex apparatuses necessary. Furthermore, there are limited results studying strain in TMD heterostructures due to the associated fabrication difficulties.

Experimental studies have shown that monolayer TMDs have Young's moduli in the $200 - 300$ GPa range [24]. Past work has shown that strain is most efficiently transferred to TMDs from higher Young's moduli substrates, for example the more rigid polycarbonate (PC) instead of the elastomeric polydimethylsiloxane (PDMS) [9]. This is supported by both finite-element simulations and experimental works. More specifically, PDMS substrates are calculated to only transfer several percent of actual strain to TMD flakes, often estimated around 10%, while substrates with moduli in the GPa range are predicted to have significantly improved transfer efficiency greater than 75% [25, 26]. This behavior is logical: the much stiffer TMDs may prevent strain transfer on very flexible substrates which can easily deform, whereas stiffer substrates will less easily allow this deformation and will transfer a higher degree of strain to the TMD.

Table 2.1 summarizes experimentally observed uniaxial tensile strain tunability of various TMDs measured using photoluminescence (PL) spectroscopy, noting the growth, transfer, and strain methods utilized. Across materials and methods, most uniaxial strain experiments tend to observe maximum PL red-shifts between $30 - 100$meV, with a few experiments reaching much higher strain levels and attaining up to 253meV of modulation. A majority of studies only attain strain levels below $\approx 2.5\%$ before slippage or strain relaxation, limiting the maximum strain tunability. The table demonstrates that methods utilizing encapsulation polymers, whether fully sandwiching the TMD layer or simply embedding it within a polymer matrix, greatly improves the overall strain transferability. The results also corroborate that experiments utilizing PDMS-based substrates suffer from quite poor strain transfer, compared to more rigid and higher Young's moduli substrates which tend to attain the best strain modulation. Finally, this table demonstrates that across the strain engineering literature, bending has been the primary method of applying strain. This is logical since it is relatively easy to bend samples without a complex apparatus: elongation and micro-electromechanical systems (MEMS) require far more complex apparatuses.

One limitation of the current strain engineering literature is the reported gauge factors. Across methods, different papers calibrate their strains in different ways (or lack calibration altogether). For example, with the bending method, different papers sometimes utilize different models to extract the actual strain from the radius of curvature or other physical measurements [3, 30]. Some studies account for non-ideal strain-transfer, while others utilize the nominal applied strain. Very few studies calibrate their strain through optical measurements of calibration patterns [30]. Finally, it is clear that the experimental gauge factors significantly vary between reported literature even for the same materials and similar

Table 2.1: Summary of reported A-exciton photoluminescence peak shifts in monolayer TMDs under **uniaxial tensile strain**, comparing: TMD fabrication methods, experimental strain application, maximum applied strain, and corresponding energy modulation, along with reported gauge factors (defined as $dE/d\varepsilon$) in units of meV/%. Encapsulation polymers shown in blue denote materials that have been spin-coated onto TMDs, although not explicitly sandwiching TMD layers. Values shown in red denote estimates inferred from reported data.

Material	Author	Growth	Substrate	Encapsulated?	Method	Gauge Factor	Max Strain (%)	Max Modulation (meV)
MoS_2	Z. Li [10]	Exfoliated	PVA	PVA	Bending	-125	1.49	-193
	F. Carrascoso [27]	Exfoliated	PC	Adamantane	Bending	-58.9	2.8	-164.9[a]
	H. Conley [28]	Exfoliated	PC/SU-8	Ti Clamps	Bending	-45	2.2	-99
	J. Christopher [29]	CVD	MEMS	PPC	MEMS	-38	1.3	-49.4
	F. Carrascoso [30]	Exfoliated	PC	✗	Bending	-37.3	1.3	-48.5
	X. He [31]	Exfoliated	PET	PMMA	Bending	-56	0.64	-35.8
	I. Niehues [32]	Exfoliated	PC	PDMS	Bending	-28	1.26	-35.3
	K. He [33]	Exfoliated	PMMA	✗	Bending	-64	0.52	-33.3
	A. John [34]	Exfoliated	PI	✗	Bending	-78	0.4	-31.2
	F. Carrascoso [27]	Exfoliated	PC	Adamantane	Bending	-70.2	0.33	-23.2
	F. Carrascoso [27]	Exfoliated	PC	✗	Bending	-37.1	0.52	-19.3
	Z. Liu [26]	CVD	PDMS	✗	Elongation	-3	4.8	-15
$MoSe_2$	I. Niehues [32]	Exfoliated	PC	PDMS	Bending	-38	0.98	-37.2
	J. Island [35]	Exfoliated	PC	PDMS	Bending	-27	1.1	-29.7
	L. Mennel [36]	Exfoliated	PEN/SU-8	✗	Bending	-54.8	0.5	-27.4
	F. Carrascoso [30]	Exfoliated	PC	✗	Bending	-41	0.65	-26.7
WS_2	Z. Li [10]	CVD	PVA	PVA	Bending	-43	5.68	-253
	S. Zhao [37]	Exfoliated	PET/Glue	PVA	Bending	-41	2.5	-102.5
	M. Tweedie [38]	CVD	PEN	✗	Bending	-20	2.5	-50
	I. Niehues [32]	Exfoliated	PC	PDMS	Bending	-50	0.95	-47.5
	F. Carrascoso [30]	Exfoliated	PC	✗	Bending	-44	1.04	-45.8
	Y. Wang [39]	CVD	PET	✗	Elongation	-11.3	4	-45.2
	J. Chen [40]	CVD	Nanowire (OFN)	✗	Elongation	-30	1.35	-40.5
	F. Colangelo [41]	CVD	Graphene	✗	MEMS	–74	0.54	-40
	L. Mennel [36]	Exfoliated	PEN/SU-8	✗	Bending	-61.2	0.5	-30.6
	X. He [31]	Exfoliated	PET	PMMA	Bending	-46	0.64	-29.4
	F. Wang [42]	Exfoliated	PMMA/SU-8	✗	Bending	-58.7	0.42	-24.7
	Q. Zhang [43]	CVD	PDMS	✗	Elongation	-1.25	16	-20
WSe_2	Z. Li [10]	Exfoliated	PVA	PVA	Bending	-109	1.70	-176
	Z. Li [10]	CVD	PVA	PVA	Bending	-53	2.56	-137
	R. Schmidt [44]	Exfoliated	PC	PDMS	Bending	-54	1.4	-75.6
	I. Niehues [32]	Exfoliated	PC	PDMS	Bending	-49	1.48	-72.5
	W. Hu [45]	Exfoliated	PC	✗	Bending	-64.3	0.65	-41.8
	L. Mennel [36]	Exfoliated	PEN/SU-8	✗	Bending	-53	0.3	-15.9

[a]This method utilizes differential reflectance rather than photoluminescence spectroscopy.

methodologies. As such, the maximum strain tunability is a more consistent metric for comparison and will henceforth be the primary metric for benchmarking experimental work.

Table 2.2 summarizes experimentally observed biaxial tensile strain tunability of various TMDs measured using PL spectroscopy. While the literature on biaxial strain is less expansive than with uniaxial strain, there are a wider variety of strain application methods. One of the leading methods for applying biaxial strain is by deflecting or bending a plastic cruciform with a TMD sample mounted at its center. Another common strain method is

Table 2.2: Summary of reported A-exciton photoluminescence peak shifts in monolayer TMDs under **biaxial tensile strain**, comparing: TMD fabrication methods, experimental strain application, maximum applied strain, and corresponding energy modulation, along with reported gauge factors (defined as $dE/d\varepsilon$) in units of meV/%. Values shown in red denote estimates inferred from reported data.

Material	Author	Growth	Substrate	Encapsulated?	Method	Gauge Factor	Max Strain (%)	Max Modulation (meV)
MoS_2	D. Lloyd [46]	Exfoliated	PC	✗	Bulge	-92	5.6	-515.2
	R. Yang [7]	CVD	PDMS	✗	Bulge	-41	9.4	-90
	F. Carrascoso [9]	Exfoliated	Mylar	✗	Deflection	-90.2	0.59	-53.2[a]
	R. Frisenda [25]	Exfoliated	PP	✗	Thermal	-51	0.9	-45.9[a]
	A. Michail [47]	Exfoliated	PMMA	PMMA	Deflection	-124	0.50	-62
	G. Plechinger [14]	Exfoliated	PDMS	✗	Deflection	-105	0.20	-60
	A. Michail [47]	CVD	PMMA	PMMA	Deflection	-76	0.50	-38
$MoSe_2$	S. Patel [48]	PVD	SiO_2	✗	Thermal	-103	0.73	-75.2
	F. Covre [49]	Exfoliated	SiO_2/hBN	PMMA	Bubble	-54	1.3	-70.2
	R. Frisenda [25]	Exfoliated	PP	✗	Thermal	-33	0.9	-29.7[a]
WS_2	J. Zhou [50]	Exfoliated	PET	✗	Bending	-85	3.7	-220
	S. Roy [51]	Exfoliated	PC	✗	Deflection	-179	0.51	-94
	A. Michail [52]	CVD	PMMA	PMMA	Deflection	-130	0.67	-87.1
	R. Frisenda [25]	Exfoliated	PP	✗	Thermal	-94	0.9	-84.6[a]
	G. Kourmoulakis [53]	Exfoliated	Graphite	PMMA	Deflection	-130	0.45	-50
	J. Yang [6]	CVD	PEN	AlO_x	Deflection	-120	0.23	-27.6
WSe_2	B. Aslan [54]	CVD	Quartz	✗	Bulge	–	–	-147
	G. Ahn [55]	CVD	Silica	✗	Thermal	-102	1.	-102
	R. Frisenda [25]	Exfoliated	PP	✗	Thermal	-63	0.9	-56.7[a]
	S. Roy [56]	Exfoliated	PC	✗	Deflection	-96	0.51	-53

[a]These works utilize differential reflectance rather than photoluminescence spectroscopy.

to induce a bulge in a TMD film with pressurized gas, although far more complex since a strong seal must be accomplished. There also exists methods of straining TMDs by forming bubbles in the monolayers, as well as taking advantage of mismatches in thermal expansion coefficients to strain TMD films. Along with the greater variety in strain methods, there is also a greater variety in polymer substrates used. Still, the higher Young's modulus substrates such as PC and PET tend to have the best strain transfer efficiency and highest gauge factors.

Overall, the biaxial tensile strain gauge factors and maximum modulations tend to be higher than the uniaxial results. For example, for WS_2 the median maximally achieved A-exciton red-shift from Table 2.1 is 42.85meV, whereas for biaxial strain it is 85.85meV from Table 2.2. This indicates an approximate factor of 2× between the strain tunability of uniaxial and biaxial strain for monolayer TMDs; this aligns well with values reported in past literature for gauge factors, supported by both experimental and computational methods [57]. The median gauge factor reported in Table 2.2 for biaxial strain on WS_2 is -130meV/%, compared to the much smaller -43.5meV/% for the corresponding uniaxial gauge factor. Computing and comparing medians from an assortment of past experimental

works is imperfect, but this displays the fundamental differences between uniaxial and biaxial strain tunability. This also aligns with intuitive expectations: biaxial strain induces a larger degree of deformation of the unit-cell, bringing larger electronic structure modulation by more significantly changing orbital overlap and interactions.

The biaxial strain experimental data suffers from the same inconsistencies in gauge factor and strain-value reporting as with uniaxial strains. It is also important to note that the experimentally achieved maximum strains are very low in the biaxial tensile regime, primarily under 1%. This limitation is primarily a consequence of biaxial strain apparatuses and methodologies. While this section has focused on experimentally applying tensile strains, there is of course also a body of literature for compressive strains. Due to the associated difficulties of applying compressive uniaxial and biaxial strains, the results are far more limited, especially in terms of the maximum applied strains which tend to be under 1%.

Chapter 3

Density Functional Theory Simulations

DFT simulations are performed to generate electronic band structures for MoS_2, $MoSe_2$, $MoTe_2$, WS_2, and WSe_2 from $-10\% \rightarrow 10\%$ biaxial strain in 1% increments. Band structures are calculated along a consistent reciprocal-lattice path to allow for straightforward comparison between materials and strain levels. Results are evaluated for various DFT methodologies to determine the workflow that matches best with experimental TMD strain studies, both qualitatively and quantitatively.

3.1 Computational Approach

A multi-step computational pipeline is implemented for simulating TMDs under biaxial strain using VASP. The first step is to obtain relaxed, unstrained structures for the full set of TMDs under study. TMD structures are first downloaded from the Materials Project database [58] in the 2H (bi-layer) form with the .CIF file format; mp-2815, mp-1634, mp-602, mp-224, and mp-1821. An example 2H structure is shown in Fig. 3.1. These structures are subsequently converted into VASP POSCAR's using VESTA, and the bi-layer atoms are removed to yield the 1H (monolayer) structure. Sufficient vacuum padding is then added using VASPKIT 922, ensuring that the atoms remain centered in the z-direction while adding padding/2 to the unit-cell above and below the monolayer.

All structural relaxation is performed using VASP with projector-augmented-wave (PAW) pseudo-potentials and with the Perdew-Burke-Ernzerhof (PBE) exchange-correlation functional. Electronic occupations are treated using Gaussian smearing (ISMEAR=0) with a smearing width of 0.05eV (SIGMA=0.05). The energy tolerance is set to 1μeV (EDIFF = 10^{-6}) for the convergence of the electronic SCF loop and electronic wavefunction. For

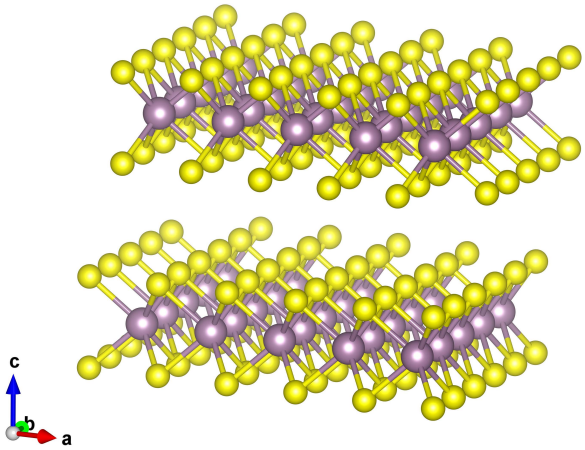

Figure 3.1: The bi-layer 2H structure of MoS_2 retrieved from the Materials Project database, mp-2815, visualized in VESTA. The magenta atoms correspond to molybdenum and the yellow atoms correspond to sulfur.

structural optimization, the force tolerance is set to 0.01 eV $Å^{-1}$ (EDIFFG=-10^{-2}), and ionic relaxation concludes when the norms of all forces are below this criterion. All VASP simulations are run on Princeton's Della and Adroit clusters, using vasp_ncl with ISPIN= 2 for calculations including spin-orbit coupling (SOC) and vasp_std with ISPIN= 1 for non-SOC calculations. Across the five materials and twenty-one strain levels per material computed within this work, 118, 275.63 CPU-hours of runtime are utilized, primarily consumed by the hybrid band structure calculations. Hypothetically, running all computations sequentially with 128 CPU-cores, this corresponds to 38.5 days of non-stop computing. However, jobs are largely parallelized, massively reducing the actual runtime necessary for this work.

3.1.1 Convergence Testing

To obtain sufficiently-relaxed structures, convergence testing is first performed to determine the optimal set of VASP input parameters for structural and electronic optimization. An initial relaxed structure of MoS_2 is obtained with over-estimated parameters, i.e., ENCUT = 900eV, a $20 \times 20 \times 1$ reciprocal-space mesh, and a vacuum spacing of 20Å. Then, a single parameter is varied while the other parameters are held constant at a reasonable level, allowing a plot of internal-energy vs. the given parameter to find the converged parameter value. For the electronic optimization, as shown in Fig. 3.2a, the planewave cut-off energy converges to $\delta < 1$meV by ENCUT = 700eV. The reciprocal-space mesh converges to $\delta <$ 0.1meV by a resolution of $12 \times 12 \times 1$. As Fig. 3.2b depicts, finer reciprocal-space meshes yield improved electronic convergence; however, this level of precision is not required, so the $12 \times 12 \times 1$ grid is chosen to maintain computationally efficient calculations. For geometric

convergence with respect to the vacuum spacing, the energy converges by 10Å. While this should be sufficient to reduce periodic-image interactions, a vacuum spacing of 15Å is chosen for convergence within $\delta < 0.5$meV. This aligns with past literature simulating TMDs using VASP [13]. It is important to note that the total unit-cell height is the vacuum spacing *plus* the monolayer TMD thickness, not solely the vacuum spacing.

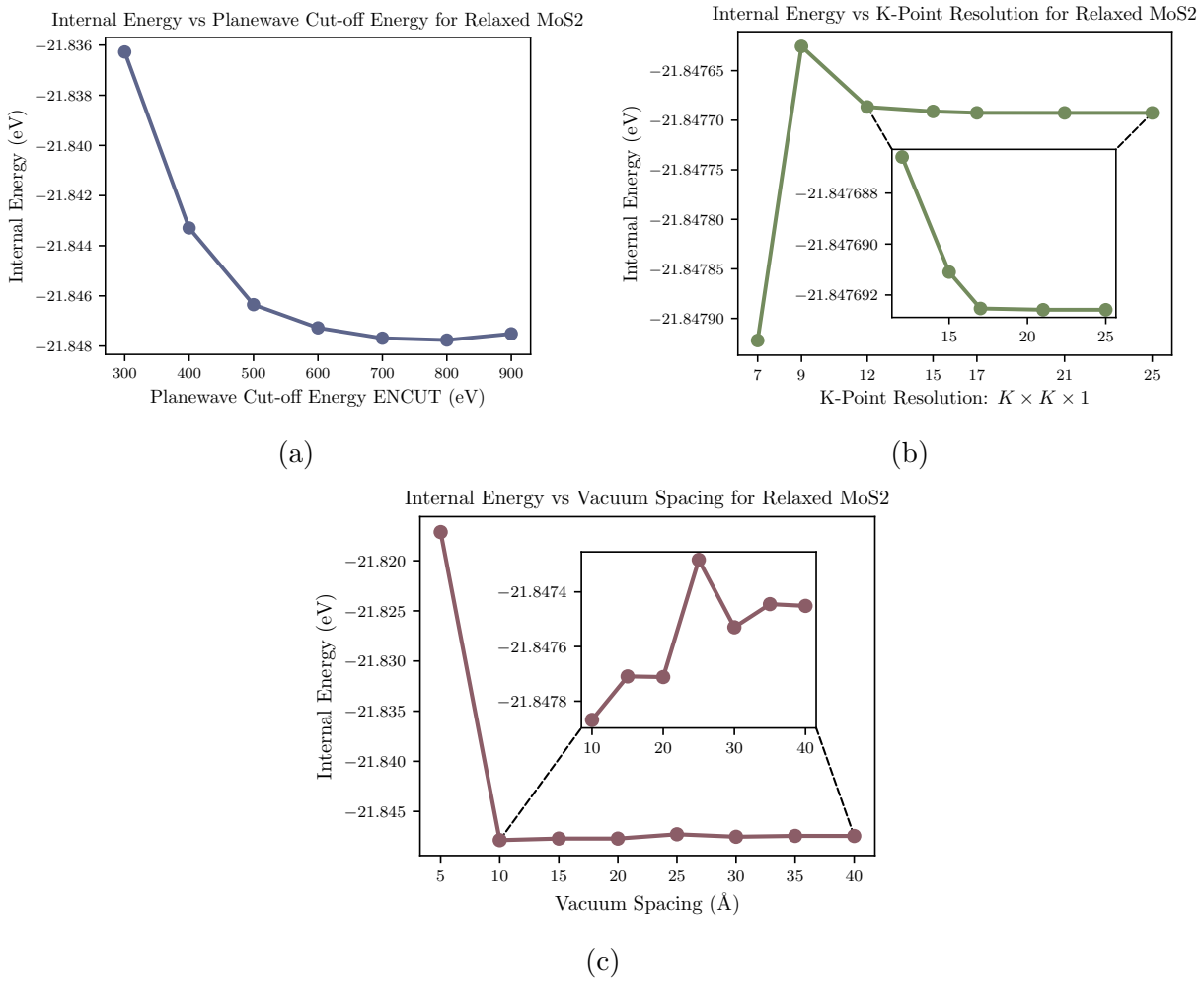

Figure 3.2: Convergence testing of VASP input parameters for structural relaxation of MoS_2. **(a)** Convergence of planewave cut-off energy (ENCUT), using a $12 \times 12 \times 1$ reciprocal-space mesh, a 15Å vacuum spacing, and NSW= 0. **(b)** Convergence of reciprocal-space mesh resolution, using ENCUT = 700eV, a 15Å vacuum spacing, and NSW= 0. **(c)** Convergence of z-direction vacuum spacing, using ENCUT = 700eV, a $12 \times 12 \times 1$ K-mesh, and NSW= 100 steps.

3.1.2 Applying Strain

Once relaxed, unstrained structures are obtained for the full set of materials using ISIF= 4 with lattice vectors and atomic positions as degrees-of-freedom, strain may be applied. Biaxial strain corresponds to simultaneously stretching (or compressing) the in-plane lattice-vectors of the unit-cell. Importantly, the POSCAR must specify atomic positions in "direct" mode such that the positions are specified as a fraction of the lattice vectors and not absolute coordinates. A script is used to methodically generate strained POSCARs by applying the transformation:

$$\vec{a} \rightarrow (1+\varepsilon)\vec{a};\ \vec{b} \rightarrow (1+\varepsilon)\vec{b};\ \vec{c} \rightarrow \vec{c}, \tag{3.1}$$

where $\vec{a}$ and $\vec{b}$ are the in-plane lattice vectors, $\vec{c}$ is the out-of-plane lattice vector, and ε is the strain, from $\varepsilon = -0.1$ (10% compressive strain) to $\varepsilon = 0.1$ (10% tensile strain). Once biaxially strained structures are obtained, structural relaxation must once-again be performed. This relaxation must use ISIF= 2 such that the lattice vectors are fixed and the atomic positions are the only degree-of-freedom, preserving the applied strain.

3.1.3 Band Structure Calculation

VASP band structure calculations require fully standardized primitive-cells to ensure proper identification of symmetries for band-path generation. All structural relaxations are performed on primitive cells from the start, which are verified to be preserved after relaxation. While structures should remain standardized, VASPKIT 923 is run on the relaxed strained structures to ensure proper centering of the atoms in the z-direction.

VASPKIT 302 is first run to generate the correct reciprocal-space path corresponding to the irreducible Brillouin zone, generating a KPATH.in file. Following this step, VASPKIT 251 is run to generate KPOINTS for hybrid band structure calculations. The Gamma-scheme is selected, with a k-mesh resolution of 0.03 for both the SCF calculations and along the k-path. This corresponds to an actual reciprocal-space resolution of $2\pi \times 0.03\text{Å}^{-1}$. This step is meant for hybrid calculations, where the band structure is obtained by using zero-weighted k-points for the band-path while simultaneously performing SCF electronic optimization over the regular k-mesh. This method is sometimes flawed, since the zero-weighted band-path does not contribute to the SCF energy convergence criterion. In practice, the band-path will have converged band structures as long as there is a sufficient number of electronic optimization steps. This procedure is not strictly necessary for non-hybrid DFT calculations, such as using the PBE functional, but to maintain simplicity this scheme is adopted for both HSE06 and PBE calculations such that the same KPATH and KPOINTS files may be used across the functionals. TMD monolayers have no net magnetic moment, so spin may safely be

ignored, i.e., ISPIN= 1, for computations ignoring spin-orbit coupling. Band structures with ISPIN= 2 are verified to have both spin-components directly overlapping. Note, however, that SOC *does* impact the band structures, an effect which will be studied with both PBE and hybrid functionals.

3.1.4 Complete Computational Workflow

In summary, the entire computational workflow is as follows:

1. Retrieve 2H (bi-layer) structure from Materials Project and convert to 1H (monolayer)
2. Relax the unstrained structure using PBE functional (ISIF=4, lattice vectors and ionic positions)
3. Apply biaxial strain by stretching in-plane lattice vectors
4. Relax strained structure (ISIF=2, ionic positions)
5. Ensure standardized primitive-cell (VASPKIT 923)
6. Generate reciprocal-space band path (VASPKIT 302, 251)
7. Perform band structure calculation with PBE or HSE06 exchange-correlation functionals
   (a) Optionally, enable spin-orbit-coupling (ISPIN=2, LSORBIT=TRUE) and use vasp_ncl instead of vasp_std
8. Post-process VASP outputs using VASPKIT and Python+pymatgen+sumo to visualize results

Example INCAR files for various steps of the computational pipeline are given in Appendix B.3. VASP outputs are processed using Python and VASPKIT to extract band structure data. Band structures are plotted and analyzed by reading in vasprun.xml and KPOINTS files using pymatgen, parsing high-symmetry reciprocal points through VASPKIT's KLABELS file, and using sumo's helper functions for generating and customizing the plots. sumo is a useful Python toolkit, based on matplotlib and pymatgen, for plotting band VASP simulation data [59].

3.2 Results and Discussion

DFT simulations using VASP are performed to generate electronic band structures for MoS_2, $MoSe_2$, $MoTe_2$, WS_2, and WSe_2 from $-10\% \rightarrow 10\%$ in 1% increments. The full range of data is collected for the PBE functional (PBE) and the PBE functional with spin-orbit coupling included (PBE+SOC). These calculations offer quick, approximate insights into the electronic structures. The HSE06 functional with spin-orbit coupling (HSE06+SOC) is used to simulate the full range of strains for MoS_2, in addition to the unstrained structures for the other four TMD materials. This method offers a much more computationally expensive calculation, with significantly better agreement with experimental results.

The primary bandgap character (direct vs. indirect) is determined by comparing the minimum direct and indirect gaps at each strain level. To account for numerical uncertainty, a tolerance of 0.1eV is introduced: if the direct bandgap lies within 0.1eV of the minimum indirect bandgap, the primary bandgap is classified as direct. This tolerance mitigates small discrepancies arising from finite k-point sampling, band interpolation, and convergence limitations in the DFT calculations, which may produce nearly degenerate direct and indirect gaps. Without such a threshold, these numerical artifacts may lead to unstable or misleading switching between direct and indirect classifications. For example, due to the finite k-point sampling, an indirect bandgap may appear slightly smaller than a direct bandgap when the true band extrema are near a high-symmetry point but are slightly off that point. In such cases, a nearby k-point can yield a marginally lower energy (on the order of tens of meV), resulting in an apparent indirect gap despite the band structure being effectively direct. This classification scheme is utilized for visualizing primary bandgaps in band structure plots, as well as in extracting primary bandgaps from DFT calculations. A more in-depth comparison of the minimum direct and indirect gaps according to strain is given in Sec. 3.2.4.

3.2.1 Optimized Unstrained Structures

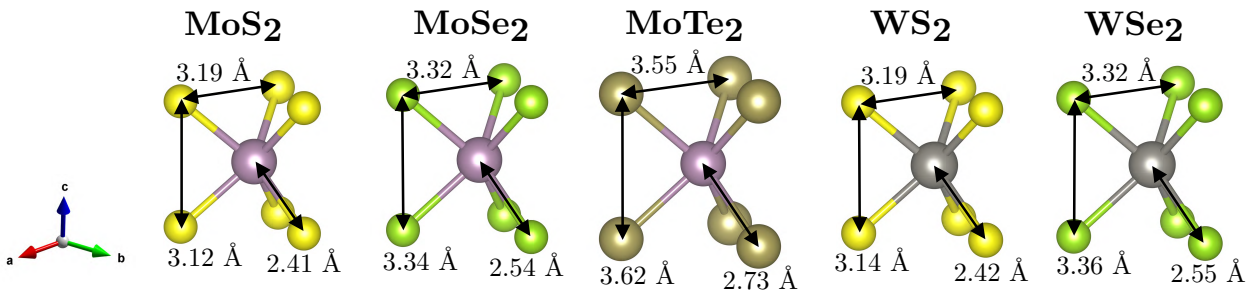

Figure 3.3: Relaxed unit-cells for MoS_2, $MoSe_2$, $MoTe_2$, WS_2, and WSe_2 with annotated distance measurements, to scale. All structures are relaxed using the PBE functional.

The starting point for all band structure calculations is the set of unstrained, relaxed structures. The relaxed structures using the PBE exchange-correlation functional and the converged VASP parameters are displayed graphically in Fig. 3.3 and in tabular form in Table 3.1, where d_{X-X} denotes the monolayer thickness and d_{M-X} denotes the bond-length between the metal and chalcogen atoms. These results demonstrate that the DFT simulations consistently overestimate the lattice constants by an average of 1.04%, thereby underbinding the atoms. While the other experimental distances are not reported here, the results are also consistently underbound by a small margin.

Material	Exp. Lattice Const. (Å) [1]	Lattice Const. (Å)	d_{M-X} (Å)	d_{X-X} (Å)
MoS_2	**3.16**	3.187	2.413	3.122
$MoSe_2$	**3.29**	3.320	2.543	3.342
$MoTe_2$	**3.52**	3.554	2.736	3.618
WS_2	**3.15**	3.186	2.419	3.143
WSe_2	**3.28**	3.322	2.550	3.362

Table 3.1: Comparison of experimental and calculated structural parameters for monolayer TMDs using the PBE functional.

Changing the exchange-correlation functional or adding SOC to the structural relaxation does not greatly change the simulated lattice constants. For example, for MoS_2 with PBE+SOC, $d_{Mo-S} = 2.41283$ Å compared to $d_{Mo-S} = 2.41261$ Å without SOC. These results differ by only $\delta = 0.00022$ Å, so SOC is not included for any structural relaxations.

	MoS_2	$MoSe_2$	$MoTe_2$	WS_2	WSe_2
PBE	1.671	1.452	1.080	1.820	1.547
PBE + SOC	1.570	1.316	0.917	1.553	1.248
HSE06 + SOC	2.147	1.879	1.457	2.102	1.768
Exp. [1]	**2.50**	**2.20**	**1.60**	**2.70**	**2.10**

Table 3.2: Calculated and experimental primary electronic bandgaps (eV) for monolayer TMDs with various DFT functionals and settings.

The primary electronic bandgaps for unstrained TMDs are demonstrated in Table 3.2. While the DFT results are quite consistent with previous studies [11, 13], the electronic bandgaps are highly sensitive to the exchange-correlation functional and spin-orbit coupling. The PBE bandgaps are anywhere between $0.5-0.8$eV below the experimental values reported in previous literature [1]. The PBE+SOC bandgaps are even lower than the PBE results by $0.1 - 0.3$eV, very poorly matching the experimental values. This occurs as a consequence of the spin-orbit splitting of the valence band, narrowing the bandgaps. The HSE06+SOC bandgaps are significantly closer to experimental results. However, these calculations still

under-estimate the bandgaps by an average of 15.1% across these materials.

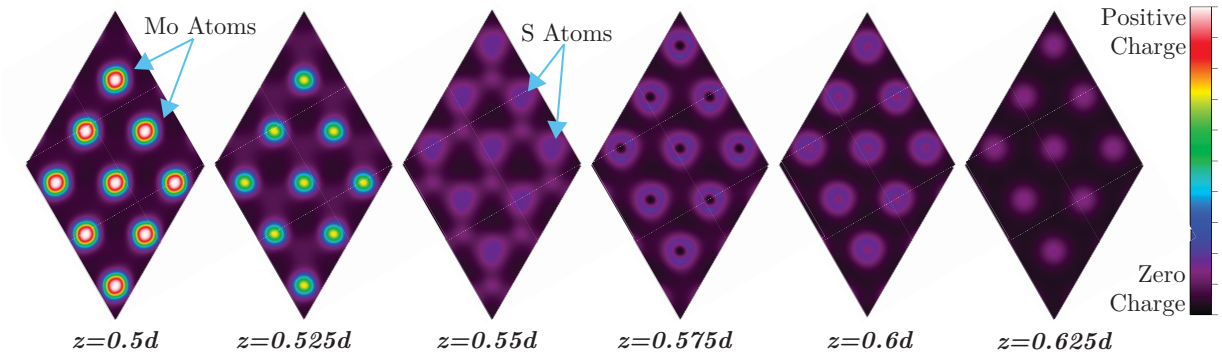

Figure 3.4: Charge-density cross-sections of unstrained MoS_2 along the (001) plane (viewed perpendicularly from the monolayer surface). The viewing position z is taken as various fractions of the unit-cell height d, where $z = 0.5d$ is precisely the cross-section at the vertical center. Sites of the molybdenum and sulfur atoms are explicitly labeled.

Fig. 3.4 displays the charge-density distribution of MoS_2, viewed from various vertical cross-sections (the (001) plane). The cross-section is sliced at various fractions of the unit-cell height, d: $z = 0.5d$ directly corresponds to the section at the vertical center of the monolayer. The cross-section at $z = 0.5d$ depicts that charge is most significantly localized at the metallic atom, molybdenum. At $z = 0.525d$, the charge-density increases at the sites between the metallic atoms, revealing the trigonal prismatic coordination: chalcogen atoms are located precisely at alternating geometric centers of the molybdenum sites. The covalent bonds are also present from this view, represented as charge-density situated between the atomic sites. At $z = 0.55d$, charge is mostly localized at the chalcogen atoms, and the bonds are still observable. At $z = 0.575d$, there is an absence of charge-density at the center of the chalcogens. As the vertical-position of the cross-sections continues to increase, the charge-density diffuses.

3.2.2 PBE Band Structures

DFT simulations using the PBE exchange-correlation functional offer a quick approximation of true material behavior: calculations for each strain level are completed within five to ten minutes each using 64 CPU-cores.

Electronic band structures and corresponding projected density-of-states (PDOS) are shown in Fig. 3.5 for MoS_2, using the PBE exchange-correlation functional. The PDOS plots depict the orbital contributions of the constituent orbitals from Mo and S to the overall DOS. All of the PDOS plots correctly depict no state density within the bandgap. The shading of the bands themselves is also a projection, displaying the relative contributions from Mo and

S by interpolating between blue and red. This demonstrates that the valence and conduction bands are primarily formed by Mo states, while some of the lower-energy bands are primarily formed from S states.

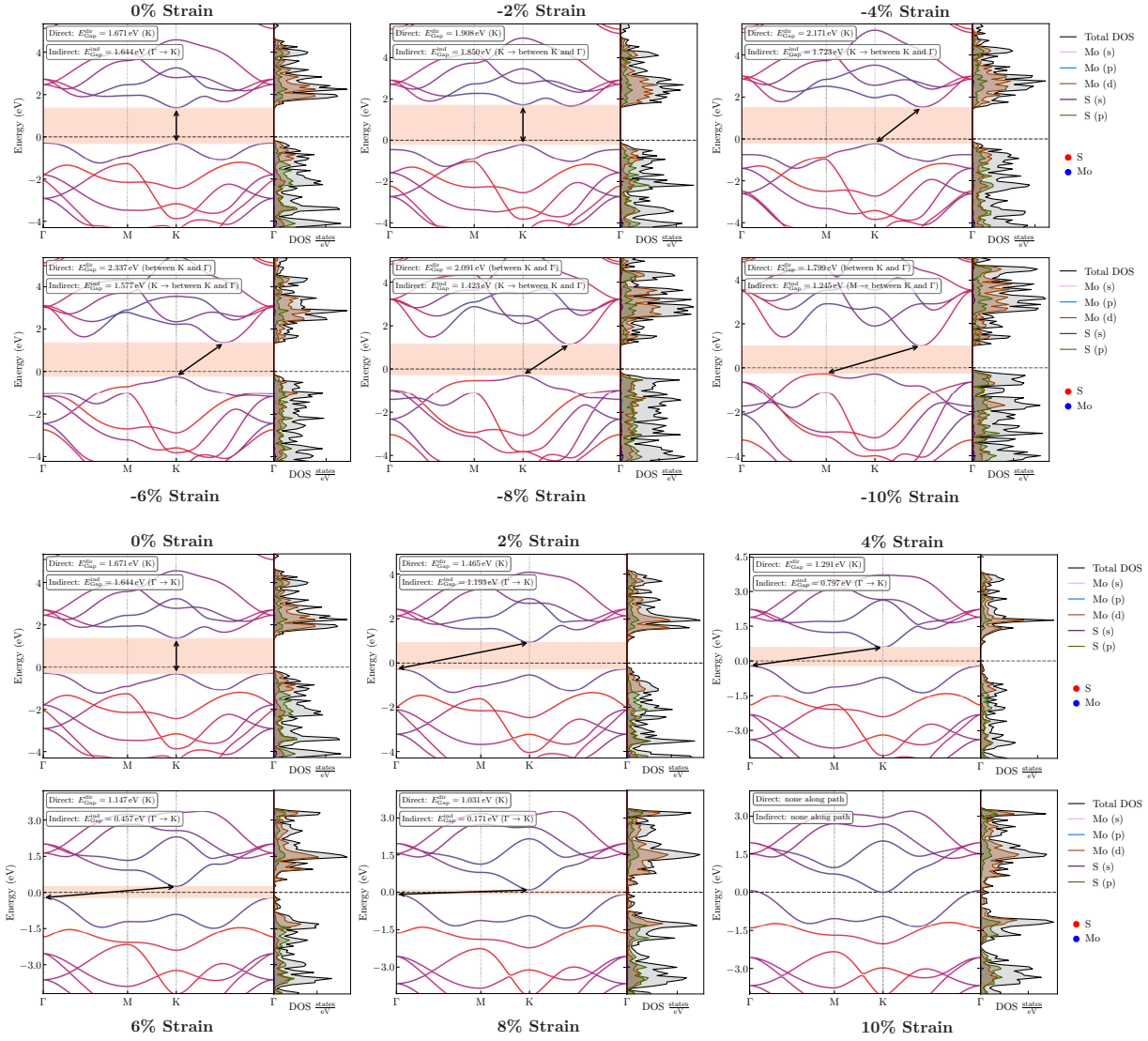

Figure 3.5: Electronic band structures and corresponding projected density-of-states of MoS_2 under biaxial (a) compressive and (b) tensile strains, computed using the **PBE** exchange-correlation functional. The band shading corresponds to the orbital contributions from the constituent elements. The Fermi level has been set to 0eV.

Unstrained, MoS_2 exhibits a direct bandgap at the K point. Under 2% compressive strain, this direct bandgap slightly widens to 1.91eV. Further increasing the compressive strain decreases the bandgap magnitude and switches the band character to an indirect bandgap. A majority of the band-modulation occurs in the conduction band, with the valence band maximum (VBM) remaining at the K point until -8% strain. For the indirect

bandgaps, the conduction band minimum (CBM) occurs about halfway between the K and Γ points, shifting closer to the valence bands with increasing strain and narrowing the bandgap. At −10% strain, the VBM swaps to the M point. Between 0% and −10% strain, there is only a total bandgap narrowing of 0.426eV, demonstrating that compressive strain does not *significantly* alter the electronic band structures.

Biaxial tensile strain, conversely, provides significant band modulation, on the order of 1.67eV from 0% to 10% strain. At 2% tensile strain, the bandgap immediately becomes indirect, with the CBM remaining at the K point and the VBM transitioning to the Γ point. This differs from compressive strain where the VBM remained at the K point. The indirect bandgap quickly narrows, and by 10% biaxial strain, MoS_2 exhibits metallic behavior with no bandgap. However, given PBE's systematic underestimation of gaps, this may not represent a true semiconductor–metal transition, with the true transition likely occurring at even higher strain (which may not be physically realizable before fracture).

Fig. 3.6 depicts PBE+SOC band structures of MoS_2, now with spin-orbit coupling included. Overall, the general trends discussed above with the PBE band structures and the bandgap nature/position are identical, including the general magnitude of band tunability. Despite the inclusion of SOC, a majority of spin-up and spin-down bands appear nearly degenerate. Unlike using ISPIN=2 alone, SOC calculations in VASP do not separately index the spin-up and spin-down bands, so these cannot precisely be isolated or separated. Notably, the valence band undergoes splitting at the K point for all strain levels. At this reciprocal lattice location, the conduction band undergoes negligible splitting. These splitting trends are consistent with previous strained and unstrained studies [12, 60, 61]. Compared to the non-SOC band structures, there is also a slight dimple at the K point, potentially occurring as a result of the finite sampling of reciprocal lattice points along the band path. Otherwise, the bands generally appear smooth.

The full electronic band structures for the other TMD materials with the PBE functional are provided in Appendix B.2.1.

3.2.3 Hybrid Band Structures

Band structure calculations are also performed with the HSE06 exchange-correlation functional with SOC included. This is a DFT+HF method, using a screened hybrid functional that mixes a fraction of exact Hartree-Fock (HF) exchange with the PBE exchange [62]. Consequently, these computations are significantly more computationally expensive compared to using the PBE functional, but they also produce significantly more accurate band structures.

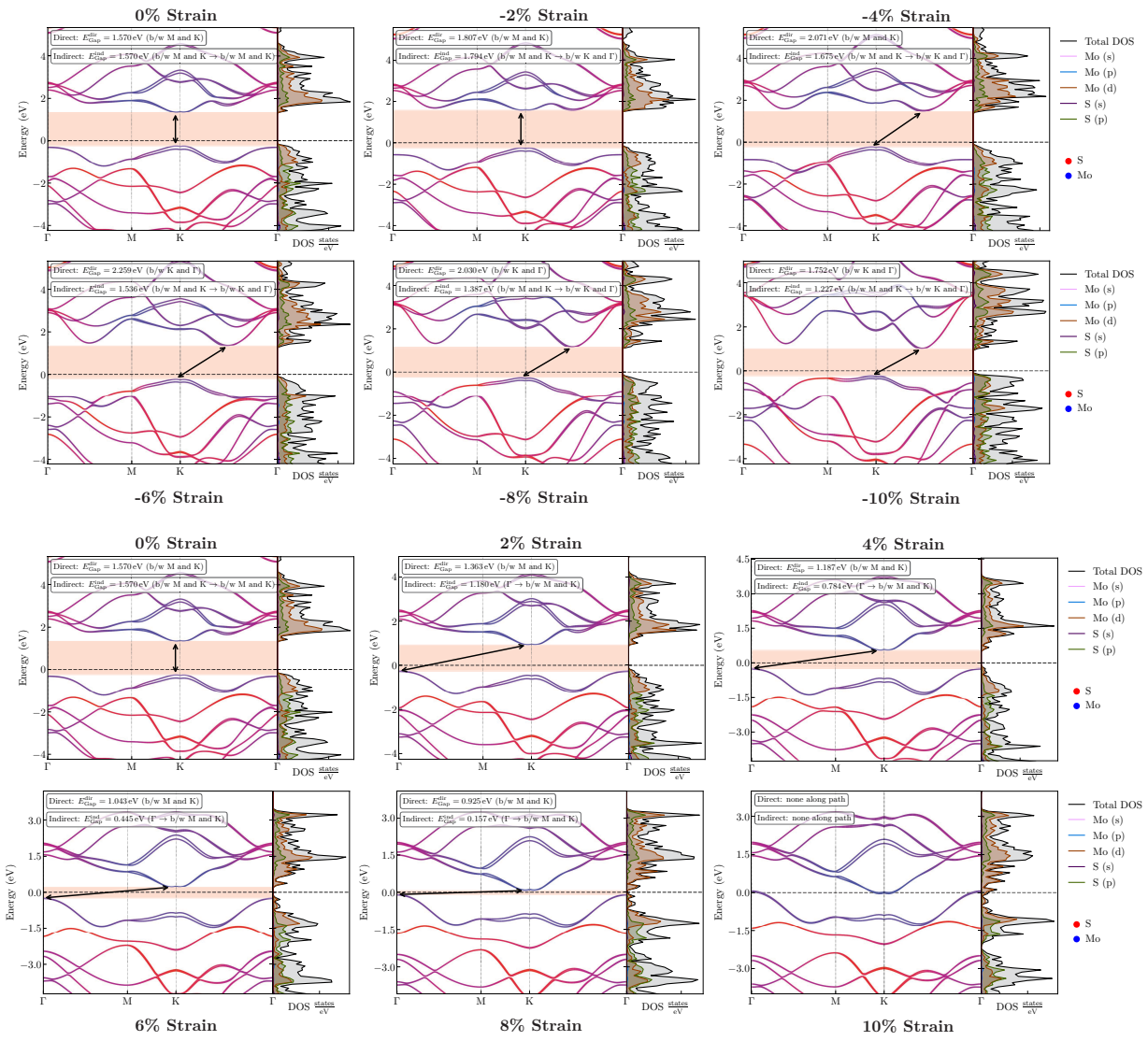

Figure 3.6: Electronic band structures and corresponding projected density-of-states of MoS_2 under biaxial (a) compressive and (b) tensile strains, computed using the PBE exchange-correlation functional **with spin-orbit coupling**. The band shading corresponds to the orbital contributions from the constituent elements. The Fermi level has been set to 0eV.

The exchange-correlation energy corresponding to the hybrid functional is as follows:

$$E_{xc}^{\mathrm{HSE}} = \alpha E_x^{\mathrm{HF,sr},\mu} + (1-\alpha) E_x^{\mathrm{PBE,sr},\mu} + E_x^{\mathrm{PBE,lr},\mu} + E_c^{\mathrm{PBE}} \tag{3.2}$$

where sr and lr correspond to short-range and long-range respectively, α is an empirical weighting parameter, and μ is the range-screening length in units of Å^{-1}. The HSE06 functional uses parameters $\alpha = 0.25$ and $\mu = 0.2$. This functional is considered screened, since the potential is screened with a complementary error function (erfc). The HF exchange

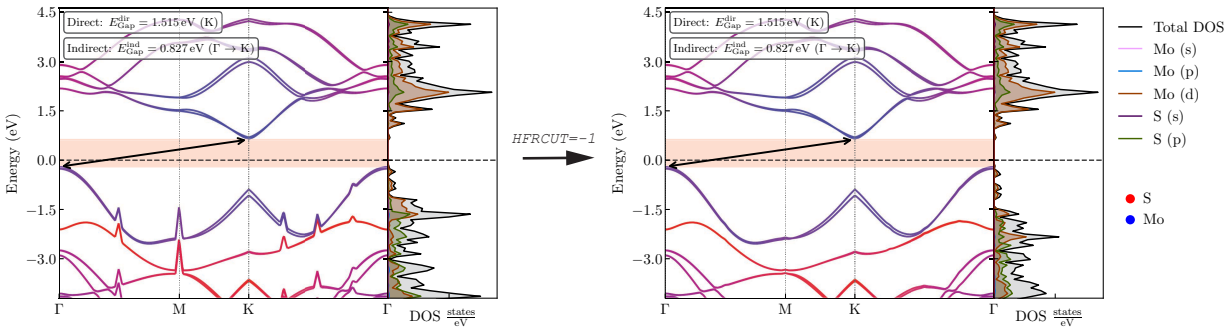

Figure 3.7: Before and after plots of the MoS_2 band structure under 6% biaxial strain using the HSE06+SOC method, demonstrating the noisy valence band behavior fixed by resuming calculations with HFRCUT= −1.

is only used at short-range, while the PBE exchange is used at longer-ranges. This is done to speed-up computations while maintaining accuracy, since computing the full HF exchange for the long range involves computationally expensive exchange integrals. Further details of the HSE06 exchange-correlation functional can be found on VASP's wiki page.

The HSE06+SOC band structure calculations employ the same converged VASP parameters as reported in Sec. 3.1.1. Using 128 CPU-cores, each calculation takes anywhere between $4 - 8$ hours on average, depending on exact hardware and electronic convergence behavior. While initial band structures appeared robust, after running HSE06+SOC calculations for the full range of materials and strain levels, an issue emerged, as shown in Fig. 3.7. The valence bands exhibit noise and spikes at certain reciprocal-lattice points, causing a slight positive offset for the valence band energy values at these points. The depicted plot has five such spikes which do not interfere with the bandgap, although other simulations had spikes interfering with the true bandgap, interfering with the extracted bandgap magnitude, character, and location. Due to the unreliability of this data, these runs cannot be analyzed in their current form.

This issue could be caused partially by the zero-weighted nature of the reciprocal-lattice paths for the band structures, resulting in potentially unconverged energy values. However, this issue was never present in any of the PBE runs, making this explanation highly implausible. Resuming runs attempting to improve electronic convergence did not resolve the issue, nor did beginning new runs with more stringent electronic convergence criteria. After a lengthy troubleshooting process, modifying the HFRCUT parameter from the default value of 0 to −1 almost perfectly smoothed out the valence bands and eliminated all spikes. From the VASP wiki, "this parameter specifies how the Coulomb kernel is approximated at $G = 0$ when the Fock energy and the exchange potential are evaluated." Switching to HFRCUT= −1 employs an alternative algorithm, "setting an automatic radius to replace the

$1/r$ Coulomb kernel with a truncated Coulomb kernel that is strictly zero beyond a certain cutoff radius" [63]. This required approximately $1-2$ hours of additional computation, resuming VASP simulations from the existing WAVECAR files.

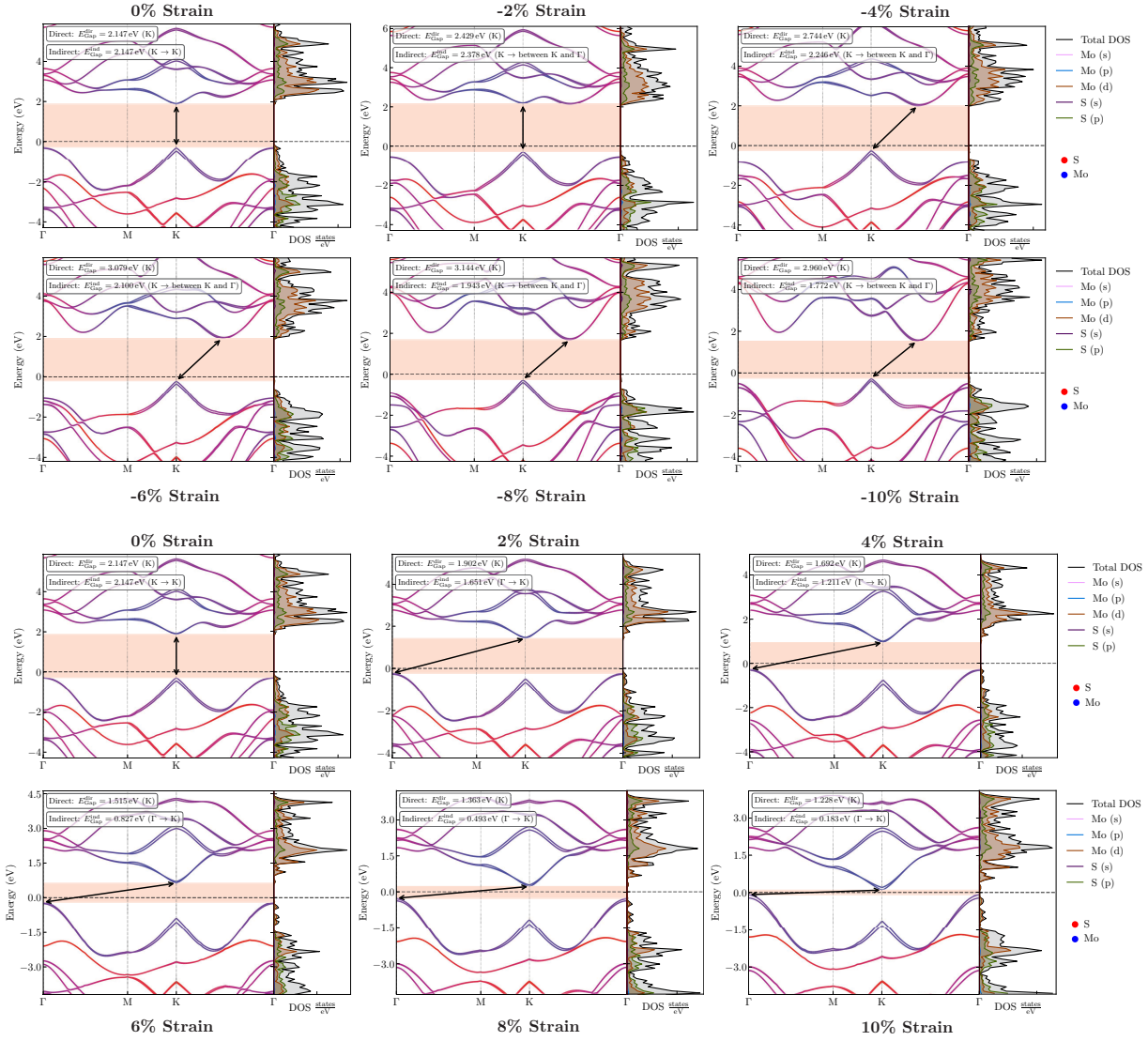

Figure 3.8: Electronic band structures and corresponding projected density-of-states of MoS_2 under biaxial (a) compressive and (b) tensile strains, computed using the **HSE06 exchange-correlation functional with spin-orbit coupling**. The band shading corresponds to the orbital contributions from the constituent elements. The Fermi level has been set to 0eV.

Fig. 3.8 displays the MoS_2 band structures using the HSE06+SOC method. While the trends are generally the same as in the PBE and PBE+SOC methods, the bandgaps are now much larger. For example, under tensile strain, the band structure does not quite become metallic even at 10% strain. However, the bandgap is narrowed on the order of 2eV, about 0.3eV higher than the PBE band tunability. The indirect bandgap with the HSE06

method at -10% strain has larger magnitude than the direct bandgap using either of the PBE approaches at 0% strain, despite the bandgap narrowing with compressive strain. This conveys the substantial differences in bandgap magnitudes between the PBE and HSE06 methods. Using the HSE06+SOC method, the concavity of the bands is also significantly different from previous PBE calculations: at the K point, the HSE06+SOC bands display much higher concavity. Spin-orbit coupling yields similar band splitting as the PBE+SOC results, yielding predominantly degenerate bands.

3.2.4 Trends in Electronic Band Gaps

The electronic band structures may be processed in various ways to better understand trends of TMD behavior under strain. For this section, PBE band structure data is used, as it exhibits qualitatively the same behavior as the more accurate yet computationally more expensive HSE06+SOC data. A more detailed discussion of these trends between functionals is presented near the end of this section.

One such way to analyze the band structures is to visualize the band-evolution under strain, overlaying the valence and conduction bands from different strain levels on the same plot. The valence-band K point energy may be fixed, so that the K $\rightarrow$ K transition can directly be visualized. This type of plot is particularly meaningful, since this is in general the smallest direct bandgap for monolayer TMDs. It is precisely this transition that dictates TMDs optical properties. Fig. 3.9 plots these band structure evolutions across the set of TMD materials under study. While each material exhibits distinct characteristics and differing ranges of strain tunability, all of these materials display an increasing K $\rightarrow$ K bandgap with compressive strain and a decreasing K $\rightarrow$ K bandgap with tensile strain.

Across these plots, TMDs with the same chalcogen element show greatest similarity – for example, MoS_2 and WS_2 show the highest degree of strain tunability, with the largest spread in conduction-band K point energies under strain. $MoSe_2$ and WSe_2 also show similar results to one another, with slightly lower strain tunability. $MoTe_2$ shows the smallest range of strain-modulation, having the smallest spread of conduction bands in its plot.

This trend can be rationalized by simply considering and analyzing atomic radii. Molybdenum ($[Kr]4d^5 5s^1$) and tungsten ($[Xe]4f^{14}5d^4 6s^2$) have similar metallic radii, 1.402 and 1.410 Å, respectively [64]. This similarity and the almost identical radii arise from lanthanide contraction: as the 4f orbitals are filled across the lanthanide series, their poor shielding increases the effective nuclear charge felt by the 5d valence electrons, pulling these valence electrons closer to the nuclei and reducing the expected size expansion of the 5d elements. As a result, tungsten is only slightly larger than molybdenum, and TMDs containing Mo or

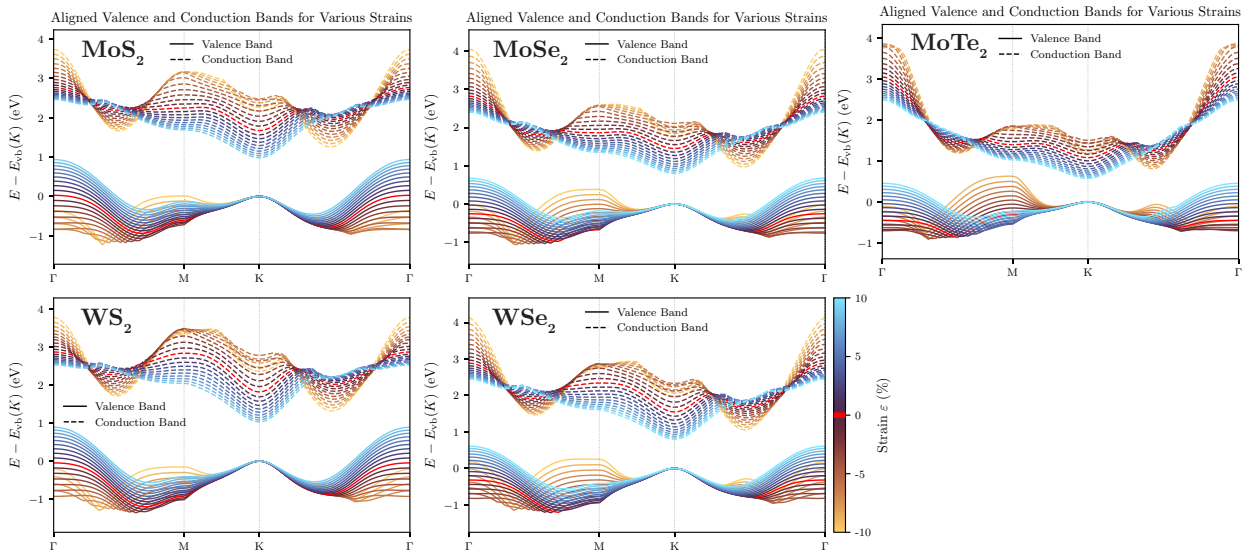

Figure 3.9: Valence and conduction band evolution across TMD materials according to PBE simulations, with $E_{\text{vb}}(K)$ at each strain level set as the reference energy. The red bands denote the unstrained case.

W with the same chalcogen element tend to have very similar properties. In contrast, the chalcogen elements show much greater variation in size and behavior. Sulfur, selenium and tellurium have Slater atomic radii of 1.00, 1.15, and 1.40 Å, respectively [65]. This progressive increase in size significantly alters bonding character and orbital overlap, leading to much more pronounced differences in the structural and electronic properties when changing between sulfur, selenium, or tellurium.

Trends of bandgap-modulation may also more generally be plotted as bandgap vs. strain, allowing for quick comparison between strain levels and materials, as shown in Fig. 3.10. This plot depicts not only the primary bandgaps, but also the minimum direct, indirect, and K-point gaps across strain levels. The K-point gap is computed simply as the difference between conduction band and valence band energies at the K high-symmetry point. While the primary bandgap character might be considered as "indirect" at a given point, the smallest direct transition and K-point gap are still physically meaningful quantities. Furthermore, the lowest direct gap dictates a material's optical response, since phonons are typically not involved for radiative recombination. Overall, this figure demonstrates how the various TMD materials all exhibit primary direct bandgaps roughly in the range of $-2\% \rightarrow 2\%$ strain, with the maximum primary bandgap occurring under a slight compressive strain. Under higher compressive strains (or tensile strains) the overall primary bandgap magnitude decreases across all scenarios. Qualitatively, all the plots display similar shapes for each quantity. Across materials, the minimum direct bandgap displays a similar, slightly curved,

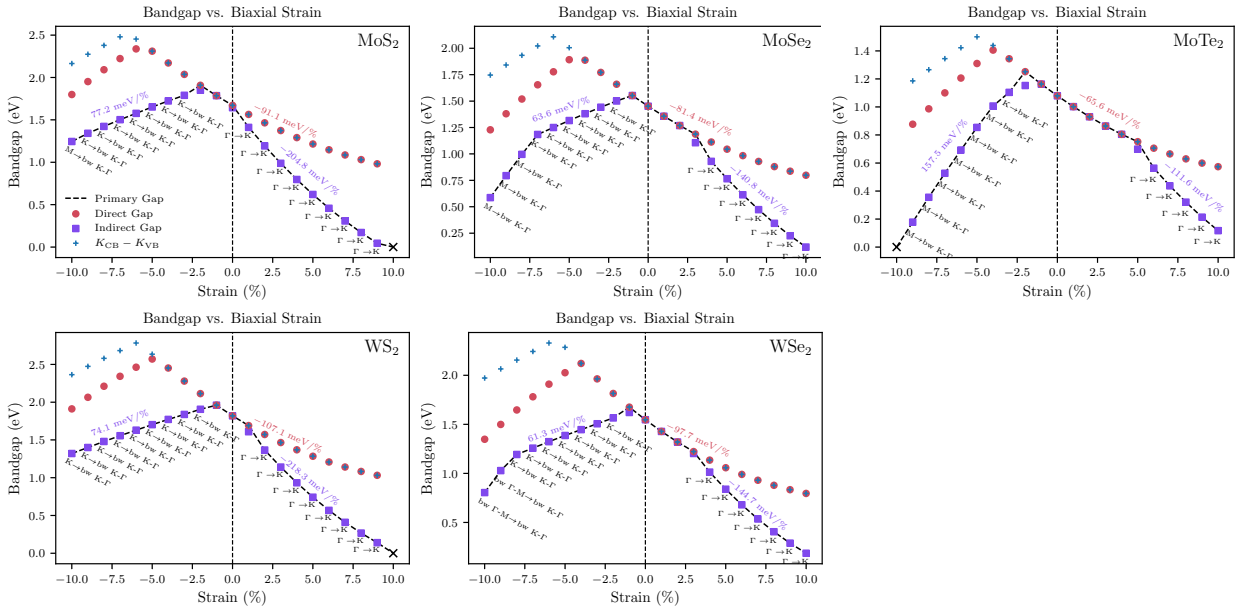

Figure 3.10: Plots of bandgap vs. biaxial strain for various TMD materials, computed using PBE data. The dashed black line denotes the primary bandgap (minimum gap at each strain), while colored markers indicate the direct gap (circles), indirect gap (squares), and the $K_{\mathrm{CB}} - K_{\mathrm{VB}}$ gap (crosses). Metallic states, where the primary gap closes, are marked by black $\times$ symbols at zero energy. Band-edge locations are annotated for gaps occurring between high-symmetry points. Linear fits are performed over selected strain ranges to quantify local trends in the direct and indirect gaps, with gauge factors (slopes) reported on the corresponding segments.

decreasing trend from around -5% to 10% strain. The two sulfur-based TMDs transition to metallic behavior (with no bandgap) at 10% tensile strain, while $MoTe_2$ transitions to metallic behavior at -10% compressive strain.

According to Fig. 3.10, all primary direct bandgaps occur at the K high-symmetry point. The primary indirect bandgaps under tensile strain occur between the $\Gamma \to$ K points in the valence and conduction bands, respectively. Indirect bandgaps under compressive strains do not occur at specifically named high-symmetry points in the conduction bands, although their valence band maxima typically fall at the K, or for higher compressive strains, the M high-symmetry points. The slope of these bandgap-strain plots is known as the gauge-factor (meV/% strain), indicating the rate of bandgap tunability with strain. These plots are generally monotonic and linear in the tensile and compressive regions: however, the selenides have a "kink" in their plots, whereby the gauge factor and bandgap tunability increase for high compressive strains. This overall linearity allows for precise tunability of the electronic bandgaps in either the tensile or compressive regimes, regardless of the exact strain magnitude. Experimentally, these strain modulation trends allow for the extraction

of the strain magnitude based on bandgap measurements and expected gauge factors.

Across materials there is also a consistent decoupling of the minimum direct gap from the K-point above -5% or -6% strains. As shown in Fig. 3.5, the minimum direct gap transitions toward the Γ-point, decreasing in magnitude with a positive gauge factor. In contrast, the K-point gap continues to slightly increase with higher compressive strains, before decreasing with a similar gauge factor. This effectively results in a minimum direct gap in the range of tens of meV smaller than the K-point gap for these high compressive strains.

In the tensile regime, all direct-gap gauge factors are computed through linearly fitting the datapoints from 0 to 5% strain. With the same chalcogen element, the tungsten-based TMDs show higher direct gap gauge factors by about -16meV/% compared to the molybdenum-based counterparts. Similarly, the direct gap gauge factors decrease moving right across the figure: sulfur-based TMDs have about a -10meV larger direct-gap gauge factor compared to their selenium counterparts. Thus, WS_2 has the largest direct-gap tensile gauge factor at -107.1meV/%, while $MoTe_2$ has the smallest at -65.6meV/%. Looking at the minimum indirect-gaps, a qualitatively similar trend is seen with their tensile gauge factors. For example, WS_2 has the largest indirect-gap tensile gauge-factor at -218.3meV/%, while $MoTe_2$ has the smallest at -111.6meV/%. In the compressive regime, indirect bandgap gauge factors appear to be independent of transition metal and sensitive to chalcogen element. MoS_2 has a moderate indirect bandgap compressive gauge factor of 77.2meV/%, while $MoTe_2$ has a significantly higher gauge factor of 157.5meV/%. This demonstrates that the telluride-based TMDs exhibit qualitatively different behavior than the sulfur and selenium TMDs, resulting in their metallic transition in the compressive regime rather than the tensile regime.

One notable feature of these plots is that the primary bandgap exhibits a maximum under a slight compressive strain. The minimum direct gaps exhibit maxima at even higher compressive strains compared to the primary gap. In both cases, the highly compressive regime tends to have a positive gauge factor, and in the tensile regime, a negative gauge factor. This is notable since neither trend is monotonic over the entire range, nor are the results symmetric about the zero-strain level. While experimental studies of TMDs under biaxial compressive strain are limited, a past optical study reports an increased exciton energy under 1.2% compressive strain. This would directly correspond to an increased electronic bandgap, hence verifying the trend [8]. Another possible explanation for this behavior is as follows: in general, the GGA method and PBE exchange-correlation functional tend to under-bind atoms, causing atomic bond-lengths that are slightly too long, as observed in the structural relaxation for these materials presented in Sec. 3.2.1. Recall that lattice-constants appeared to be approximately 1% too long. Thus, it is possible that a slight $1-2\%$ compressive

strain *also* yields an improved lattice structure, more closely resembling the experimental structures, thereby retrieving improved bandgaps more closely matching the experimental results. For example, whereas the HSE06+SOC bandgap for MoS_2 is 2.147eV, its maximal bandgap under -2% strain is 2.43eV, significantly closer to the experimental value of 2.50eV. Similar behavior is observed in past DFT results [3, 13, 66], but this suggests that more careful structural relaxation of the unstrained structures may yield further-improved band structure data using the hybrid functional. Still, the bandgap underestimation is most likely a consequence of the GGA methodology, and the PBE method alone is not responsible for the observed trend. Due to the verification with experimental results, it appears to be merely coincidental.

Among the materials studied, the sulfides tend to have the greatest tensile-strain gauge factor, followed by the selenides and tellurides. Tungsten-based TMDs have slightly higher gauge-factors than corresponding molybdenum-based TMDs, although the difference is quite small. On the other hand, $MoTe_2$ is the only TMD exhibiting a metallic transition under compressive strain: it has the greatest compressive-strain gauge factor. In fact, it has a greater degree of strain tunability under compressive strain compared to under tensile strain. Among the materials studied, the sulfides have the highest primary gap gauge factors for small strain levels. In the tensile regime, WS_2 stands out as a clear winner in terms of its strain tunability: this will be further explored experimentally in Chapter 5.

Comparison of Functionals

The plots of valence and conduction band evolution, in addition to bandgap vs. strain, are also plotted for MoS_2 with both PBE and HSE06+SOC data. Fig. 3.11 compares the band evolution results between the PBE and HSE06+SOC band structures.

These plots demonstrate that the qualitative behavior between the two methods is the same, validating the choice of PBE data for qualitative analysis. Both calculations corroborate that compressive biaxial strains will increase the magnitude of the K direct bandgap, while tensile strains will decrease the magnitude of the K direct bandgap, with similar overall range of tunability. However, it is immediately apparent that the two methods yield vastly different valence band curvature at the K point. Generally, $\frac{1}{m^*} \sim \frac{d^2E}{dk^2}$, indicating that holes have a smaller effective mass according to the HSE06+SOC calculations compared to the PBE approach, as a consequence of the higher concavity (2nd derivative). This would generally also suggest an increased hole mobility, μ_h, with the HSE06+SOC calculations.

Plots of bandgap vs. strain for PBE and HSE06+SOC data are also compared for MoS_2 in Fig. 3.12. This displays the large bandgap differences between these two methodologies. For example, since the HSE06+SOC unstrained bandgap is 0.476eV larger than the PBE result,

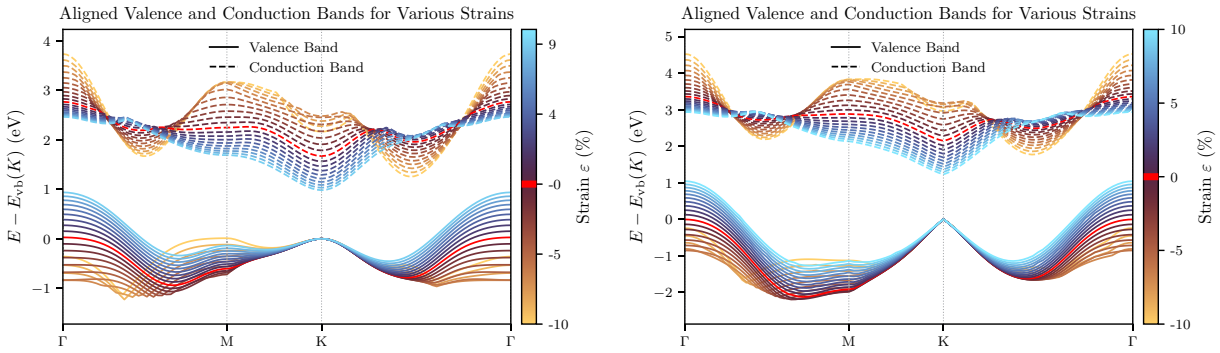

(a) (b)

Figure 3.11: Valence and conduction band evolution of MoS_2 for (a) PBE data, and (b) HSE06+SOC data, with $E_{vb}(K)$ at each strain level set as the reference energy. The red bands denote the unstrained case.

it does not quite undergo a metallic transition at 10% tensile strain. In the tensile regime, the magnitude of HSE06+SOC gauge factors are approximately 20meV/% greater compared to the PBE data for both the direct and indirect gaps. In comparison, the compressive gauge factors are almost identical between the methods. Another qualitative difference is associated with the direct gaps at high compressive strains: for the PBE data, the direct-bandgap begins to diverge from the K-point gap, moving toward the Γ-point. In contrast, the direct-bandgap with the HSE06+SOC data remains at the K-point for the entire range of strains. This indicates a slight difference in the overall behavior of the band structures, although they qualitatively remain very similar between the two methods. This trend is consistent with the behavior depicted in Fig. 3.11– since the PBE method predicts much lower valence band curvature, its minimum direct gap is able to move toward the Γ-point. In contrast, the HSE06+SOC method predicts a valence band with a much higher curvature and more pronounced maxima at the K-point, so its minimum direct gap is consequently fixed here regardless of strain magnitude.

Further quantitative data on MoS_2 bandgaps vs. strain for PBE, PBE+SOC, and HSE06+SOC methods is provided in Appendix B.2.2.

3.2.5 Band-Edge Evolution Under Strain

For future device design, it is important to not only study the various electronic transitions and gaps under strain, but also the specific evolution of the valence and conduction bands. The specific band-edge states studied are: the valence-band maxima (VBM), conduction-band minima (CBM), K-point valence-band energy E_{VB}(K), and the K-point conduction-band energy E_{CB}(K). There are various ways to reference these energies for comparison: for

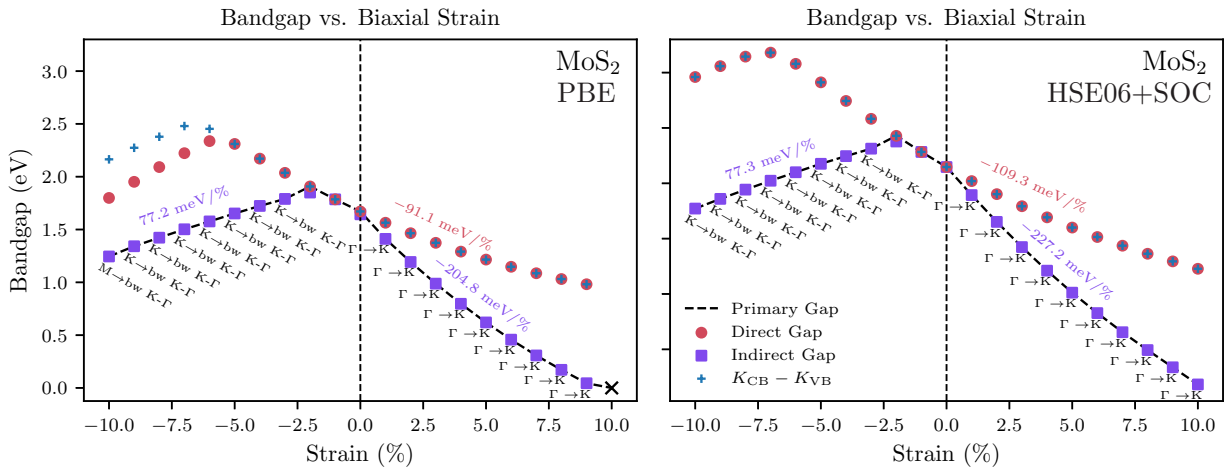

Figure 3.12: Bandgap vs. biaxial strain for MoS_2, comparing PBE and HSE06+SOC results (shared vertical scale). The primary bandgap is depicted as a dashed black line, with markers indicating direct, indirect, and $K_{CB} - K_{VB}$ gaps. Metallic states are marked by black $\times$ symbols, and labeled gauge-factors highlight local strain tunability trends through linear fitting.

example, taking the raw DFT output energies, referencing energies to the Fermi level, or referencing the energies to the vacuum level. Since the Fermi level may change with strain (and is not necessarily the most robust reference with DFT), the vacuum energy is used as a reference. The vacuum energy may simply be considered as the electrostatic background energy sufficiently far away from the TMD monolayer. For each DFT simulation, the vacuum energy is computed in a simple multi-step process. First, the planar-averaged electrostatic potential is computed perpendicular to the surface of the TMD monolayer. Then, the values are retrieved at the top and bottom of the unit cell: these are averaged, and the result is the vacuum energy. This is logical since the top and bottom of the cell are sufficiently far away from the TMD monolayer due to the 15Å introduced vacuum spacing between periodic monolayers.

Fig. 3.13 depicts plots of vacuum-aligned band-edge energies vs. biaxial strain for various TMD materials. These plots provide context to the simplified bandgap analysis of Fig. 3.10, displaying the movement of the VBM and CBM according to strain. At each strain level, the gap between VBM and CBM (blue and purple squares) is precisely the primary bandgap. It is immediately clear that for the sulfide and selenide TMDs, the gap closes much quicker in the tensile regime compared to under compressive strains. The positions of the valence band and conduction band K-point energies are also shown with green and red circles, respectively, allowing for the tracking of this optical transition.

There are several overarching trends consistent across the materials. For example, the

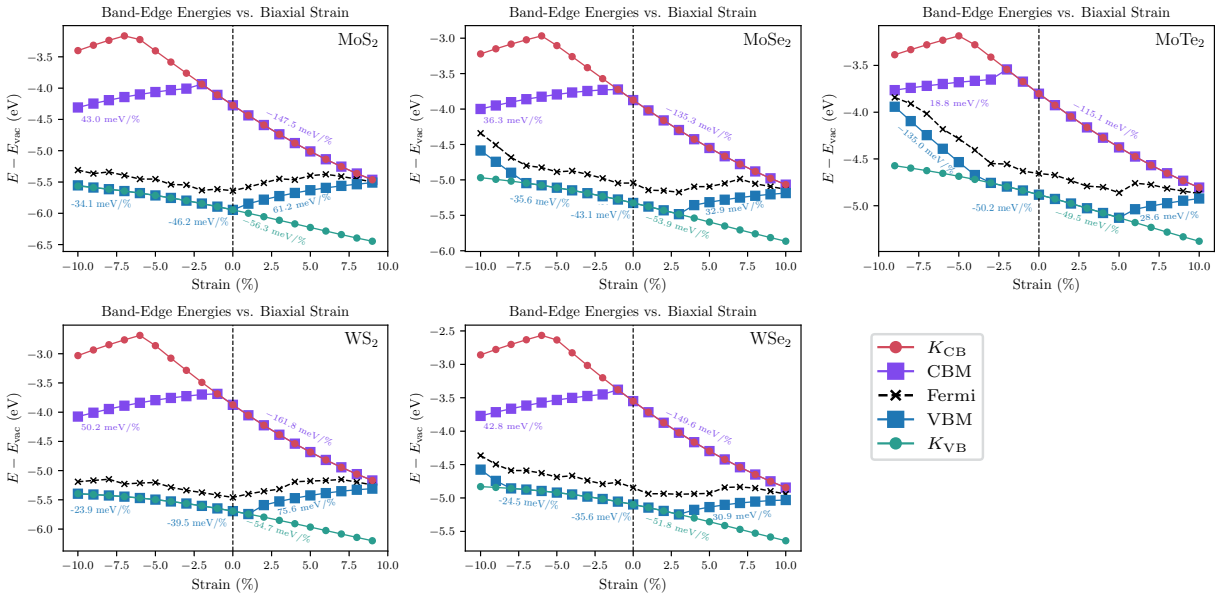

Figure 3.13: Vacuum-aligned band-edge energies vs. biaxial strain for various TMD materials, computed using PBE. Energies are referenced to the vacuum level at each strain. The Fermi level is shown as a dashed black line, while colored markers denote K_{CB} (red circles), CBM (purple squares), VBM (blue squares), and K_{VB} (green circles). Linear fits over selected tensile and compressive strain ranges quantify local trends in the conduction and valence band edges, with slopes reported on the corresponding segments.

conduction bands tend to have the highest strain tunability, therefore dictating the overall bandgap tunability with strain. Across the materials, the CBM and K_{CB} behavior are consistent: the CBM is at the K-point in the tensile regime, and it shifts toward the Γ point in the compressive regime. The CBM tends to decrease in energy for both compressive and tensile strains, with opposite slopes in each strain regime. The K_{CB} energy shows slightly different behavior: its energy decreases monotonically from around $-7\% \rightarrow +10\%$ strains, with an inflection for highly compressive strains where its gauge factor switches from positive to negative.

The trends for the VBM are effectively the inverse of the CBM trends across the materials– specifically the energy tends to increase in the tensile regime and for the compressive regime, forming a stretched out "V" shape. Note that due to the slight curvature of the VBM as strain changes, the gauge factors consequently change: as such, there are gauge factors for the high-compressive strain and low-compressive strain regimes depicted on each plot. This behavior is in line with a quadratic relationship, although the precise fitting of these trends and calculation of the bowing parameter is outside the scope of this work. There tends to be far less VBM tunability compared to the CBM behavior, except for $MoTe_2$ which exhibits significantly exaggerated trends compared to the other TMDs. The tensile

VBM gauge factors for the sulfides are about twice in magnitude compared to their high-compressive strain gauge factors, whereas the selenides have similar magnitude gauge factors in both regimes with opposite signs. The compressive strain VBM gauge factors are about 10meV/% higher in magnitude for the molybdenum-based TMDs compared to the tungsten-based TMDs, and these quantities appear relatively invariant to chalcogen element. The VBM tends to fall on the K-point under compressive and low tensile strains, although for higher tensile strains it shifts to the Γ-point.

The K_{VB} energies depict a unique trend not observed with the other band-edge energies. The behavior is entirely monotonic across the entire range of strains, with relatively consistent gauge factors across all the materials between $25 - 50$meV/%. In contrast, the VBM, CBM, and K_{CB} energies all have some inflection point where the gauge factor flips sign. The sulfide-based TMDs tend to have relatively consistent gauge factors across the strain regions for the various band-edges, while the selenide and telluride-based TMDs exhibit a large jump in gauge-factor magnitude for the VBM under high compressive strains.

In terms of the magnitude of strain tunability in the tensile-regime (for all of the band-edge trends), the sulfides have the highest tunability, followed by the selenides and tellurides. For compressive-strain tunability, TMDs with similar transition-metals show similar tunability in the VBM, with slightly more chalocogen-sensitivity in the CBM, consistent with the tensile trends. In both the tensile and compressive regimes, the tungsten-based TMDs have slightly higher tunability than the corresponding molybdenum-based TMDs. WS_2 has the highest tensile strain CBM tunability at -161.8meV/%, as well as the highest tensile strain VBM tunability at 75.6meV/%. $MoTe_2$ has by far the highest overall VBM tunability under compressive strains at -135.0meV/%, with the caveat that this gauge factor is only achieved at strains greater than -4%.

One important note observed in these plots is the Fermi-energy which always appears to follow the trends of the VBM, albeit offset by around +25meV into the bandgap. Using VASP, the Fermi energy is not uniquely defined within the bandgap and is somewhat arbitrary: as such, the Fermi energy tends to fall toward the valence band. This skewed Fermi energy does not otherwise impact the calculations.

Using this band-edge data, TMD heterostructure devices with potential for unique strain-characteristics are presented in Chapter 6.

3.3 Limitations and Future Work

While this work provides a thorough analysis of TMD monolayers under biaxial strain, further computational work is still needed in the field of strain-engineering. Given the

high research interest in TMDs and other two-dimensional materials like graphene, black phosphorus (BP), and hexagonal boron nitride (h-BN), there is ample utility in tuning an exchange-correlation functional specifically for two-dimensional materials. Computationally, this could be as simple as tuning the empirical weighting parameters of a hybrid functional, or as complicated as weighting various exchange-correlation functionals together to reproduce experimental results across a wide range of compounds. Regardless, this would significantly aid in modeling the optical and electronic properties of current and future two-dimensional materials. Another plausible development could include fine-tuning a large, foundational machine-learning interatomic potential (MLIP) specifically for use with two-dimensional materials. This could help in modeling complex heterostructures with large supercells while maintaining accurate predictions, as well as efficiently modeling finer strain resolutions below 1% to get a better idea of the fine-grained strain response of TMDs from a theoretical standpoint.

It is important to continue accounting for phenomena and effects that are physically observed: for example, accounting for wrinkles in monolayers, dopants, defects, substrate effects, and in general, heterostructures, to better match experimental research. Significant research has already been performed on alloying, and it is important to view these effects not only in isolation, but also in relation to one another.

Besides biaxial strain, it is important to study uniaxial strain on TMDs. Uniaxial strain does not preserve symmetry of the Brillouin zone, causing difficulty in computing a succinct irreducible band path for the electronic structures. Still, electronic bandgaps and band nature may be extracted from DFT calculations over the reciprocal lattice mesh, and it is important to understand the electronic tunability under arbitrarily oriented uniaxial strains. This will reveal fundamental insights into the behavior of TMDs, and it is important considering that it is nonphysical to only consider strains in high-symmetry directions, for example, along the zig-zag or armchair directions of hexagonal lattices. This is important since a majority of current experimental strain studies focus on uniaxial strain, since it is much simpler to physically apply. While uniaxial strain is fundamentally similar to biaxial strain, albeit with lesser strain tunability, the trends in material behavior may not necessarily carry over.

Finally, while group-VI TMDs have historically seen the highest research interest, it is also important to extend computational studies to TMDs with transition metals beyond the group-VI family, for example with Zr, Hf, Ti, V, Nb, Ta, Re, Pt, Pd, etc. These materials and their heterostructures may exhibit novel electronic properties and quantum phenomena useful for future technologies.

Chapter 4

Experimental Methods

This chapter discusses the various experimental methods employed for fabricating, transferring, and straining TMD samples. Monolayer WS_2 and WSe_2 samples are grown using the metal-organic chemical vapor deposition (MOCVD) process. In essence, CVD fabrication involves a cylindrical furnace in which gaseous precursors are flowed through at a controlled rate. These precursors undergo a gaseous reaction, subsequently nucleating on a heated substrate and allowing for epitaxial film growth [67]. In MOCVD with TMDs, organic metal precursors such as $(NtBu)_2(NMe_2)_2M$ and $W(CO)_6$ are used for film growth. Possible chalcogen precursors include Et_2S_2 and $(CH_3)_2Se$. During synthesis, finely tuning the growth parameters (precursor ratios, gas flow, etc.) may result in substantial impacts in the kinetics and thermodynamics of TMD growth, causing drastic changes in the final products [67]. Thus, substrate coverage may be controlled, allowing for flake or monolayer film-like samples. For samples comprised of flakes, flake coverage and size may also be controlled.

TMD samples are grown on Si/SiO_2 substrates. Besides through thermal expansion and contraction, these substrates do not allow for mechanical strain, as a consequence of their extremely brittle nature. This requires that TMD flakes or films are transferred to external substrates for subsequent strain engineering. It is also important to encapsulate TMD samples, such that they are fully contained from above and below within a polymer stack. Past studies have demonstrated that encapsulation is crucial in mitigating slippage during strain experiments [4, 45].

Optical microscopy (OM) allows for directly capturing images of TMDs, up to a magnification of approximately 100×. This theoretically allows for optical calibration of strain methods for sufficiently high strains. Although this is outside the scope of this work, this is a promising direction to more accurately quantify and calibrate strains. Higher magnification is possible through either scanning electron microscopy (SEM) or transmission electron microscopy (TEM), directly allowing the measurement of TMD lattice constants.

4.1 Transfer Methods

Various transfer methods exist to transfer TMD monolayers from their silicon growth substrate to destination polymer substrates. These may be broadly placed into two main categories: dry transfer and wet transfer methods. Dry transfer methods do not introduce the TMD sample to any liquids (and are hence dry), while wet transfer methods utilize a liquid solution to assist with transfer. Between transfer methods, transfer yield and reliability may widely vary. The optimal transfer method largely depends on sample preparation and quality: this dictates the TMDs adhesion strength with the growth substrate. Generally, wet transfer methods are more reliable than dry transfer methods, although introducing samples to chemical solutions can sometimes result in unwanted effects and sample degradation. Additionally, older and oxidized samples are more likely to pose challenges during the transfer process compared with newly grown samples. For this reason, all samples measured and strained in this work are freshly grown, transferred, and measured within one week at maximum.

Dry Transfer

TMD dry transfer is simple multi-step process. The following dry transfer procedure assumes use of polycarbonate (PC) as the transfer polymer, but other polymers are also possible which may have slightly modified handling and curing procedures. Other polymer choices include poly(methyl methacrylate) (PMMA), polydimethylsiloxane (PDMS), polyvinyl alcohol (PVA), polypropylene carbonate (PPC), polyethylene naphthalate (PEN), polyethylene terephthalate (PET), polyimide (PI), NOA-61 adhesive, and SU-8 photoresist. Different polymers may also have different levels of adhesion, surface roughness, and "stickiness," in addition to flexibility and durability. Similarly, the procedure assumes use of single-sided thermal release tape (TRT) with a release temperature of 130°C, although tapes with other release temperatures are available (100°C, 150°C, etc.). These may yield differing results, depending on their adhesion strength. For example, the lower-temperature TRT tends to have a gentler release, which is desirable for TMD transfer. The full dry transfer procedure is as follows:

1. Score and break a silicon substrate with TMD growth to the desired size, for example a 1cm $\times$ 1cm square
2. Spin-coat TMD sample with a polymer film: for example, PC for 60s at 2000 RPM
3. Cure polymer on hot plate for $5 - 10$ minutes at 110°C to dissolve solvent (acetone)

4. Scratch edges of silicon substrate with a razor blade to ensure polymer does not cover substrate edges

5. Smoothly adhere TRT on top of the polymer layer, creating Si/SiO_2/TMD/PC/TRT stack

6. Gently and smoothly peel TRT from the substrate in one continuous motion

7. Adhere TMD/PC/TRT stack onto a new substrate, forming a Substrate/TMD/PC/TRT stack

8. Heat the stack at 10°C above the TRT minimum release temperature while applying pressure with a weighted aluminum block. This releases the TRT and yields an encapsulated Substrate/TMD/PC stack

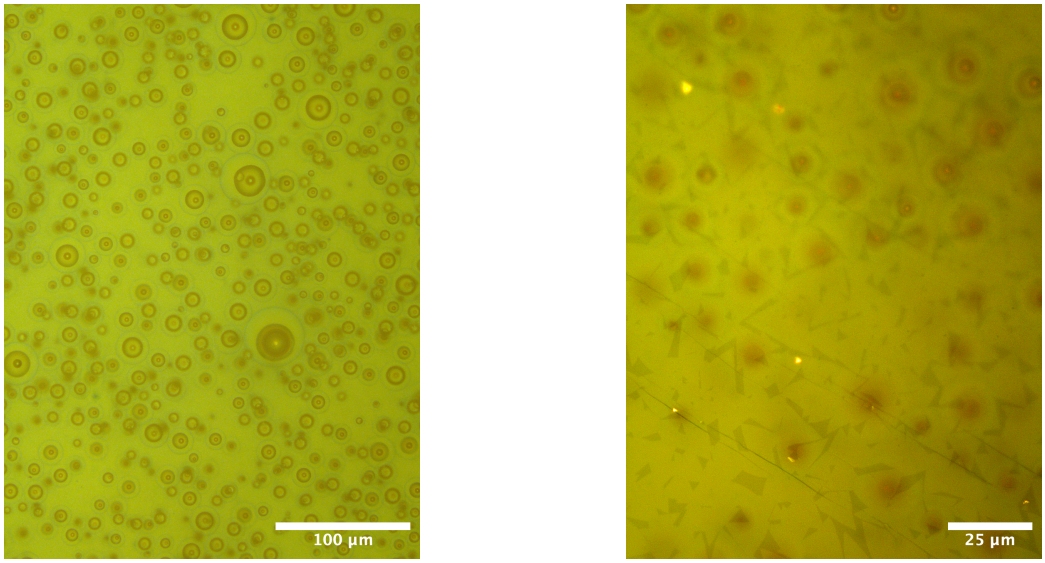

(a) (b)

Figure 4.1: **(a)** Optical microscope image of thermal release tape at 20× magnification. **(b)** Optical microscope image of a TMD-TRT stack at 50× magnification with successful WS_2 transfer to the TRT, before adhesion onto a destination substrate.

Between steps, it is important to spray the sample with the N_2 gun to ensure the samples are free from stray particles and contaminants. Fig. 4.1 displays optical microscope images of fresh TRT and the TMD–TRT stack after step six from above. The bubbles are the adhesive from the TRT, and the lightly colored triangles are the TMD flakes from the successfully transferred high-coverage sample. Once the TRT has been peeled from the silicon substrate, the TMD-polymer stack will visually have a slight yellow hue against the bluish/green of the TRT.

Fig. 4.2 displays three optical microscope images with various levels of success transferring WSe_2 flakes from an initial Si/SiO_2 growth substrate to a fresh silicon substrate. In Fig. 4.2(a), ripples of successful transfer are present, separated by regions of sparseness. This indicates one of two scenarios: (1) the thermal release tape was not adhered gently and smoothly onto the top polymer surface, or (2) the thermal release tape was not smoothly peeled from the silicon substrate. Regardless of the exact scenario, Fig. 4.2(b) displays the same sample in a region of more successful transfer. However, the flakes are significantly broken up rather than remaining pristine. Fig. 4.2(c) displays a different sample which was more successfully dry-transferred to a new substrate. This depicts that the dry transfer procedure can be very sensitive to the pressure applied to the sample during adhesion and peeling of the TRT-stack. While several samples were transferred with this method, a majority of attention was focused on the significantly more reliable wet transfer methods.

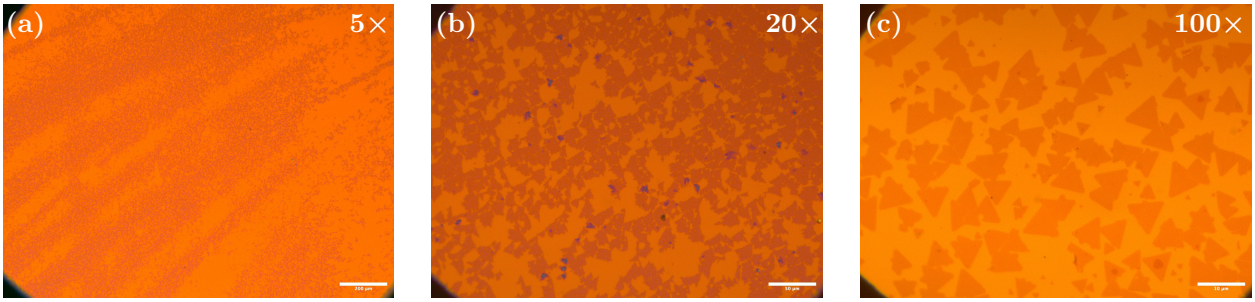

Figure 4.2: **(a-b)** WSe_2 sample after partially-successful dry-transfer to a new Si/SiO_2 substrate, at (a) 5× and (b) 20× magnifications. **(c)** Another WSe_2 sample more successfully dry-transferred to a new Si/SiO_2 substrate, at 100× magnification. Scale bars are $200\mu m$, $50\mu m$, and $10\mu m$, respectively.

Wet Transfer

There exist several variants of wet transfer methods, two of which will be described in this section. Both methods begin with the same fundamental steps as the dry transfer method.

The H_2O-assisted wet transfer method relies on the intercalation of water molecules between the polymer film and silicon growth-substrate. Importantly, this procedure uses de-ionized (DI) water. This process assumes that the TMD will be more strongly adhered to the polymer film rather than the silicon growth substrate, which may not be true for heavily oxidized samples. A schematic procedure for the wet transfer method is given in Fig. 4.3. Slightly peeling the film stack from a corner or edge can help improve water-intercalation during the water bath step. Then, the silicon substrate may simply fall off the TRT stack with gentle shaking. Alternatively, the film can be gently peeled after one to two minutes of submersion, as demonstrated in step six. After submersion, it is important to blow off

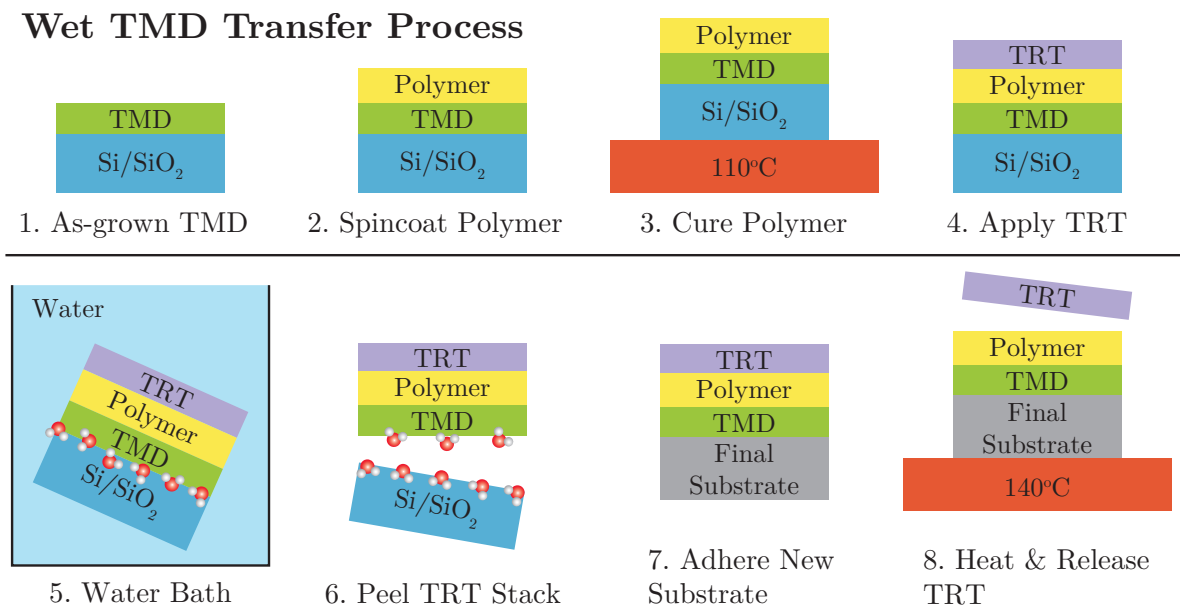

Figure 4.3: Diagram of the **H_2O-assisted** wet transfer procedure, demonstrating the main steps. The procedure is generally agnostic to the transfer polymer and the final substrate used.

any stray H_2O particles with the N_2 spray gun. Heating the TRT stack **below** the TRT release temperature is also useful to evaporate any remaining water (for example 60°C) before adhering the sample to the destination substrate.

While the H_2O-assisted wet transfer method has improved transfer yield and reliability compared with the dry transfer method, it still is not entirely robust and sometimes fails to transfer TMD samples. Thus, a modified wet transfer procedure using potassium hydroxide (KOH) is implemented for optimal reliability, as depicted in Fig. 4.4. A KOH bath with a ratio of 10g KOH to 30g DI water is used, corresponding to 25 wt% KOH. After step 4 in Fig. 4.4, the TRT-Si stack is transferred to a KOH bath instead of a water bath. KOH etches away at the substrate and oxide layer, naturally detaching the TRT-stack with the TMD adhered. Once the growth substrate detaches, the TRT-stack must be rinsed with DI water. As with the water-assisted method, if the stack does not naturally detach within $1-2$ minutes, peeling a corner of the polymer stack and gently shaking can help. While the KOH-assisted wet transfer procedure is highly reliable and efficient, it does have a potential drawback. The exposure of TMD samples to the corrosive environment of KOH may degrade sample quality. This downside is minimized since the TMD is only exposed to the KOH bath for several minutes before successful release, as opposed to 1-2 hours utilized in other similar procedures [68].

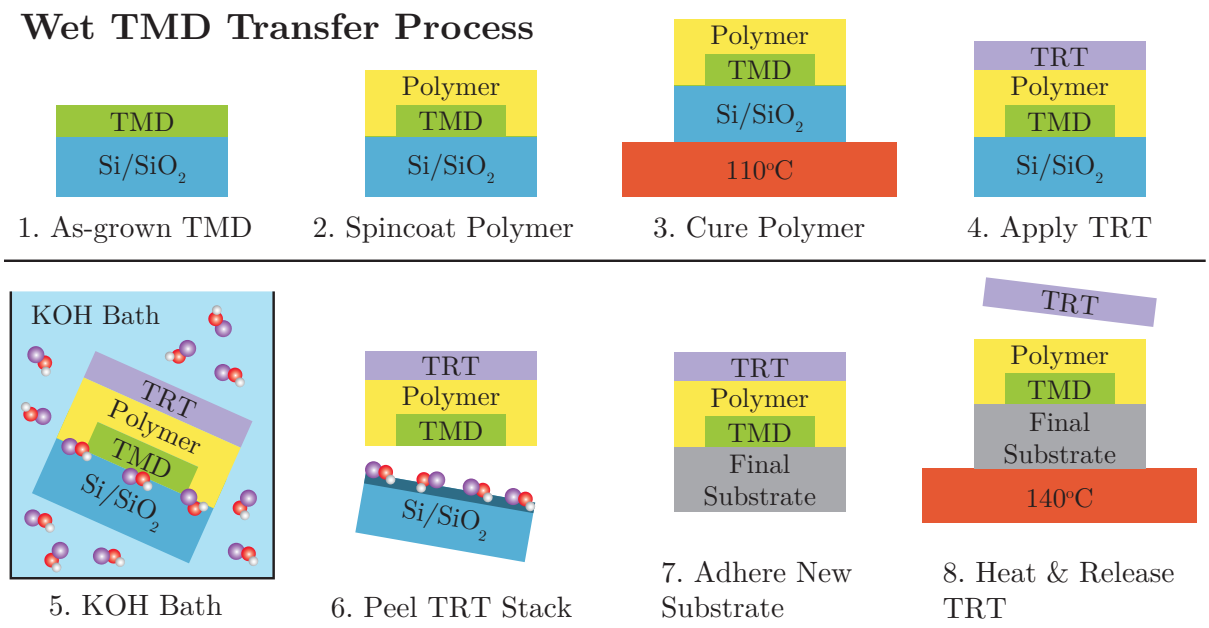

Figure 4.4: Diagram of the **KOH-assisted** wet transfer procedure, demonstrating the main steps. The procedure is generally agnostic to the transfer polymer and the final substrate used.

The TMD-TRT stack may then be transferred to a destination substrate such as PDMS or PET by gently adhering the TMD-TRT stack onto the destination substrate, trying to minimize air bubbles. The ideal final substrate depends on the intended process of straining TMDs: for bending experiments, PET is ideal; for elongation experiments, PDMS is ideal due to its elastomeric properties. The TMD-TRT stack is successfully transferred to PET films using this procedure, specifically the uncoated side of Melinex® ST504 125μm heat-stabilized PET films. Despite their heat-stabilization, these PET films heavily deform and warp for temperatures above 150°C, so it is preferable to use TRT with a 100°C or 120°C release temperature. The PET-TMD-PC stack is ideal for bending experiments: the PET film serves as a rigid yet highly flexible substrate.

For a more flexible substrate for use in elongation / stretching experiments, an elastomer like PDMS is ideal for the final substrate. In practice, the TMD-PC-TRT stack does not adhere well to cured PDMS, remaining adhered to the TRT even after thermal release. Thus, a modified procedure is developed to ensure sufficient encapsulation of the TMD during elongation experiments.

Before the KOH-assisted wet transfer is initiated, a PDMS sample is prepared in a 90mm petri-dish, using a $10:1$ ratio of base to curing agent of the SYLGARD™ 184 silicone elastomer product. A $6-8$g mixture yields an ideal thickness in the petri-dish of approximately

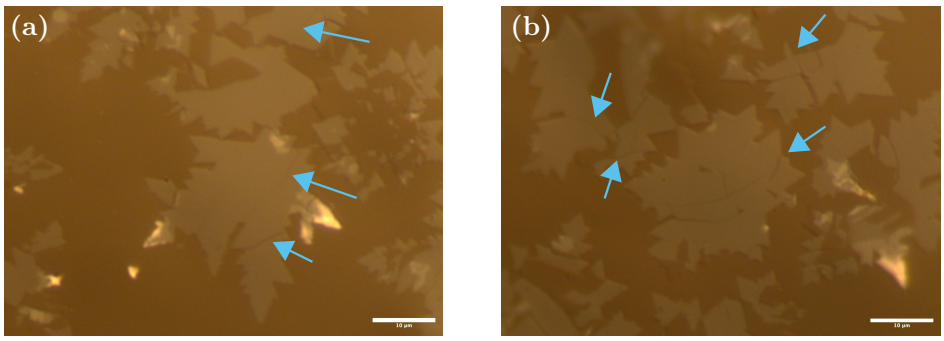

Figure 4.5: Optical microscope images at 100× magnification of two WSe_2 samples post KOH-assisted wet transfer to PDMS. Blue arrows point to cracks in the TMD flakes due to excessive pressure during the transfer procedure. Scale bars are $10\mu m$.

1mm. This mixture is mixed thoroughly and is set to rest for approximately one hour to get rid of bubbles and settle. Then, the PDMS should be heated for approximately 15 minutes at 90°C, or until it is just slightly sticky. The TMD-TRT stack isolated after the KOH step is then carefully placed atop the semi-cured PDMS, such that the TMD is directly in contact with the PDMS, attempting to minimize any bubbles between the layers. Finally, the sample can be heated at 90°C for another $10 - 15$ minutes to fully cure the PDMS.

After curing, the PDMS may be cut out from the petri-dish and placed on a glass slide. For about five minutes, this stack should be placed on a hot plate at a temperature above the TRT release temperature, with an aluminum weight applying consistent pressure. It is crucial that the glass slide is the top-most layer, such that the TRT is *directly* in contact with the hot plate. This is necessary, otherwise placing the glass slide on the hot plate consistently results in unsuccessful transfer. This likely results from the glass insulating the heat transfer to the TRT, causing a release with poor adhesion to the encapsulation polymer.

It is crucial not to apply excess pressure to the TMD-stack while adhering the TRT-TMD stack to the semi-cured PDMS, in addition to during the TRT release step. Excess pressure causes cracks to form in the TMD flakes, as demonstrated in Fig. 4.5. This is undesirable, so it is important to apply minimal pressure during the transfer procedure to avoid sample damage.

This transfer procedure is reliable with high yield, repeated many times without any difficulties. It is also robust to choice of TRT: tapes with release temperatures of 150°C and 130°C both are successful. However, as previously mentioned, the TRT with lower release temperature is preferred for its gentler thermal release. The KOH-assisted wet transfer yields a successfully encapsulated TMD sample, encapsulated above by PC and below by PDMS. This combines the ease of handling and flexibility of the elastomer PDMS with the higher Young's modulus PC ($>$ 1GPa), useful for attaining efficient strain-transfer.

4.2 Spectroscopy

Raman and photoluminescence (PL) spectroscopy are complementary techniques for probing the structural and electronic properties of TMDs through an incident laser beam. Raman spectroscopy is based on the inelastic scattering of incident photons by lattice vibrations, providing a simple way to measure the phonon modes. These phonon modes may be sensitive to sample thickness, crystal symmetry, strain, doping, and temperature. In TMDs, characteristic Raman-active modes, such as the in-plane and out-of-plane vibrational modes, allow for quantitative analysis of structural variations due to strain.

Photoluminescence spectroscopy probes the radiative recombination of photo-excited electron–hole pairs and is therefore directly sensitive to the electronic band structure. In TMDs, PL provides information on optical bandgap energy, excitonic states, and recombination dynamics. The strong PL response observed in monolayer TMDs, arising from their direct bandgap nature, makes PL particularly effective for distinguishing layer thickness and strain magnitude. Together, Raman and PL spectroscopy offer a powerful, non-destructive means of probing structural, vibrational, and electronic properties of TMDs. However, it is important that laser power is kept at a minimum, to minimize any potential sample damage caused by laser irradiation. In practice, this is only a concern for higher-power Raman measurements: no sample damage is observed for the PL experiments carried out in this work. This spectroscopy technique is used to measure strained TMDs, directly revealing the strain-induced modulation of their electronic band structures.

The in-house spectroscopy setup enables data capture using two main configurations: confocal-mode and line-mode. Confocal mode requires focusing the laser to a small circular spot, enabling the collection of localized data, for example at the center of a TMD flake. This produces a single Raman or PL spectrum. Line-mode effectively focuses the laser into a thin strip (actually a very stretched out oval), allowing for the collection of an array of spectra along the laser line, allowing for spatial analysis. The setup also has a stepper-controlled xy-stage, allowing for precisely collecting two-dimensional mappings of spectra by making small, fixed steps perpendicular to the direction of the laser-stripe.

Baseline correction is performed using the asymmetrically reweighted, penalized least squares smoothing algorithm (ar-PLS) [69]. This algorithm effectively attains a smoothed baseline which may be subtracted from the raw data, yielding a spectrum sitting flatly upon zero-intensity. Fig. 4.6 depicts a WS_2 Raman spectrum before and after the baseline correction step.

In practice, this algorithm significantly outperforms other baseline-correction methods, including standard penalized least squares, mitigating any ringing artifacts that may result

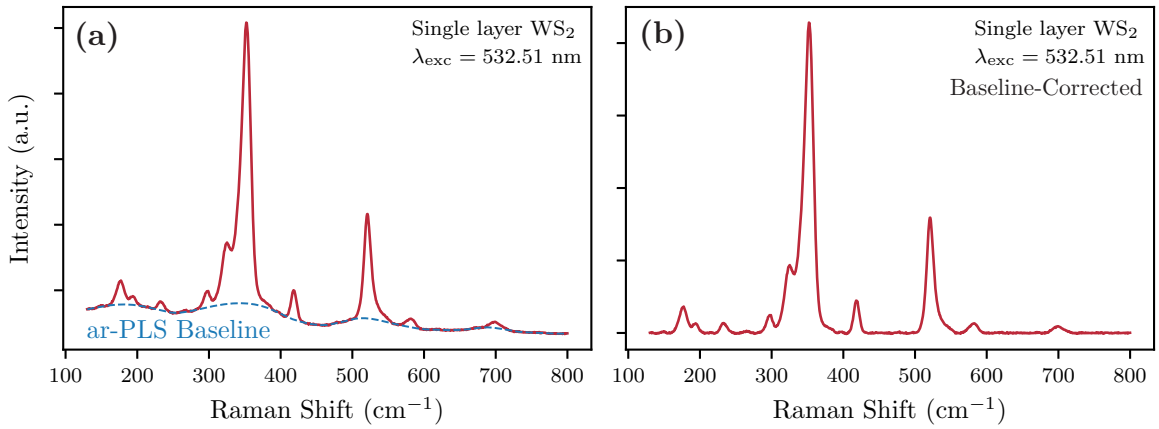

Figure 4.6: Raman spectroscopy measurements of a WS_2 flake, (a) before and (b) after, the ar-PLS baseline correction algorithm. The blue dashed line in (a) displays the extracted baseline.

from the smoothing process. The parameters of the algorithm are finely tuned for each spectrum, such that the spectra closely match the references. This is required due to the differing peak intensities for each Raman/PL measurement, anywhere from a few hundred counts at the peak positions to tens of thousands of counts.

4.3 Uniaxial Strain

This section presents the two methods used to experimentally apply uniaxial tensile strain to TMD samples – elongation (stretching) and bending. Due to the lack of a robust biaxial strain apparatus, this study is limited to uniaxial tensile strains which are fundamentally much simpler to apply.

Elongation experiments are conducted using a custom-built uniaxial strain apparatus developed by John Kim in 2025 [70]. The device applies tensile strain to rectangular samples using two opposing, thumbscrew-driven translation stages mounted on linear slides, as shown in Fig. 4.7. Samples are secured between opposing clamps, with additional set screws driven through the samples ends to ensure firm attachment and minimize slippage during deformation. With this apparatus, the distance between stages may easily be measured, and the tensile strain can be computed as $\varepsilon = \Delta d/d_0$ where d_0 is the separation for the zero-strain case.

A key limitation of this apparatus arises from the spring-loaded translation stages, which exert an outward force on the sample. In this configuration, the lead screws primarily constrain the stage positions rather than actively applying a tensile force driving the stages apart. As the screws are loosened, the springs drive the stages apart to induce elongation.

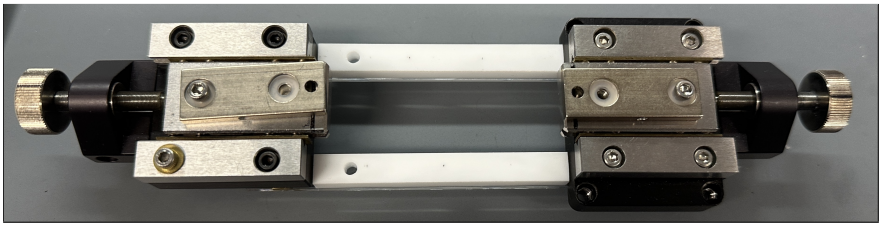

Figure 4.7: Custom-built uniaxial strain apparatus used to elongate rectangular samples. Two opposing clamps are mounted on spring-loaded translation stages along linear slides, with thumbscrews used to control the stage positions. As the screws are loosened, the springs drive the stages apart, applying tensile strain to the mounted sample.

However, if the sample or substrate is too stiff, the spring force may be insufficient to produce appreciable strain, and the stages will not fully separate. Consequently, this apparatus is best suited for compliant, flexible substrates, where the spring-driven motion can effectively translate into uniform tensile strain. This is ideal for samples transferred to PDMS substrates – however, samples on PET substrates may not be elongated since PET is too rigid for elongation with the apparatuses springs.

Next, the bending strain method is introduced. When a thin film is bent along a radius, its top surface experiences a uniaxial tensile strain while the bottom surface experiences a uniaxial compressive strain. This same principle may be applied to strain-engineering for TMDs: once transferred to a destination substrate, the substrate may be bent along different radii to induce uniaxial tensile strain on the TMD. As demonstrated in Table 2.1, bending has been the primary means of straining TMDs. In practice, bending may be achieved in various ways: complex 3- or 4-point bending apparatuses, deflection apparatuses, or simply bending a substrate along a defined radius. The most common method has been to utilize an apparatus such as the elongation apparatus, affixing the ends of the sample and decreasing the distance between translation stages such that the sample bends upwards. These methods often take physical measurements to estimate the bending curvature (for example, the height and length), alternatively capturing a photo and estimating with digital methods.

Fig. 4.8 presents a schematic view of bending experiments. From a theoretical standpoint, strain in a bending experiment depends on two parameters: the radius of curvature R and the sample thickness t. Thus, the tensile strain on the surface may simply be computed as $\varepsilon = t/2R$, although other models and derivations do exist [5, 30].

In theory, the elongation apparatus in Fig. 4.7 may be re-purposed to bend rectangular samples as presented schematically in Fig. 4.8(b). However, the optical microscope utilized for spectroscopy measurements does not have sufficient working distance for both the elongation apparatus plus the additional height of the bent sample (without complete deconstruction of the microscope stage). As such, more rudimentary bending experiments are

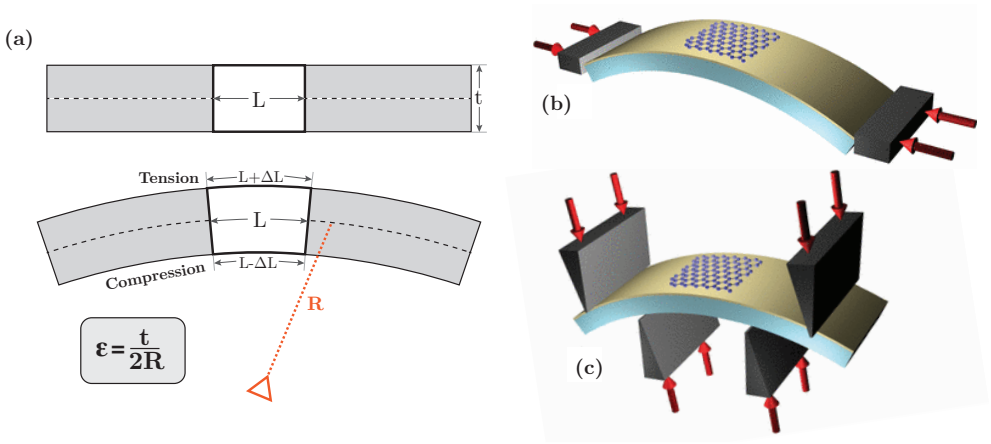

Figure 4.8: **(a)** Schematic diagram of the cross section of a flexible substrate before and after bending it along a radius R. The neutral plane is indicated by the dashed black line within the substrate. **(b-c)** Renderings of a flexible substrate with a two-dimensional material on its surface undergoing uniaxial tensile strain mounted to a two-point (b) and four-point (c) apparatus. Panels (b-c) are modified from [71].

performed by bending substrates over curves of known radii or arbitrarily bending substrates and adhering their ends to a base similarly to the two-point bending method presented in Fig. 4.8(b).

Chapter 5

Experimental Results

Baseline Raman and photoluminescence data of as-grown samples is collected to serve as a reference for future strained measurements. Both Raman and PL peaks are expected to move with strain, at varying rates according to the strain type (biaxial, uniaxial, etc.) and magnitude. By using both DFT results and past experimental literature, measuring the modulation of these peaks allows for convenient quantification of strain. It also allows for determining any modulation or unwanted effects that may be induced during the polymer-assisted transfer process. Due to its promising DFT-predicted strain tunability and established CVD growth procedure, WS_2 is selected for strain experiments in this study. WSe_2 is another compelling TMD, although previous computational results demonstrate lesser band tunability compared to WS_2.

Raman and photoluminescence measurements of as-grown WS_2 flakes are shown in Fig. 5.1, taken with a laser spot focused at the center of a triangular monolayer flake. The PL spectrum depicts an optical bandgap of 1.969eV, closely matching results from past literature [1, 72]. A multi-peak fitting algorithm is performed with two Gaussian functions in order to extract the exciton and trion peak positions, E_{A^0} and E_{A^-}, respectively. The difference in the exciton and trion peak energies,

$$E_{b,A^-} = E_{A^0} - E_{A^-} \tag{5.1}$$

is referred to as the trion binding energy [72]. For the data in Fig. 5.1(a), $E_{b,A^-} = 36\text{meV}$, directly in line with values from previous literature between $20 - 41\text{meV}$ [72], confirming robust sample quality. This also confirms a successful peak-fitting and measurement procedure, which is crucial for accurately extracting the exciton peaks from strained measurements.

The Raman peaks in Fig. 5.1(b) are identified through comparison with reference spectra from previous literature [73]. The Si peak may generally be used to align spectra, as this peak

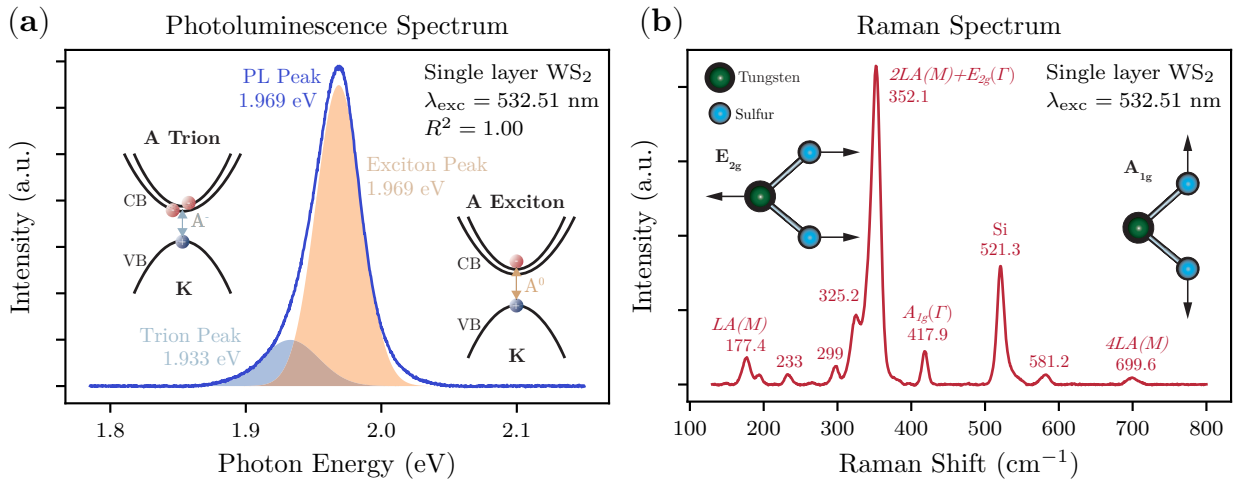

Figure 5.1: Spectroscopy measurements under a $\lambda = 532.51$nm laser source for an as-grown WS_2 flake. **(a)** Photoluminescence spectrum, separated into trion and exciton peaks. Inset band diagrams depict the quasi-particle dynamics at the K point of the Brillouin zone. **(b)** Raman spectrum, with peak Raman shifts labeled. Inset molecular diagrams depict specific vibrational modes of WS_2.

position *should* remain relatively constant across samples (although no shifting is necessary for the given spectrum).

Acoustic phonons correspond to collective atomic motion, for example both the tungsten and sulfur atoms stretching in the same direction. Conversely, higher energy optical phonons correspond to out-of-phase atomic movement, for example the two vibrational modes depicted in Fig. 5.1(b). The prominent longitudinal acoustic (LA) vibrational modes correspond to low-energy phonons traveling within the lattice plane, caused by an excitation wavelength near resonance. Both the A_{1g} and E_{2g} at the Gamma-point are present in this analysis: these Raman-active modes are highly tunable with strain, allowing for another convenient way to quantify and measure a TMD's strain. However, as a consequence of the laser emission wavelength used for optical analysis, the $2LA(M)$ and E_{2g} peaks highly overlap: this requires de-convolution to separate the peaks, which can introduce numerical error from the fitting procedure. This poses difficulty, considering the E_{2g} mode represents the in-plane vibrations, which are particularly relevant for in-plane strains: this mode tends to see greatest strain-modulation [74, 75]. Due to the challenges associated with Raman spectroscopy (overlapping peaks, larger laser power risking sample damage, etc.), this work will primarily focus on PL spectroscopy for strain-related experimentation. There is also greater experimental literature available for PL modulation compared to Raman measurements, as demonstrated in Table 2.1 and Table 2.2, allowing improved contextualization of results.

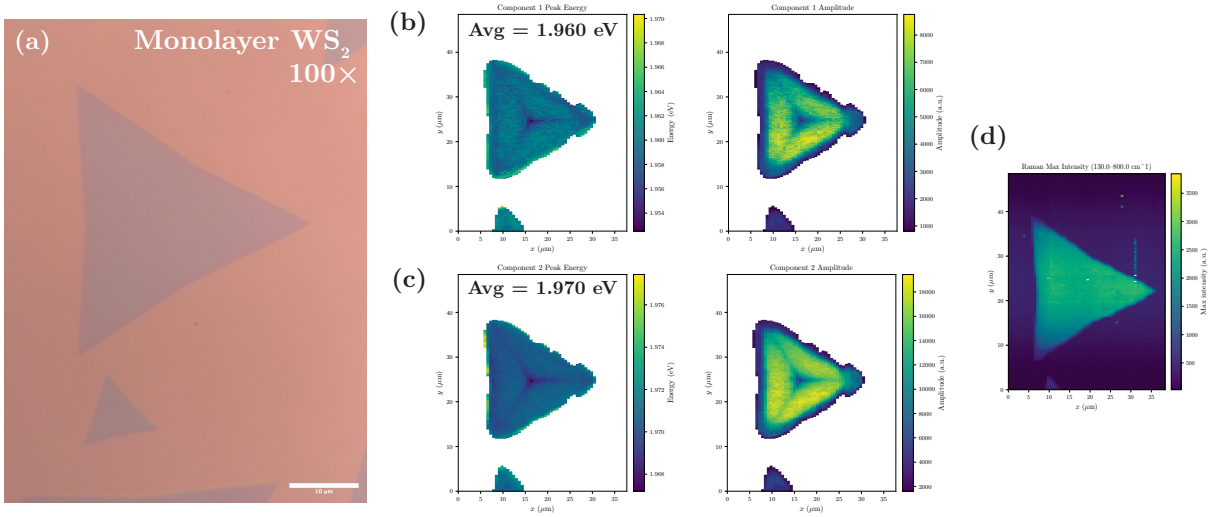

Figure 5.2: Two-dimensional PL and Raman maps for an as-grown WS_2 sample, with a line scan step-size of 500nm. (a) Optical microscope image of sample at 100× magnification, scale bar is 10μm. The side-length of the flake is roughly 30μm. (b-c) Photoluminescence energy and amplitude maps fitted to the (b) trion and (c) exciton peaks. (d) Raman mapping of maximum intensity at each spatial position, corresponding to the $2LA(M) + E_{2g}(\Gamma)$ peak.

Two-dimensional PL and Raman mappings are also depicted in Fig. 5.2 for an as-grown WS_2 sample. After baseline correction, the PL-peaks are fitted to a two-gaussian function to extract the exciton and trion contributions, as previously. These peak energies are highly consistent over the flake, with a *very slight* decrease in photoluminescence energy and amplitude at the center of the flake, effectively splitting the flake into three isosceles triangles. This pattern is consistent with past PL analyses of as-grown WS_2 flakes [76]. This sample has a lower estimated $E_{b,A^-} = 10.9$meV, significantly lower than the previously analyzed sample.

The Raman maximum intensity mapping also depicts high consistency over the entire flake. The Raman map has better defined edges compared to the PL maps which slightly smear out the results. Significantly higher laser-power is required for the Raman mapping, which also results in an increase in noise and anomalies in the data (for example, the vertical streak of high intensities at around $x = 30\mu$m).

Similar mappings are created for WS_2 and WSe_2 flakes transferred to PDMS and encapsulated with PC using the KOH-assisted transfer method. Several mappings are captured at the same locations, demonstrating negligible sample damage after analysis. The same spectroscopy setup parameters are recorded and utilized for the remaining experimental analysis. This is important such that flakes are not damaged during optical analysis in strain experiments, where repeated measurements are taken. Together, these mapping techniques

demonstrate reasonable photoluminescence and Raman consistency across the flakes. As a result of this consistency, the remainder of spectroscopic strain measurements are done in confocal mode due to its simpler procedure and lesser sample laser-irradiation.

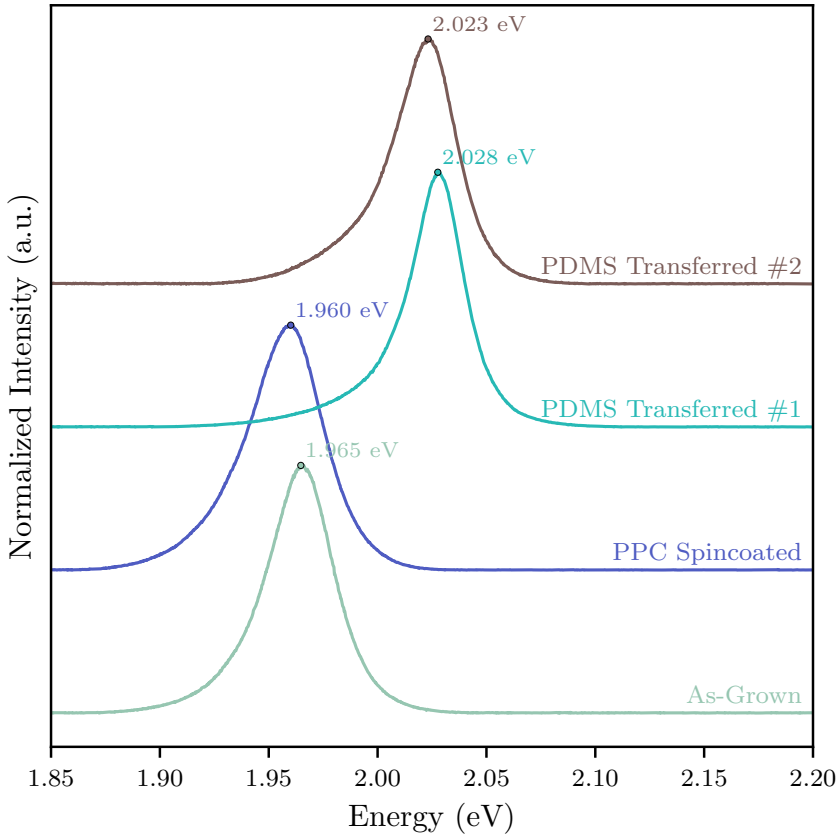

Figure 5.3: Photoluminescence (PL) spectra of a WS_2 monolayer measured at successive stages of a polymer-assisted wet-transfer process, including as-grown, PC spin-coated (*incorrectly labeled as PPC*), and two independent PDMS transfer instances. Each spectrum is baseline-corrected, normalized to its maximum intensity, and vertically offset for clarity. Peak positions are labeled with their corresponding PL energies.

After KOH-assisted transfer and polymer encapsulation, there is a noticeable shift in the PL spectrum. Fig. 5.3 demonstrates the PL of a WS_2 sample at successive stages of the transfer process. The as-grown PL peak is at 1.965eV, consistent with the results in Fig. 5.1. After spin-coating and curing PC, the PL is about 5meV less than the as-grown measurement, although this is likely due to flake-to-flake variations rather than an actual shift in PL. The sample is then transferred to PDMS using the KOH-assisted wet transfer procedure described in Sec. 4.1. Consequently, there is an observed shift in the as-grown PL peak of 63meV. From the same CVD-grown TMD sample, another sample is prepared and transferred – this causes the same PL shift, this time slightly less at 58meV, depicted as the

second transferred sample in Fig. 5.3.

Comparable PL blue-shifts are consistently observed when transferring samples to PET or PDMS using the wet-transfer procedure. Wang et al. follow a similar KOH-assisted transfer procedure with WS_2 using PDMS as a destination substrate, recording a 53.8meV blue-shift in the PL, from 1.970eV to 2.023eV [77]. This result very closely matches the observed trend, and the most plausible cause of this PL blue-shift is strain-relaxation during transfer. Furthermore, there is likely a certain degree of strain intrinsic to the CVD-grown flakes; however, once the flakes are transferred from the Si/SiO_2 growth substrate, the strain may relax. Wang et al. also indicate that the KOH-bath during the transfer does not have any unwanted strain-related effects on the WS_2 flakes [77].

5.1 Strain Engineering

Strain engineering experiments are conducted with WS_2 samples to investigate its experimental tunability compared with past experimental and computational studies. While biaxial strain has significantly greater strain tunability compared to uniaxial strain, it is also much more difficult to apply experimentally without a complex apparatus. As such, this work evaluates WS_2's uniaxial strain tunability, using both elongation and bending methods. The KOH-assisted wet transfer method is used for all experiments within this section.

Previous studies have demonstrated that uniaxial and biaxial strain gauge factors will differ by approximately a factor of two [57]. Since this work predicts a bandgap shift rate of about -107.1meV/% for $0 \rightarrow 1\%$ biaxial tensile strain on WS_2 (see Sec. 3.2.4), uniaxial strain is predicted to have an approximately -54meV/% gauge factor for small tensile strains. This value is strongly aligned with previous computational studies which predict uniaxial tensile gauge factors of around -64meV/% for monolayer WS_2, although the precise value depends on the exact methodology [31].

For WS_2, the reported methods in Table 2.1 demonstrate a median A-exciton tunability of -42.85meV and a median gauge-factor of -43.5meV/%. This is thus the target tunability for uniaxial tensile strain in this paper. To reach this goal, various substrates are tested, as well as carrying out both elongation and bending experiments.

5.1.1 Elongation

Using the KOH-assisted transfer procedure, a WS_2 sample is prepared on PDMS, encapsulated by PC. Before mounting the sample on the strain-apparatus, a reference PL measurement is taken indicating a peak position of 2.031eV, consistent with previous measurements.

Then, the sample is mounted on the elongation apparatus: a slight pre-strain must be applied to ensure that the flexible substrate is flat and uniformly mounted. This is considered the zero-strain point: as the apparatus is adjusted, the separation between the translation stages is measured so that the nominal tensile strain may be calculated as $\varepsilon = \Delta d/d_0$ where d_0 is the separation at the zero-strain case. At each strain level, several random flakes are measured across different regions of the sample to ensure robust results.

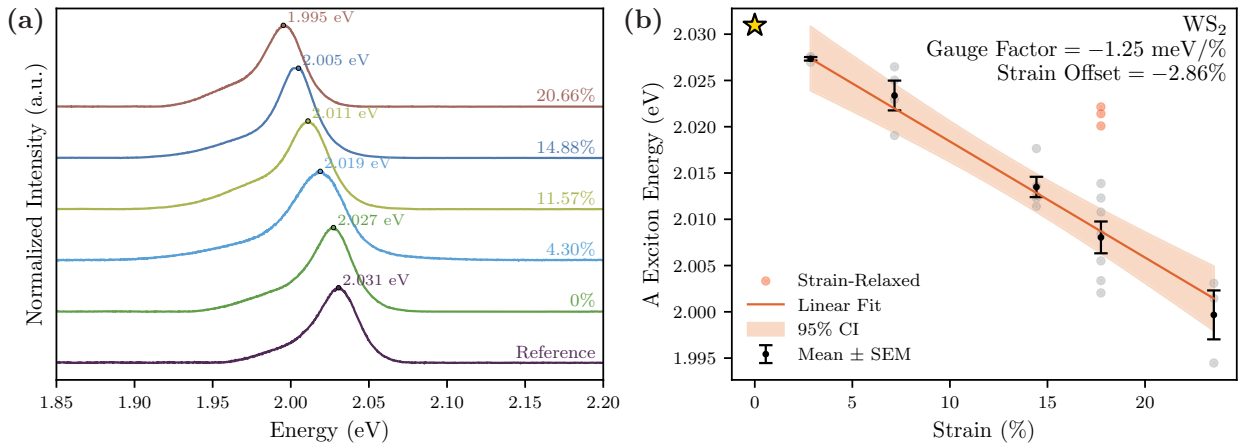

Figure 5.4: Strain-dependent PL response of monolayer WS_2 on a PDMS substrate encapsulated by PC under varying uniaxial tensile strains. **(a)** Stacked, normalized PL spectra at increasing strain, vertically offset for clarity. Peak energies are labeled, and the selected spectra correspond to measurements exhibiting the largest strain-induced red-shift. **(b)** Extracted A-exciton energies as a function of strain. Light gray points show individual measurements, while black markers with error bars denote the mean energy at each strain with standard error of the mean (SEM). The orange line represents a weighted linear fit to the averaged data, with the shaded region indicating the 95% confidence interval. Red points correspond to strain-relaxed flakes and are excluded from the fit. The gold star marks the reference sample measured prior to mounting on the strain apparatus.

Fig. 5.4 depicts the results of the elongation experiment. Fig. 5.4(a) presents the PL spectra of the reference measurement and at various strain levels. The strain values reported are simply ε from above and are not corrected for the slight pre-strain induced by mounting the sample on the apparatus. Since multiple flakes are measured at each strain level, the flakes with the largest strain-induced red-shift are selected for plotting (besides at zero-strain, where the spectra with maximum peak energy is selected). This demonstrates a monotonic trend in the PL peak positions: the peak is consistently modulated as the strain increases. From the un-mounted measurement to the flake with maximal red-shift, there is a maximum peak modulation of $\Delta E_{\text{peak}} = -36\text{meV}$ and a maximum A-exciton modulation of $\Delta E_{\text{A-exciton}} = -36.48\text{meV}$. This is significant modulation, falling well within the range of prior experimental results presented in Table 2.1. However, the modulation does not quite

reach the goal of 42.85meV of red-shift.

Fig. 5.4(b) plots the A-exciton energies across all of the measured flakes and strain levels, as well as linearly fitting the data. Individual PL measurements at each strain level (light gray points) show a small degree of scatter, while the mean values provide a reasonable estimate of the strain-induced trend. Data points identified as strain-relaxed flakes (in red) deviate from the primary trend and are therefore excluded from the fit. This strain-relaxation behavior is consistent with previous experiments in literature where the A-exciton energies blue-shift once a certain threshold strain is reached where slippage or fracture occurs [9, 43]. Not all flakes experience this relaxation, however, and higher strains are attained with greater modulation – this may be explained by varying flake orientations, as well as potential inconsistencies or defects in the PDMS or TMD surfaces. For example, Zhang et al. demonstrate the orientation-dependent fracture of WS_2 flakes under large uniaxial tensile strain [43].

The A-exciton energy exhibits a clear linear red-shift with increasing uniaxial tensile strain, consistent with strain-induced bandgap narrowing in monolayer WS_2. A weighted linear regression is performed on the averaged data, yielding a gauge factor of approximately $\sim -1.25\text{meV}/\%$. The regression weights are $1/\sigma^2 \sim 1/(\text{SEM})^2$, estimating the uncertainty of the associated means. This experimental gauge factor falls short of the target -40 to $-60\text{meV}/\%$ based on previous literature and this work's computational results. However, this gauge factor *exactly* matches the value estimated from Zhang et al.'s data, where they also elongated WS_2 on a PDMS substrate (although un-encapsulated) [43]. Even if the strain transfer efficiency of WS_2 on PDMS is considered as $\approx 10\%$ [25, 26, 43], the effective gauge factor is still quite low at $-12.5\text{meV}/\%$, although it is then the correct order of magnitude.

One note about Fig. 5.4(b) is the strain offset: because of the slight pre-strain on the sample when it is mounted on the apparatus, the PL at 0% nominal strain has a slight red-shift compared to the reference. By aligning the fitted linear model to this reference, an effective strain offset of approximately -2.86% is extracted and used to correct the strain-axis such that the reference falls at zero-strain. This value is subtracted from all strain-values in Fig. 5.4(b) to account for the offset. After accounting for the offset, the strain axis may be understood as the true mechanical strain experienced by the TMD.

Using the median WS_2 uniaxial tensile strain gauge factor of $-43.5\text{meV}/\%$, we may also calculate the *actual* maximum strain that the TMD experiences considering its -36.48meV A-exciton modulation. This yields an *estimated* maximum strain of 0.858% corresponding to a strain transfer efficiency of just 3.6% when considering the strain-offset. This is an exceptionally poor strain transfer: while this experiment demonstrates viable PL tunability, it also demonstrates that significant work in substrate-engineering and transfer methodology

may yield immensely improved results, potentially allowing for much greater strain tunability.

Another alternate strain experiment is conducted with another WS_2 sample using an identical transfer procedure and methodology. However, the maximum nominal strain of 17.19% only achieves a maximum PL peak modulation of -20.1meV with a maximum A-exciton red-shift of -19.37meV. This modulation would *theoretically* correspond to a gauge factor of -1.17meV/%, although the actual fitted gauge factor in Fig. C.1 is far less at -0.87meV/% due to the scatter in measurement from different flakes. The strain results for this experiment are very inconsistent, although further plots and data are presented in the appendix in Fig. C.1 and Table C.2. This alternate experiment yields similar order of magnitude, albeit worse results compared to the main elongation experiment. Fitted PL data for the main and alternate elongation strain experiments are provided in Appendix C.1.

In an attempt to improve the strain transfer efficiency of the strain experiments, PDMS substrates are coated with various polymers including PC, PVA, PMMA (A5), PBC (poly-(butylene carbonate)), and SU-8. This is tested since the elongation apparatus requires a flexible substrate: however, strain is best transferred to TMDs from materials with higher Young's moduli, hence the attempt at surface treatments. However, these polymers do not successfully adhere to the PDMS – while PC showed the most promising adhesion, the sample was extremely fragile and the PC layer easily peeled when manipulated or stretched. Various PDMS base to curing agent ratios are also experimented with, although the optimal $10:1$ ratio yields optimal substrate reliability and quality.

Thus, further work is required in finding the optimal substrates for TMD elongation experiments to achieve higher strain transfer efficiency. To circumvent the limitations of the elongation apparatus, bending tests are also experimented in the following section, testing a different means of applying strain to TMD flakes.

5.1.2 Bending

As presented in Fig. 5.5, a preliminary bending experiment is conducted with a WS_2 sample bent over a glass vial of radius $r = 13.5$mm. The WS_2 sample is prepared through the typical KOH-assisted transfer process, prepared on a PDMS substrate and encapsulated with PC. Fig. 5.5(a) displays an optical image of a flake on this sample – while the flake has visible cracks, likely due to excessive pressure during the transfer process, it is sufficient for this preliminary experiment. PL measurements for this specific flake are measured in unstrained and strained configurations. The reference measurement depicted in Fig. 5.5(b) demonstrates the PL peak position of 2.028eV, in line with other transferred sample measurements.

Then, the same sample is bent around the glass vial, as shown in Fig. 5.5(c). Due to

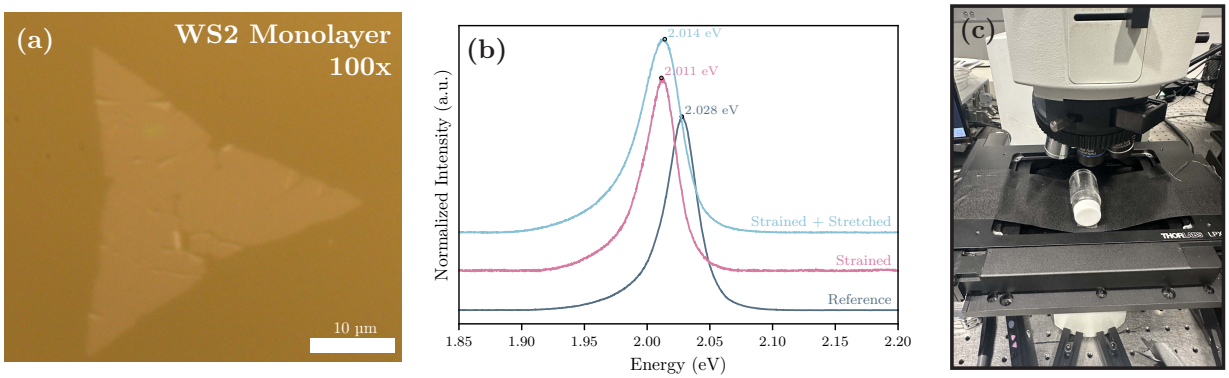

Figure 5.5: **(a)** Optical image (100×) of a monolayer WS_2 flake on a PDMS substrate with PC encapsulation, with an approximately 36μm side-length. **(b)** Stacked, normalized photoluminescence spectra for the reference (unstrained), bent (strained), and bent with additional stretching scenarios, with peak energies labeled. **(c)** Experimental setup for in-situ measurement of bending-induced strain, in which the sample is bent over a glass vial of radius 13.5 mm.

the inherent "stickiness" of the PDMS substrate, there is sufficient adhesion to the glass vial without any outside glue, tape, or adhesives. The PDMS sample is not stretched around the vial: it is simply bent without imposing any elongation strain. This strain-condition yields a PL peak shift of -16.3meV and an A-exciton modulation of -16.4meV compared to the reference spectrum. This demonstrates successful strain transfer to the TMD flake using the bending method. In an attempt to further strain the TMD flake, the sample is removed from the vial and is pre-stretched before re-adhering it to the vial and affixing it with tape. The resulting spectra is labeled "Strained + Stretched" and causes a slight blue-shift of the PL compared to the strained case; compared to the reference, there is a -13.6meV peak shift. This indicates that the sample experiences slippage and slight strain-relaxation with this increased strain rather than enhanced modulation. Since the flake is tracked visually, it is verified that the flake does not undergo fracture during this experiment.

To compute the *actual* strain on the surface of the PDMS due to the bending, the thickness of PDMS must be estimated. The 7.002g PDMS sample was prepared in a standard 90mm petri-dish. Using the known density of PDMS $\rho = 0.965\text{g/cm}^3$ from the manufacturer, its thickness may then be estimated: the volume of 7.002g of PDMS is $V = m/\rho = 7.25595855\text{cm}^3$ and the cylindrical interior of the dish has area $A = \pi r^2 = 63.6172512\text{cm}^2$, yielding an estimated thickness of $t = V/A = 1.14$mm. Thus, the nominal uniaxial tensile strain that the TMD experiences is approximately $\varepsilon = t/2R \approx 4.22\%$ since the TMD sits on the surface of the PDMS. Because the TMD's polymer encapsulation layer can be considered much less thick compared to the PDMS, the overall sample neutral-plane

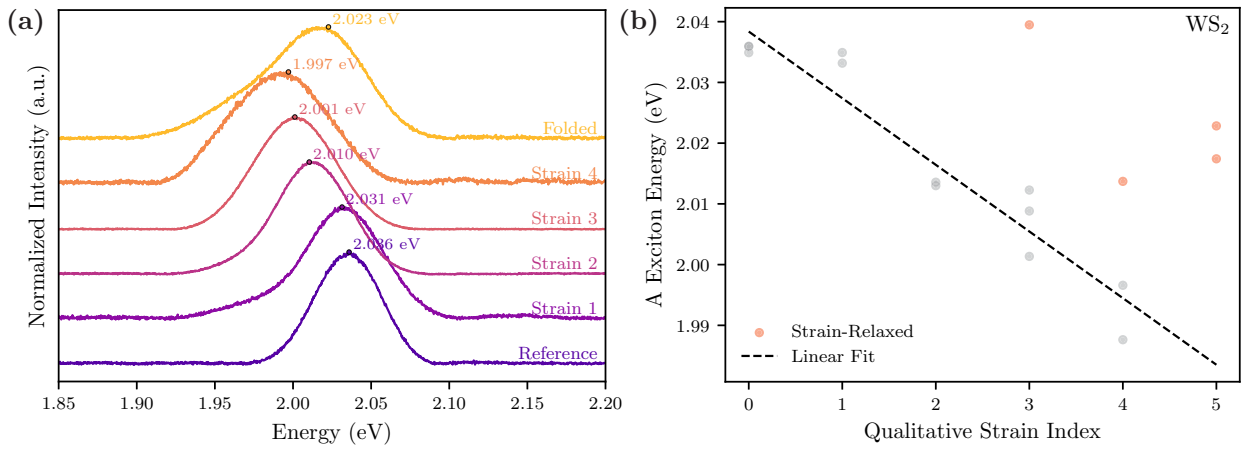

Figure 5.6: Qualitative strain-dependent PL response of monolayer WS_2 on a PET substrate encapsulated by PC under varying uniaxial tensile strains. **(a)** Stacked, normalized PL spectra at increasing strain, vertically offset for clarity and color-coded to indicate increasing strain. Peak energies are labeled, and the selected spectra correspond to measurements exhibiting the largest strain-induced red-shift. **(b)** Extracted A-exciton energies as a function of qualitative strain index. Light gray points show individual measurements, red points correspond to strain-relaxed flakes. A linear fit is performed as a guideline of the monotonic strain trend.

may be considered as roughly the neutral-plane of PDMS, validating the $\varepsilon = t/2R$ model.

Considering the "strained" scenario, this experiment corresponds to a gauge factor of $-3.89\text{meV}/\%$, which is significantly improved compared to the elongation experiments. This new gauge factor would correspond to a $-38.9\text{meV}/\%$ gauge factor considering a $\approx 10\%$ strain-transfer efficiency of PDMS, aligning much better with the median gauge factor of $-43.5\text{meV}/\%$ from the experimental results surveyed in Table 2.1. This demonstrates significantly better strain transfer efficiency in the bending regime compared to the elongation experiments, showing promise with the bending method.

A second bending experiment is performed using a PC-encapsulated WS_2 sample supported on a 125μm PET substrate. As in the main elongation experiment, several random flakes are measured at each strain level. The objective of this experiment is to probe the maximum PL tunability achievable under strain; as such, the applied strain is not quantitatively calibrated and the levels are qualitatively recorded rather than measured. Strain is introduced incrementally by progressively bending the substrate and securing its ends to a rigid cardboard support with tape, thereby inducing tensile strain in the central region of the sample containing the WS_2 flake. This method is not continuous and may only apply discrete strain levels; an improved, calibrated apparatus compatible with the spectroscopy setup would resolve this challenge but is outside the scope of this work.

Fig. 5.6 demonstrates the results of the second bending experiment. As shown in Fig. 5.6(a), the PL peaks monotonically increase from the reference measurement until strain level 4. Note that although the strain levels are incremental and the trend is monotonic, the strain levels are not necessarily linear. This demonstrates a maximum PL peak shift between the reference and strain level 4 of -43.8meV and a slightly larger maximum A-exciton shift of -48.3meV. The exciton energy is slightly more robust since it explicitly involves peak-fitting – due to slightly noisy data near the peaks, the PL-peak energies are not as robust. This A-exciton red-shift is larger than the maximum value attained from the elongation experiment. Notably, it is also larger in magnitude than the median value from literature of -42.85meV. This solidifies that the bending method is extremely promising for measuring strain-modulated TMDs, and the transfer procedure using PET as a destination substrate is also validated. Although the gauge-factor is inconclusive due to the unknown nominal strain levels, this experiment likely demonstrates that PET has improved strain transfer efficiency compared to PDMS due to the higher overall tunability, in line with theoretical expectations.

For the final strain level, a crease is formed in the PET substrate such that there is a fold at the center where the WS_2 is located. While this certainly increased the strain on the TMD, this resulted in strain-relaxation as indicated by the blue-shift of the PL peak to a value between strain levels 2 and 3.

Data for all of the measured flakes from this experiment is presented in Fig. 5.6(b). There are several measurements that are clearly strain-relaxed and are marked in red: these occur starting at strain level 3, although this behavior is clearly very flake-dependent. A linear guideline is shown as a guide to the eye: while the strain increments are not necessarily linear, the guideline demonstrates the clear monotonic trend for the red-shifting of the A-exciton peaks. The full peak-fitted PL data for this bending experiment is provided in the appendix in Table C.3.

Several other bending experiments are carried out to evaluate various substrates, with limited success. For example, a large sample is prepared using an entire CVD-grown sample by performing the KOH-assisted transfer method with PC as the encapsulation polymer. The TRT is used as the bending substrate rather than transferring the TMD to a destination substrate and releasing the tape. However, TRT has a strong, undesirable PL background greater than $50,000$cts, limiting measurement capabilities for the TMD's PL. Another sample is prepared using the standard KOH-assisted transfer procedure, transferring to a PMMA-coated PET substrate. However, there were again spurious PL peaks that directly interfered with WS_2's peaks. These spurious peaks are likely caused by some kind of diffraction-related effects or Raman modes of one of the polymers.

Finally, there is one last bending experiment with quantifiable strain levels, albeit with

less PL tunability than reported above. A sample is prepared using the standard KOH-assisted transfer procedure, transferring to a PC-coated PET substrate. The TMD is effectively sandwiched by PC using this method, which should in theory have a high strain transfer efficiency. To easily bend the sample over quantifiable strain levels, plastic substrates were affixed to glass slides with hot-glue at three distinct radii of curvature. Although this only allows for strain modulation at discrete levels, it is a proof-of-concept for the ability to quantify strain from bending experiments.

This experiment unfortunately suffers from very noisy data and spurious PL peaks: as such, limited data is successfully collected. The full results are demonstrated in the appendix in Fig. C.2 and Table C.4. This experiment yields a maximum PL peak shift of -15.5meV and a maximum exciton shift of -13.6meV, in line with the preliminary experiment's results. Notably this experiment has the same PL peak at 2.023eV as the folded substrate scenario in Fig. 5.6, indicating internal consistency between bending experiments. Unfortunately, even though the bending radii are known the strain cannot precisely be computed – there are no precise measurements of the PC film coating on the PET substrate. Still, this may be estimated based on the 2000RPM, 60s spincoating of dilute PC on the PET substrate. The PC layer is likely on the order of several microns at maximum [78], which is negligible mechanically compared to the PET thickness and is hence ignored for the strain calculations. Notably, the PET substrate does not appreciably change in thickness after coated with PC supporting this conclusion. Even if this estimate is poor, this only changes the estimated strain ($\varepsilon = t/2R$) by a constant factor. Using this reasoning, the maximum strain attained in this experiment was by bending the sample over a radius of 12.25mm, equating to 0.51% strain. Notably, despite the noisy data, this experiment yields an estimated (un-corrected) gauge factor of -19.62meV/%. This is significantly higher than any of the gauge-factors computed from PDMS-based experiments. While this value is still about half of the experimental values reported in literature, it verifies that PET+PC has significantly improved strain transfer efficiency compared to PDMS and is a promising substrate combination for future strain experimentation.

5.2 Limitations and Future Work

The experimental strain engineering performed in this work has several main limitations. For example, to carefully quantify strain-induced bandgap modulation, the strain evolution of specific flakes should be analyzed, rather than analyzing many random flakes throughout the sample. While this does demonstrate the overall trends, it is not ideal. This work also does not consider strain with relation to TMD flake-size and orientation. These are two more

factors that likely impact the exact strain tunability, with further research necessary to best understand their impacts. The main cause for these limitations is the strain methods used. Both the elongation and bending methods required slight disassembly of the spectroscopy setup, causing limited use of the xy-stage with only one remaining direction of travel. This caused extreme difficulty in alignment and focusing, requiring a lot of manual adjustment and fine-tuning. While the elongation apparatus was quite robust and would theoretically allow for systematic studies, the bending methodology was quite elementary. The nature of the bending experiments made it nearly impossible to successfully focus and align flakes, with very poor optical clarity and contrast. The sample would very often drift and if the sample surface was not entirely flat, focusing was quite difficult especially with the limited xy-tunability. A new apparatus for continuous two-point bending compatible with the Xie group's spectroscopy setup would help achieve continuous and easily quantifiable bending strain. Alternatively, a more adjustable, modified microscope stage for use in strain experiments would be exceedingly helpful. Furthermore, calibrating the bending apparatuses strain and precisely measuring film thicknesses would allow for much more precise strain determination from the bending method.

Besides the clear limitations in the apparatuses, there are several limitations and potential improvements in the transfer procedure. Further work is still needed in the area of substrate-engineering to find optimal substrate combinations with high strain transfer efficiency. This work clearly indicated the PC-PC "sandwich" as a viable combination (PET+PC substrate and PC encapsulation), although according to past literature there should be several other promising combinations that alleviate the low strain transfer efficiency of PDMS, for example using PVA. Besides the substrate, implementing an annealing procedure post-transfer may also help achieve improved strain tunability by reducing TMD slippage. For example, a previous work demonstrated that annealing at 100°C for 3 hours improved their uniaxial gauge factor from -12.7meV/% to -51.9meV/% for a WSe_2 sample on a PC substrate [45]. Another work similarly finds a 133% increase in gauge factor through annealing post polymer-assisted transfer [79]. Annealing may also help increase the TMD photoluminescence; Wang et al. find that KOH heavily suppresses PL intensity, finding that annealing is a viable pathway to improve sample luminescence [77]. While the samples are only exposed to KOH for a short period of time during transfer (< 5 minutes), it still likely somewhat diminishes the PL according to this result. Thus, annealing is a simple step that may yield significantly enhanced strain tunability of TMDs.

In a broader sense, there is still significant progress to be made in the field of experimental TMD strain engineering. This work demonstrated the sub-optimal strain transfer efficiency of current methods, as well as the highly inconsistent results reported in literature.

Researchers must continue improving methods of strain transfer efficiency, realizing higher strains and consequently improved range of electronic tunability. Further work is especially needed on biaxial strains, specifically biaxial compressive strains, where there has been a lack of experimental research. Biaxial strains beyond -1.2% have not been realized on MoS_2 [8], causing uncertainty in the modulation of their electronic band structures (i.e., is the maximal bandgap at a slight compressive strain, after which the bandgap narrows?). Considering the extremely varied results between experimental strain engineering methods, significant methodological and procedural improvement is also necessary.

Beyond methodological improvements, it is important to focus experimental strain engineering on heterostructures and more complex devices. While uniaxial strain has largely been applied on single-material samples, focusing more attention applying strain to devices may realize practical applications.

Chapter 6

Future Applications

While there has been significant research focus on fundamental strain engineering in TMDs, further research is still needed to realize the implications of TMD strain tunability. Computational studies have been quite robust: however, there is still a need to study new strain configurations and especially device heterostructures under strain. There is greatest room for improvements in experimental strain engineering, where most studies have found quite limited strain tunability before slippage or fracture occur. From both lenses, significant work is still required studying the applications of strain-related effects.

Using the computational results from this work's biaxial strain study, several interesting device structures are proposed. TMD heterostructures, whether in-plane or stacked, show promise for various semiconductor applications like transistors, sensors, and photo-detectors. Strain engineering adds another layer of tunability for these devices, allowing for either tunable flexible devices or for engineered band-alignments under specific levels of pre-strain as in strained-silicon. While the following analysis is specifically for biaxial strain, the same device heterostructures likely show similarly interesting strain-tunabilty under other types of mechanical strain, although with different rates and levels of tunability.

Table 6.1: Proposed TMD heterostructure pairings selected on the basis of large differences in strain tunability between corresponding band edges. Here, TMD 1 denotes the material with the larger absolute strain tunability in the specified regime, and the tunability difference is defined as $\Delta GF = GF_{\mathrm{TMD1}} - GF_{\mathrm{TMD2}}$ (meV/%). The estimated 3% modulation provides a simple comparison of relative band-edge shifts. For certain regimes, the quoted tunability applies only beyond the indicated strain threshold.

TMD 1	TMD 2	Regime	Carrier	ΔGF (meV/%)	Tunability at 3%	Valid For
WS_2	$MoSe_2$	Tensile	e^-	-26.5	-79.5	$\varepsilon \geq 0\%$
WS_2	$MoSe_2$	Tensile	h^+	42.7	128.1	$\varepsilon \geq 3\%$
WS_2	WSe_2	Tensile	h^+	44.7	134.1	$\varepsilon \geq 3\%$
WS_2	$MoSe_2$	Compressive	e^-	13.9	41.7	$\varepsilon \leq -1\%$

Promising device heterostructures are presented in Table 6.1, on the basis of large differences in strain tunability between materials using the results from the biaxial strain band-edge evolution in Fig. 3.13 computed with DFT. Heterostructure devices may either operate using holes or electrons as primary carriers: strain modulates conduction and valence bands differently, so the optimal material-pairings depend on the exact carrier and strain regimes. Heterostructures may also be created by either stacking materials to create a van der Waals (vdW) heterostructure, or alternatively grown coherently with connected lattices to create an in-plane heterostructure. This is more difficult considering the lattice mismatch between TMD materials, but several authors such as Xie et al. have demonstrated successful methods of growing complex structures and super-lattices using CVD growth [80]. One note is that several of the gauge factor differences only apply above or below certain strain thresholds and not necessarily for small strains: this results due to the varying band-edge evolutions under strain where trends are not necessarily symmetric about zero strain. As such, the "Tunability at 3%" indicates an additional 3% beyond the threshold minimum, not necessarily a 3% nominal strain.

Based on these results, the WS_2 and $MoSe_2$ heterostructure pairing displays quite promising strain tunability characteristics. Starting from zero-strain, the largest difference in gauge factors in Table 6.1 is between the CBM of WS_2 and $MoSe_2$ under tensile strain. The band-edges have a difference of $-26.5\text{meV}/\%$ in strain tunability, allowing the CBM to be shifted relative to one-another under small levels.

Because isolated monolayer calculations do not share a common reference energy, band-edge offsets are evaluated relative to the vacuum level rather than the Fermi level. While the Fermi levels of the two materials would align after heterostructure formation, such alignment is a consequence of interfacial charge redistribution and is not captured by separate monolayer calculations. Using this work's DFT calculations, the vacuum-aligned CBM of WS_2 and $MoSe_2$ are predicted to be within 0.293meV of one another, demonstrating essentially a flat-band condition. However, the exact band-alignment of this material pairing is disputed, with varying computational and experimental works predicting differing alignments [81–85]. For example, Sheng et al. predict a 418meV difference in CBM with WS_2 higher in energy [82], while another theoretical work predicts a 60meV offset with opposite alignment [81]. Depending on the precise equilibrium band alignment, if WS_2's CBM is higher in energy at zero-strain, it is plausible that this heterostructure's barrier will invert between the two materials once strained, due to the difference in strain tunability. This aligns with the results observed in a previous work using electric-fields rather than strain [84], although both methods typically tune band structures similarly. In the opposite scenario, if WS_2's CBM is lower in energy, the carrier dynamics will remain similar under strain, with the relative

energy difference between CBM increasing. Regardless, it is clear that the conduction band alignment between this pairing and the charge dynamics are highly-tunable under biaxial strain. For the same material pairing in the compressive regime, the conduction band trend is essentially the same albeit with much lesser magnitude. Under tensile strain, the pairing also displays promising strain tunability in the valence-bands for holes, although requiring larger strains to shift the relative band alignment. Given that there is a 368.4meV difference in vacuum-aligned VBM such that WS_2's VBM is more negative in energy, under large tensile strains the VBM band-edges may move closer together, although inversion is unlikely.

For a hole-carrier device, WS_2 and WSe_2 is another promising heterostructure candidate: however, the difference in gauge-factors requires at-least 3% biaxial strain to significantly move the band-edges from one another, which could prove difficult to achieve this large band-alignment tunability. More complex heterostructures are also possible by incorporating $MoTe_2$, although these are outside the scope of this study.

Based on the experimental lattice parameters given in Table 3.1, WS_2 and WSe_2 have an experimental lattice mismatch of 0.13Å or 4.13% compared to WS_2. Despite the mismatch, experimentalists have realized both van der Waals and in-plane heterostructure configurations for this material pairing [80, 86]. TMDs with the same chalcogen have very similar lattice parameters, irrespective of transition metal, while TMDs with different chalcogens have larger differences in lattice parameters. In comparison, WS_2 and $MoSe_2$ have an experimental lattice mismatch of 0.14Å or 4.44% compared to WS_2. In both in-plane heterostructure configurations, the mismatches are quite small, and given that the TMDs have the same crystal structure, either vdW or in-plane heterostructures are plausible and have been experimentally demonstrated [1, 81–83, 87–89].

Chapter 7

Conclusion

In summary, this work provides an overview of strain engineering in TMD monolayers using both first-principles and experimental methods. Computationally, VASP is utilized to study biaxial strain-induced electronic structure modulation across TMDs. Experimentally, uniaxial tensile strain is applied to WS_2 using both bending and elongation methods to modulate its optical properties, probed using photoluminescence spectroscopy.

This report provides a thorough analysis of monolayer group-VI transition metal dichalcogenides under biaxial strain, using various DFT methods in VASP for MoS_2, $MoSe_2$, $MoTe_2$, WS_2, and WSe_2. Biaxial strain allows for significant band structure modulation with monotonic and primarily linear bandgap tunability across strain levels, simultaneously preserving the lattice symmetry and Brillouin zone. Biaxial tensile strains offer greatest electronic bandgap tunability, while compressive strains offer a much narrower range of modulation. Electronic tunability is greatest in the sulfide-based TMDs, followed by the selenides and tellurides. TMDs with tungsten also tend to have slightly higher strain tunability compared to their molybdenum-based counterparts. As such, WS_2 has the highest strain tunability of the materials studied. For each TMD analyzed, there exists a window of direct bandgap behavior within roughly $-2\% \rightarrow 2\%$ biaxial strain, with the largest direct primary bandgap occurring under slight compressive strain at the K-point. Outside of this strain range, group-VI TMDs exhibit an indirect bandgap, narrowing more significantly with tensile strain compared with compressive strain. In regimes of indirect primary bandgap, the minimum direct bandgaps tend to have a slower rate of strain tunability – this implies that there is a significant difference in optical and electronic strain tunability. $MoTe_2$ exhibits slightly different properties compared to the other TMD materials, experiencing a metallic transition at -10% compressive strain and larger modulation with compressive strains rather than tensile strains. With the PBE method, MoS_2 and WS_2 are observed to undergo a metallic transition at 10% tensile strain. While large strain magnitudes provide

insight into trends, they may exceed experimentally accessible values due to the likely onset of slippage and fracture at far lower strain magnitudes. Finally, this work demonstrates that a majority of strain-induced bandgap tunability results from modulation of the conduction band minima (CBM), while the valence band maxima have far less strain tunability. Under tensile (compressive) strains, the CBM (VBM) tends to fall on the K-point, deviating in the opposite strain-regime.

This work's results display how PBE band structures are qualitatively correct, and by adding spin-orbit coupling, the general band-splitting behavior is obtained. However, the magnitudes of bandgaps are highly inaccurate with both the PBE and PBE+SOC methods. By switching to the HSE06 exchange-correlation functional with SOC, the overall band structures and trends remain largely similar. Still, the HSE06 functional significantly improves the bandgap magnitudes, underestimating experimental results by about 15%. HSE06+SOC bandgaps can potentially align more closely with experimental results by applying slight compressive strains, allowing for structures more closely matching physically observed TMDs.

While experimental biaxial strain engineering is outside the scope of this work due to the complex apparatuses required, uniaxial strain engineering exhibits fundamentally similar trends, albeit with smaller tunability and gauge factors. This work observes that transferring WS_2 from its growth Si substrate to a destination polymer substrate results in a PL blue-shift of about 60meV, likely a consequence of strain-relaxation in the TMD flakes. Applying uniaxial tensile strain to monolayer WS_2 on a PDMS substrate achieves a maximum A-exciton peak modulation of -36.48meV with a nominal gauge factor of just -1.25meV/%. While the strain transfer efficiency of PDMS is very limited, more promising results are attained through bending experiments. Bending a monolayer WS_2 sample on a PET substrate yields a maximum A-exciton peak modulation of -48.3meV. Another bending experiment of WS_2 on a PC-coated PET substrate yields an estimated gauge factor of -19.62meV/%, demonstrating the viability of the bending method for substrates more rigid than PDMS. Even at modest strain levels, strain-relaxation is observed in some of the TMD flakes measured. While significant improvements must be made to the experimental strain procedures, this work yields very promising strain tunability in WS_2, exceeding the strain-induced modulation of many past experimental works. A promising device heterostructure between WS_2 and $MoSe_2$ is finally proposed, owing to the large difference in strain tunability between these materials and the favorable, highly tunable band-alignment.

Fundamentally, understanding connections between strain and electronic-bandgaps in monolayer TMDs will accelerate developments in flexible electronics, photonics, and novel sensing applications. TMD materials with high strain sensitivity enable ultra-sensitive

strain sensors, potentially outperforming and offering novel device characteristics compared to traditional metal-foil strain gauges. Strain-tunable bandgaps can create reconfigurable photonic components such as LEDs or detectors with mechanically adjustable emission and absorption characteristics. Understanding direct-to-indirect bandgap transitions under strain could enable strain-tunable opto-electronics, for instance, a monolayer LED or laser whose emission wavelength or intensity can be modulated mechanically. Such tunability is attractive for developing mechanically tunable optical sensors and flexible photonic chips. These insights are also valuable for designing heterostructures and more complex devices with materials of differing strain tunability, potentially allowing invertible and reconfigurable band structure configurations depending on strain magnitude, type, and direction. Insights of strain modulation are also relevant to semiconductor reliability and epitaxial growth, allowing for better understanding of how intrinsic thermal and manufacturing-induced strain may impact semiconductor device performance. This is crucial as TMD device fabrication begins to move to the wafer scale.

Appendix A

Engineering and Industrial Standards

This work follows standard practices in computational materials science and electronic structure theory. While VASP pseudo-potentials are not permitted to be shared online due to licensing agreements, example input files and workflows are provided for reproducibility. A majority of figures, when possible, have been created using vector graphics with embedded text for optimal viewing on the digital version of this thesis. All simulations, data processing, and visualizations were performed using the following software tools and conventions:

Electronic Structure Calculations

- **Materials Project Database (v2025.09.25)**: Retrieval of crystal structures and lattice parameters
- **VASP (v6.4.3)**: Density Functional Theory (DFT) calculations using plane-wave basis sets and projector augmented-wave (PAW) potentials
- **VASPKIT (v1.5.0)**: Preparation of input files and post-processing of electronic structure data

Data Analysis

- **Python (3.9.12)**: Scientific computing environment used for all data analysis and automation
  - **NumPy, SciPy**: Numerical computation and linear algebra
  - **matplotlib**: Data visualization and plotting
  - **pymatgen, ASE**: Atomistic structure manipulations and analysis of VASP simulations

  - **sumo**: Electronic band-structure and density of states visualizations

Visualization and Post-Processing

- **VESTA**: Crystal structure visualization, modification, and structural analysis
- **Adobe Illustrator (2026)**: Preparation of publication-quality vector graphics, diagrams, and figures
- **LaTeX**: Typesetting and scientific documentation

High-Performance Computing

- **Slurm**: Job scheduling and resource management on Princeton's high-performance computing clusters

Units and Conventions

- All quantities and equations are reported in the **International System of Units (SI)** unless otherwise specified

Appendix B

Density Functional Theory

This appendix provides supplemental background on density functional theory (DFT), supplemental DFT data, and example VASP input code.

B.1 Theoretical Foundation

Density functional theory (DFT) is the leading method to efficiently and accurately model the ground-state properties of condensed matter and molecular systems [90]. Instead of finding ground-state wavefunctions which scale with $\approx 3N$ (where N is the number of electrons), DFT shifts the problem to finding the ground-state charge density $\rho(\mathbf{r})$ which is only a function of three variables (the real-space position). The main limitation of DFT is that the universal density functional $E[\rho(\mathbf{r})]$ is not precisely known– rather, it is only proven to exist [90].

To begin, we must first consider the Born-Oppenheimer approximation: since each proton is roughly 1836× the mass of an electron, protons react to changes much slower than electrons. As such, we may treat the wavefunctions of atomic nuclei and electrons separately. In the time-independent, non-relativistic picture, this simplifies the Schrödinger equation to:

$$\left[\sum_{i=1}^{N}\left(-\frac{\hbar^2}{2m}\nabla_i^2 + V_{\text{ext}}(\mathbf{r}_i)\right) + \sum_{i<j}^{N}\frac{e^2}{4\pi\varepsilon_0|\mathbf{r}_i-\mathbf{r}_j|}\right]\Psi(\mathbf{r}_1,\mathbf{r}_2,\ldots,\mathbf{r}_N) = E\Psi(\mathbf{r}_1,\mathbf{r}_2,\ldots,\mathbf{r}_N) \tag{B.1}$$

$$V_{\text{ext}}(\mathbf{r}) = -\sum_{A=1}^{M}\frac{Z_A e^2}{4\pi\varepsilon_0\,|\mathbf{r}-\mathbf{R}_A|} \tag{B.2}$$

where N denotes the number of electrons and M the number of atoms. The vector $\mathbf{r}_i$ represents the position of the i-th electron, while $\mathbf{R}_A$ denotes the position of the A-th atomic nucleus. The function $\Psi(\mathbf{r}_1,\mathbf{r}_2,\ldots,\mathbf{r}_N)$ is the many-electron wavefunction, and E is the

corresponding electronic energy eigenvalue. The constant $\hbar$ is the reduced Planck constant, m is the electron mass, and ∇_i^2 is the Laplacian operator acting on the coordinates of electron i. The quantity $V_{\text{ext}}(\mathbf{r}_i)$ denotes the external potential experienced by electron i due to all nuclei. Furthermore, e is the elementary charge and ε_0 is the vacuum permittivity. The parameter Z_A represents the atomic number (nuclear charge) of nucleus A. The term $-\frac{\hbar^2}{2m}\nabla_i^2$ represents the kinetic energy of the i-th electron. The term $\frac{e^2}{4\pi\varepsilon_0|\mathbf{r}_i-\mathbf{r}_j|}$ describes the Coulomb repulsion between electrons i and j, while $\frac{Z_A e^2}{4\pi\varepsilon_0|\mathbf{r}-\mathbf{R}_A|}$ corresponds to the Coulomb attraction between an electron at position $\mathbf{r}$ and nucleus A.

The dimensionality of this problem is far too complex to solve numerically for any reasonably sized systems. Thus, we may look at this problem through the Kohn-Sham lens, reformulating the problem from using the many-electron wavefunction to using the much simpler electron density $\rho(\mathbf{r})$. Explicitly,

$$\rho(\mathbf{r}) = N \int |\Psi(\mathbf{r}, \mathbf{r}_2, \ldots, \mathbf{r}_N)|^2 d\mathbf{r}_2 \cdots d\mathbf{r}_N, \tag{B.3}$$

which only depends on the three cartesian coordinates of the position vector $\mathbf{r}$.

There are two main DFT theorems we must next consider, known as the Hohenberg-Kohn theorems [91]. The first theorem claims that the ground-state electron density $\rho(\mathbf{r})$ uniquely determines the external potential $V_{\text{ext}}(\mathbf{r})$, up to an additive constant. Since $V_{\text{ext}}(\mathbf{r})$ uniquely determines the Hamiltonian, this establishes a one-to-one mapping between the ground-state wavefunction and the electron density.

This results since the kinetic energy and electron repulsion operators are system-independent, unlike the external potential $V_{\text{ext}}(\mathbf{r})$ which encodes all system-specific information (atomic positions and charges). Consequently, $V_{\text{ext}}(\mathbf{r})$ fixes the Hamiltonian (up to an additive constant), and therefore the ground-state wavefunction and all observables like ground-state energy are uniquely determined by the electron density. The ground-state energy of a system may then be separated as:

$$E_0 = E[\rho(\mathbf{r})] = F_{\text{HK}}[\rho(\mathbf{r})] + V[\rho(\mathbf{r})] \tag{B.4}$$

$$V[\rho(\mathbf{r})] = \int V_{\text{ext}}(\mathbf{r})\rho(\mathbf{r}) d\mathbf{r} \tag{B.5}$$

where the functional $F_{\text{HK}}[\rho(\mathbf{r})]$ is introduced as the sum of kinetic and electron repulsion energies. This functional is universal, since any system-specific dependencies are captured by the external potential.

The second Hohenberg-Kohn theorem is effectively a statement of the variational principle, claiming that the energy functional $E[\rho(\mathbf{r})]$ yields the lowest energy if and only if the

input electron density is the true ground state density $\rho_0(\mathbf{r})$ [91]. Formally speaking,

$$E_0 \leq E[\rho(\mathbf{r})] \tag{B.6}$$

with equality if and only if $\rho(\mathbf{r}) = \rho_0(\mathbf{r})$. In other words, the electron density $\rho(\mathbf{r})$ that minimizes the energy E is the true electron density, such that $E[\rho(\mathbf{r})] > E[\rho_0(\mathbf{r})] = E_0$ for all $\rho(\mathbf{r}) \neq \rho_0(\mathbf{r})$. Thus, determining the ground-state of a system within density functional theory reduces to finding the density $\rho(\mathbf{r})$ that minimizes the specified energy functional.

While the Hohenberg–Kohn theorems establish that the ground-state energy is a functional of the electron density and that it may be obtained variationally, there is no explicit form for the universal functional $F_{\mathrm{HK}}[\rho(\mathbf{r})]$. To address this predicament, Kohn and Sham introduced an auxiliary system of non-interacting electrons that reproduces the same ground-state electron density $\rho_0(\mathbf{r})$ as the true interacting system when under a fictitious local potential $V_{\mathrm{KS}}(\mathbf{r})$ [92]. Under this framework, the Hohenberg-Kohn functional may be split into three terms, as follows:

$$F_{\mathrm{HK}}[\rho(\mathbf{r})] = T_{\mathrm{s}}[\rho(\mathbf{r})] + E_{\mathrm{H}}[\rho(\mathbf{r})] + E_{\mathrm{xc}}[\rho(\mathbf{r})] \tag{B.7}$$

$$E_{\mathrm{H}}[\rho(\mathbf{r})] = \frac{1}{2}\frac{e^2}{4\pi\varepsilon_0}\iint \frac{\rho(\mathbf{r})\rho(\mathbf{r}')}{|\mathbf{r}-\mathbf{r}'|}d\mathbf{r}d\mathbf{r}' \tag{B.8}$$

where the first two terms are known explicitly and all unknown leftovers are pushed into the exchange-correlation functional E_{xc}. The T_{s} functional captures the kinetic energy of the non-interacting Kohn-Sham particles, while the Hartree energy functional captures the classical electrostatic energy according to the given charge density. Note that this Hartree term replaces the many-body electron interaction term, now considering the average (mean-field) effect at a given position. This leaves the exchange-correlation functional to recover the exact energy by re-introducing missing parts of the kinetic energy for interacting electrons not captured by the Kohn-Sham particles, in addition to the electron-electron interactions not captured by the Hartree term. In essence, the exchange-correlation functional must capture all many-body effects. This term must be approximated, but importantly, it is typically smaller in magnitude compared to the other terms [90]. One drawback of this method is that the kinetic energy is an implicit functional of density and an explicit functional of the Kohn-Sham orbitals, meaning that these orbitals must be solved for to compute this term. Formally,

$$T_{\mathrm{s}}[\rho(\mathbf{r})] = -\frac{\hbar^2}{2m}\sum_i \int \varphi_i^*(\mathbf{r})\nabla^2\varphi_i(\mathbf{r})d\mathbf{r} \tag{B.9}$$

where $\varphi_i(\mathbf{r})$ have been introduced as the Kohn-Sham orbitals. Within this formulation,

minimizing the energy $E[\rho(\mathbf{r})]$ corresponds directly to solving the Kohn-Sham equations, given by:

$$\left[-\frac{\hbar^2}{2m}\nabla^2 + V_{\text{ext}}(\mathbf{r}) + V_{\text{H}}(\mathbf{r}) + V_{\text{xc}}(\mathbf{r})\right]\varphi_i(\mathbf{r}) = \varepsilon_i\varphi_i(\mathbf{r}) \tag{B.10}$$

where $V_{\text{H}}(\mathbf{r})$ and $V_{\text{xc}}(\mathbf{r})$ are the functional derivatives with respect to $\rho(\mathbf{r})$ of E_{H} and E_{xc}, and φ_n and ε_n are the n-th Kohn-Sham orbital and eigenvalue. This formalism then defines the electron density as:

$$\rho(\mathbf{r}) \equiv \sum_{i}^{\text{occupied}} |\varphi_i(\mathbf{r})|^2, \tag{B.11}$$

where $\varphi_i(\mathbf{r})$ denotes the i-th occupied single-electron orbital. The summation runs over all occupied orbitals, and each orbital is assumed to be normalized: under this construction, $\int \rho(\mathbf{r})d\mathbf{r} = N$. It is necessary for the solution of these equations to be self-consistent, since both the Hartree and exchange-correlation potentials depend on the electron density. Thus, the interacting many-electron problem has successfully been mapped onto an effective non-interacting system, with all many-body effects contained in an approximated exchange–correlation functional. Solving the Kohn-Sham equations effectively distills down to solving the one-particle Schrodinger equation. This reformulation reduces the complexity of the problem from an exponentially scaling many-body wavefunction to an effective single-particle problem that scales more favorably with system size, enabling calculations for systems containing hundreds or thousands of atoms. The entire DFT procedure is as follows:

1. Define an initial guess for the charge density $\rho(\mathbf{r})$
2. Using $\rho_{\text{guess}}(\mathbf{r})$, we may directly compute $V_{\text{H}}(\mathbf{r}) = \frac{e^2}{4\pi\varepsilon_0}\int \frac{\rho(\mathbf{r}')}{|\mathbf{r}-\mathbf{r}'|}d\mathbf{r}'$ and $V_{\text{xc}} = \frac{\delta E_{\text{xc}}[\rho(\mathbf{r})]}{\delta\rho(\mathbf{r})}$. This then allows us to solve the Kohn-Sham equation for the single-particle wavefunctions $\varphi_i(\mathbf{r})$ given by Equation B.10.
3. Next, we can compute the actual charge density according to Equation B.11.
4. If the calculated charge density does not match the guess, $\rho_{\text{guess}}(\mathbf{r})$, i.e. $\rho_{\text{guess}}(\mathbf{r}) \neq \rho(\mathbf{r})$, repeat Step 1 with an updated guess until the density is self-consistent. This process is equivalent to minimizing the overall energy functional.

Once this process is completed, the overall ground-state energy may be computed from the converged electron density in combination with the exchange-correlation functional, Equation B.5 for the energy due to the electron-nuclear interactions, and Equation B.8 for the classical electrostatic energy. The kinetic energy functional given in Equation B.9 uses the single-particle Kohn-Sham orbitals, finally completing the overall energy. In practice, a numerical tolerance will be set while converging the self-consistent field (SCF) such that the

energy is minimized within the specified tolerance (such as $\delta = 10^{-6}$eV). It is important to note that the Kohn–Sham orbitals $\varphi_i(\mathbf{r})$ are auxiliary quantities introduced to reproduce the correct ground-state density. While they do not, in general, correspond directly to physical many-body states, they often provide useful qualitative insight into the electronic structure.

It is also important to note that approximation is introduced through the exchange-correlation functional: if this functional were known precisely, the ground-state energy and charge density would be exact [90]. There have been continuous efforts to develop increasingly accurate exchange-correlation functionals, yet one of the most widely used approaches is known as the Generalized-Gradient Approximation (GGA). Here, the exchange-correlation functional depends both on the electron density $\rho(\mathbf{r})$ and its gradient $\nabla\rho(\mathbf{r})$. The most popular functional within this category is the method of Perdew-Burke-Ernzerhof (PBE) [93]. So-called hybrid functionals incorporate a fraction of the exact electron exchange-energy computed using the Hartree-Fock method, allowing for more accurate predictions. The overall accuracy of a DFT calculation is therefore determined primarily by the quality of the exchange-correlation functional and how well it approximates the missing terms.

One of the major limitations of DFT is that it is fundamentally a ground-state method. As a consequence, it is not strictly suitable for excited-state phenomena or spectroscopy results, and it often fails for strongly correlated systems. Another fundamental limitation is that the accuracy of physical observables is often highly dependent on the exact exchange-correlation functional used. More accurate functionals will more accurately predict quantities like bandgaps, at the expense of much greater computational complexity.

Other practical considerations implemented in DFT codes include: minimization algorithms, basis sets used for Kohn-Sham orbitals, all-electron vs. pseudo-potential considerations of core electrons, and other numerical methods [90]. Further information about DFT can be found in [90, 94–96], among other resources.

B.2 Supplemental DFT Data

B.2.1 PBE Band Structures Across Materials

This section provides supplemental data on the band-structures for the five materials studied using the PBE exchange-correlation functional. Table B.1 presents the bandgap magnitude and type across the five materials and twenty-one strain levels. This demonstrates that most materials have a direct bandgap at the center of the strain range, for between three and five strain levels. This also depicts how $MoTe_2$ has slightly different behavior than the other materials, with a direct bandgap for a larger range of strains. It undergoes a

metallic transition for compressive strains (also trending toward a metallic transition for tensile strains), compared to a metallic transition simply at tensile strains for the other materials.

Strain (%)	MoS_2	$MoSe_2$	$MoTe_2$	WS_2	WSe_2
-10	1.245	0.587	0.000	1.320	0.804
-9	1.342	0.794	0.178	1.400	1.028
-8	1.423	0.996	0.355	1.480	1.193
-7	1.502	1.184	0.527	1.556	1.258
-6	1.577	1.250	0.693	1.630	1.323
-5	1.652	1.316	0.854	1.702	1.386
-4	1.723	1.381	1.007	1.772	1.446
-3	1.790	1.442	1.104	1.838	1.506
-2	1.908	1.501	1.252	1.906	1.565
-1	1.786	1.553	1.164	1.960	1.675
0	1.671	1.452	1.080	1.820	1.547
1	1.411	1.357	1.002	1.690	1.428
2	1.193	1.268	0.930	1.366	1.320
3	0.988	1.187	0.864	1.141	1.222
4	0.797	0.930	0.805	0.933	1.013
5	0.620	0.765	0.752	0.742	0.839
6	0.457	0.613	0.563	0.568	0.680
7	0.308	0.473	0.437	0.409	0.535
8	0.171	0.343	0.320	0.267	0.405
9	0.044	0.226	0.213	0.140	0.289
10	0.000	0.119	0.117	0.000	0.186

Table B.1: DFT-calculated primary bandgap (eV) vs. strain for monolayer TMDs, computed using the PBE exchange-correlation functional. Direct primary gaps are shown in blue.

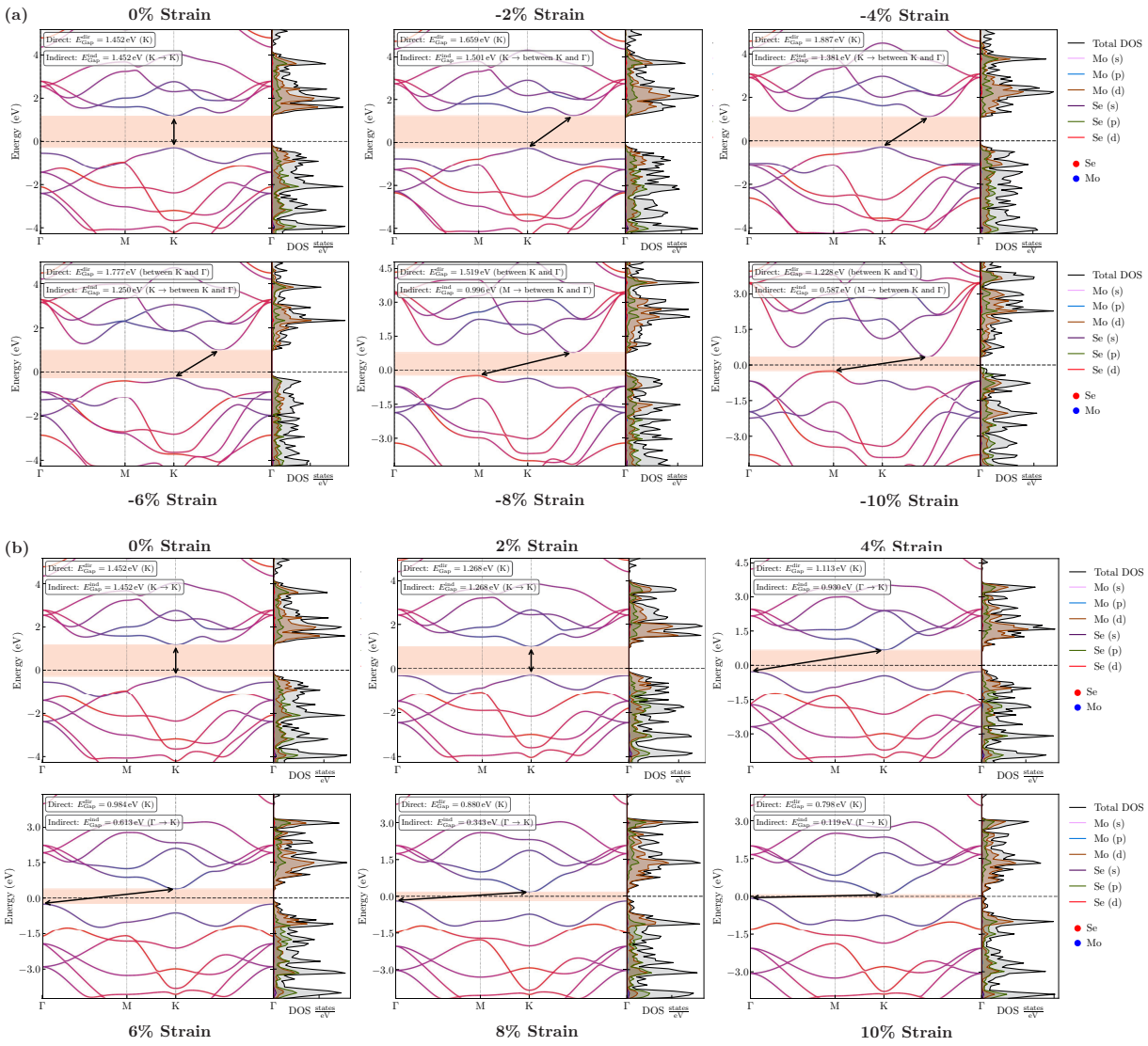

Figure B.1: Electronic band-structures and corresponding projected density-of-states of **$MoSe_2$** under biaxial (a) compressive and (b) tensile strains, computed using the **PBE exchange-correlation functional**. The band shading corresponds to the orbital contributions from the constituent elements. The Fermi level has been set to 0eV.

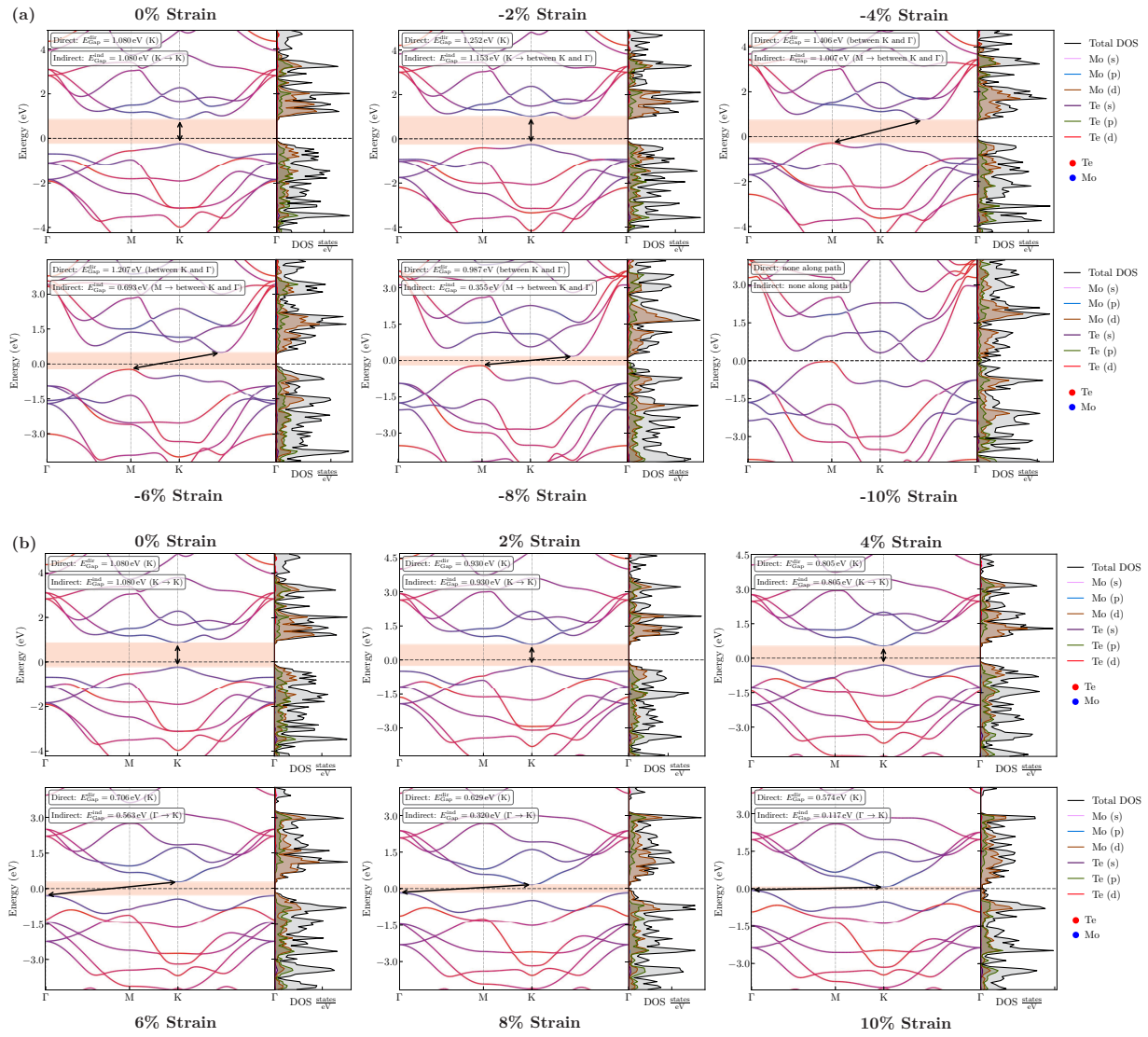

Figure B.2: Electronic band-structures and corresponding projected density-of-states of **$MoTe_2$** under biaxial (a) compressive and (b) tensile strains, computed using the **PBE exchange-correlation functional**. The band shading corresponds to the orbital contributions from the constituent elements. The Fermi level has been set to 0eV.

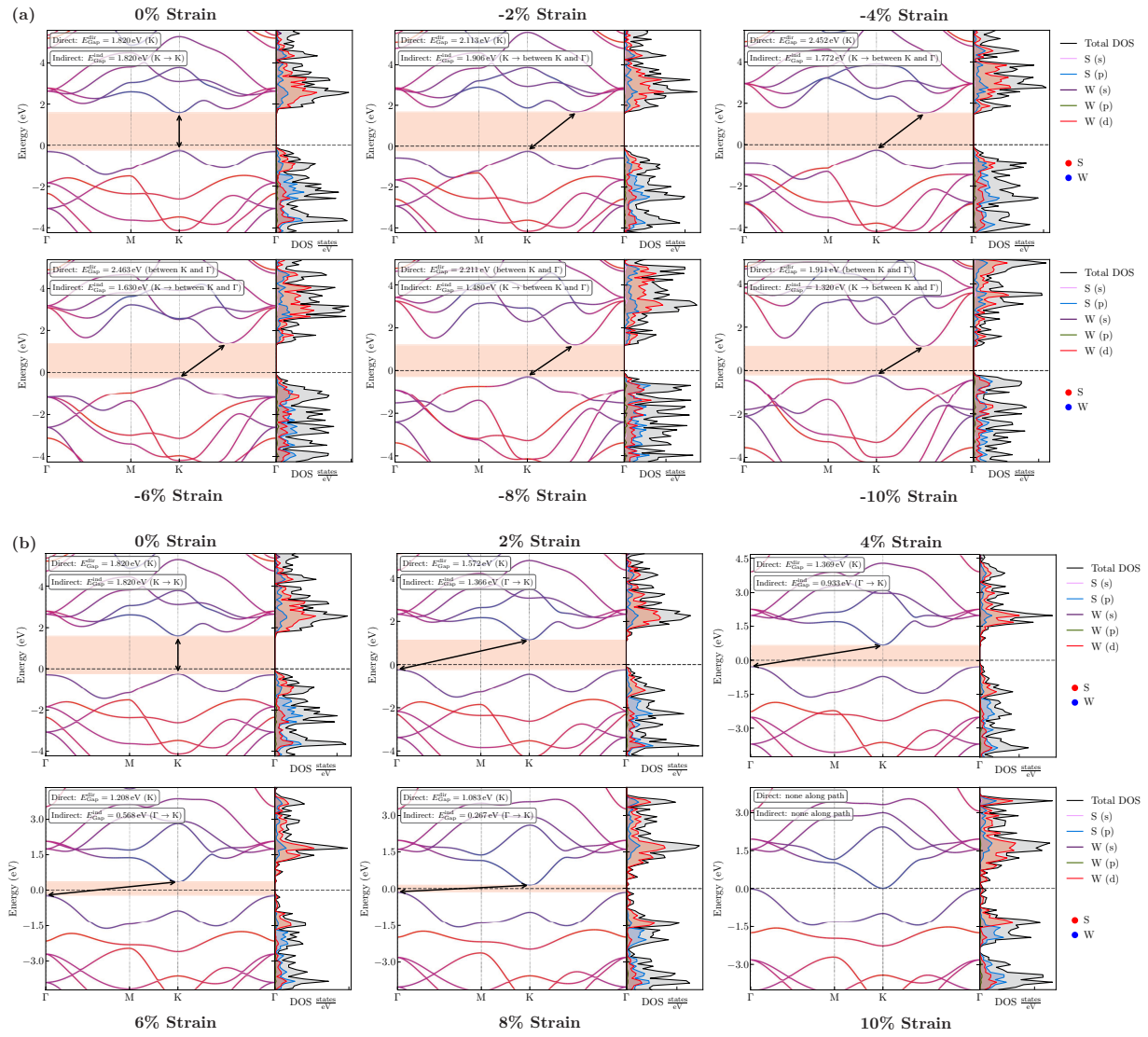

Figure B.3: Electronic band-structures and corresponding projected density-of-states of **WS_2** under biaxial (a) compressive and (b) tensile strains, computed using the **PBE exchange-correlation functional**. The band shading corresponds to the orbital contributions from the constituent elements. The Fermi level has been set to 0eV.

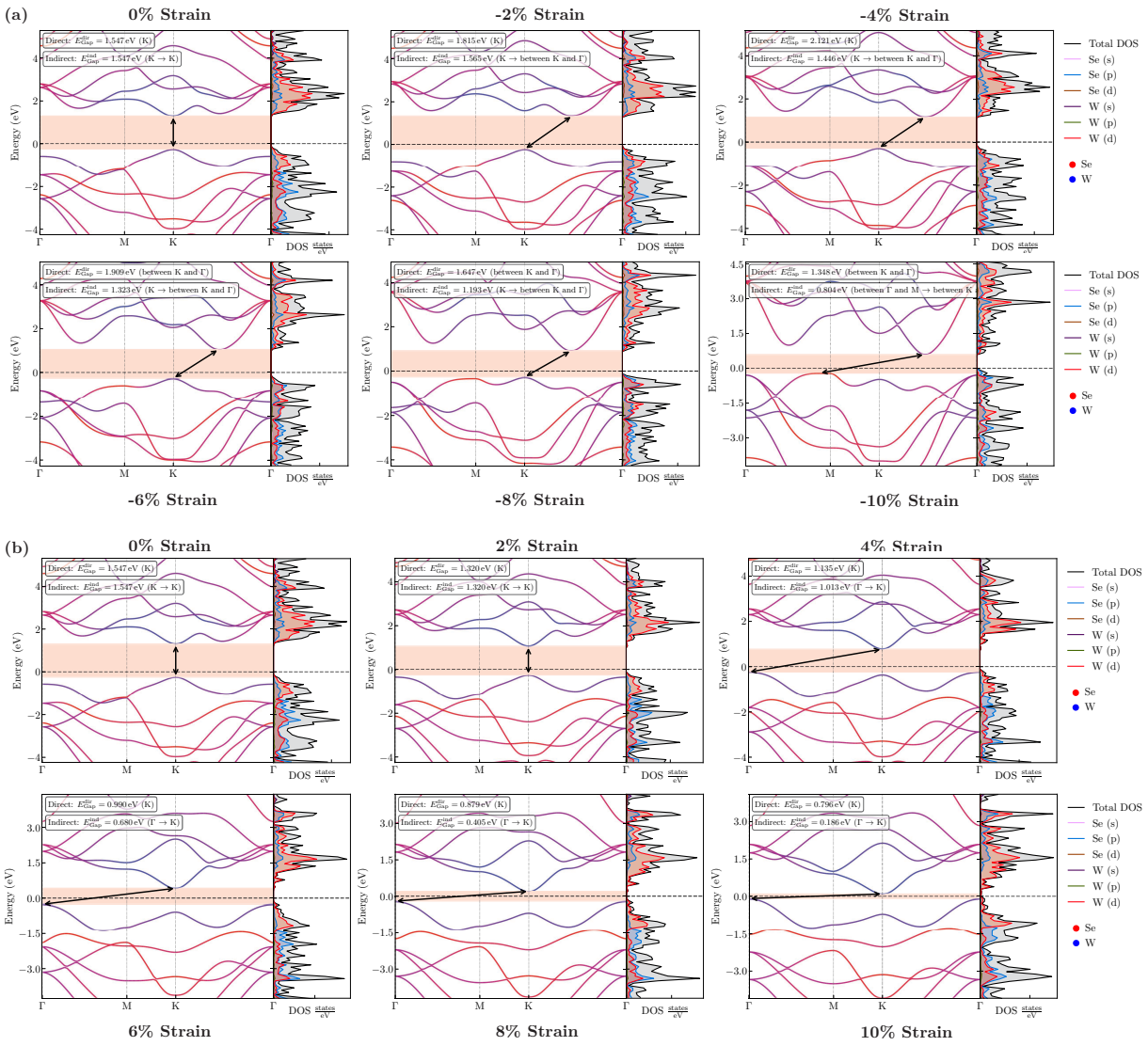

Figure B.4: Electronic band-structures and corresponding projected density-of-states of **WSe_2** under biaxial (a) compressive and (b) tensile strains, computed using the **PBE exchange-correlation functional**. The band shading corresponds to the orbital contributions from the constituent elements. The Fermi level has been set to 0eV.

B.2.2 MoS_2 Bandgaps vs. Strain Across DFT Methods

This section provides supplementary data on the primary bandgaps of MoS_2 under different strain levels, for the PBE, PBE+SOC, and HSE06+SOC methods. This data is presented in Table B.2.

Strain (%)	PBE	PBE+SOC	HSE06+SOC
-10	1.2449	1.2268	1.7718
-9	1.3416	1.3085	1.8593
-8	1.4227	1.3871	1.9430
-7	1.5022	1.4632	2.0233
-6	1.5767	1.5359	2.0999
-5	1.6519	1.6080	2.1762
-4	1.7233	1.6746	2.2456
-3	1.7897	1.7372	2.3130
-2	1.9077	1.8070	2.4289
-1	1.7857	1.6843	2.2834
0	1.6710	1.5703	2.1471
1	1.4113	1.4627	1.8936
2	1.1926	1.1801	1.6514
3	0.9876	0.9753	1.4238
4	0.7967	0.7843	1.2106
5	0.6201	0.6081	1.0119
6	0.4572	0.4445	0.8274
7	0.3076	0.2941	0.6545
8	0.1714	0.1567	0.4933
9	0.0445	0.0239	0.3376
10	0.0000	0.0000	0.1827

Table B.2: MoS_2 primary bandgap (eV) vs. strain using different DFT methods. Direct primary gaps are shown in blue.

B.3 Example INCAR Files

This section contains example INCAR files for various steps of the computational pipeline. The INCAR for the structural relaxation of the strained structures is as follows:

```
ISPIN  =  2            (Spin polarised DFT)
ISTART = 1

# ICHARG =  11         (Non-self-consistent: GGA/LDA band-structures)
LREAL  = .FALSE.       (Projection operators: automatic)
ENCUT  =  700        (Cut-off energy for plane wave basis set, in eV)
PREC   =  Accurate   (Precision level: Normal or Accurate)
LWAVE  = .FALSE.        (Write WAVECAR or not)
LCHARG = .FALSE.        (Write CHGCAR or not)
ADDGRID= .TRUE.        (Increase grid, helps GGA convergence)

Electronic Relaxation
ISMEAR =  0            (Gaussian smearing, metals:1)
SIGMA  =  0.05         (Smearing value in eV, metals:0.2)
NELM   =  90           (Max electronic SCF steps)
NELMIN =  6            (Min electronic SCF steps)
EDIFF  =  1E-06        (SCF energy convergence, in eV)

Ionic Relaxation
NSW    =  100          (Max ionic steps)
IBRION =  2            (Algorithm: 0-MD, 1-Quasi-New, 2-CG)
ISIF   =  2            (Stress/relaxation: 2-Ions, 3-Shape/Ions/V, 4-Shape/Ions)
EDIFFG = -1E-02      (Ionic convergence, eV/AA)
```

Next, the INCAR for the PBE band-structure calculations is as follows:

```
ISPIN  =  1            (Non-Spin polarised DFT)
ISTART = 1

LREAL  = .FALSE.       (Projection operators: automatic)
ENCUT  =  700        (Cut-off energy for plane wave basis set, in eV)
PREC   =  Accurate   (Precision level: Normal or Accurate)
LWAVE  = .TRUE.        (Write WAVECAR or not)
LCHARG = .TRUE.        (Write CHGCAR or not)
ADDGRID= .TRUE.        (Increase grid, helps GGA convergence)

Electronic Relaxation
ISMEAR =  0            (Gaussian smearing, metals:1)
SIGMA  =  0.05         (Smearing value in eV, metals:0.2)
NELM   =  90           (Max electronic SCF steps)
NELMIN =  6            (Min electronic SCF steps)
EDIFF  =  1E-06        (SCF energy convergence, in eV)

Ionic Relaxation
NSW    =  0          (Max ionic steps)
IBRION =  2            (Algorithm: 0-MD, 1-Quasi-New, 2-CG)
ISIF   =  2            (Stress/relaxation: 2-Ions, 3-Shape/Ions/V, 4-Shape/Ions)
EDIFFG = -1E-02      (Ionic convergence, eV/AA)

LORBIT = 11
NEDOS = 1000
```

Finally, an example INCAR for the HSE06+SOC calculations is as follows:

```
ISPIN  =  2            (Spin polarised DFT)
ISTART = 1
ICHARG = 1

# ICHARG =  11         (Non-self-consistent: GGA/LDA band-structures)
LREAL  = .FALSE.       (Projection operators: automatic)
ENCUT  =  700        (Cut-off energy for plane wave basis set, in eV)
PREC   =  Accurate   (Precision level: Normal or Accurate)
LWAVE  = .TRUE.        (Write WAVECAR or not)
LCHARG = .TRUE.        (Write CHGCAR or not)
ADDGRID= .TRUE.        (Increase grid, helps GGA convergence)

Electronic Relaxation
ISMEAR =  0            (Gaussian smearing, metals:1)
SIGMA  =  0.05         (Smearing value in eV, metals:0.2)
NELM   =  90           (Max electronic SCF steps)
NELMIN =  6            (Min electronic SCF steps)
EDIFF  =  1E-06        (SCF energy convergence, in eV)

Ionic Relaxation
NSW    =  0          (Max ionic steps)
IBRION =  2            (Algorithm: 0-MD, 1-Quasi-New, 2-CG)
ISIF   =  2            (Stress/relaxation: 2-Ions, 3-Shape/Ions/V, 4-Shape/Ions)
EDIFFG = -1E-02      (Ionic convergence, eV/AA)
ISYM =  0            (Symmetry: 0=none, 2=GGA, 3=hybrids)

LORBIT = 11
NEDOS = 1000

LSORBIT = .TRUE.       (Enable spin-orbit coupling)
LHFCALC= .TRUE.       (Activate HF)
AEXX   =  0.25        (25% HF exact exchange, set to reproduce exp. bandgap)
HFSCREEN= 0.2         (Switch to screened exchange, e.g. HSE06)
ALGO   =  ALL         (Electronic Minimisation Algorithm)
TIME   =  0.4         (Timestep for IALGO5X)
PRECFOCK= N           (HF FFT grid)
HFRCUT = -1
```

Appendix C

Supplemental Experimental Data

This section provides the raw experimental photoluminescence strain engineering data, using both the elongation and bending methods. PL peaks are reported, as well as the exciton and trion peaks based on fitting the sum of two Gaussians to the data. This method does not *always* work perfectly, so some of the exciton or trion peaks may be slightly flawed. The exciton peak generally coincides well with the overall PL peak, so it may be considered as the most robust datapoint per measurement.

C.1 Elongation Data

Data for the main and alternative elongation experiments are provided in Table C.1 and Table C.2, respectively. A plot visualizing spectra for the alternative elongation experiment is demonstrated in Fig. C.1, along with a plot of the exciton peak values according to strain and the estimated gauge factor.

C.2 Bending Data

Data for the main bending experiment is provided in Table C.3, along with the qualitative strain-levels (note that strain level 5 indicates the folded/creased scenario). Data for the alternative, quantitative bending experiment is provided in Table C.4; spectra and exciton peaks according to strain are plotted in Fig. C.2 for this experiment.

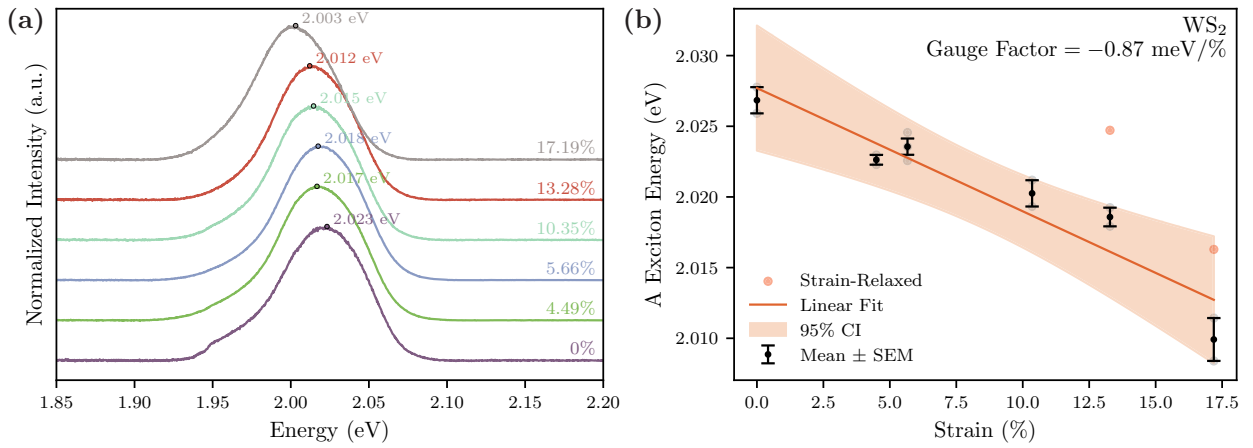

Figure C.1: Alternative elongation experiment for the strain-dependent PL response of monolayer WS_2 on a PDMS substrate encapsulated by PC under varying uniaxial tensile strains. **(a)** Stacked, normalized PL spectra at increasing strain, vertically offset for clarity. Peak energies are labeled, and the selected spectra correspond to measurements exhibiting the largest strain-induced redshift. **(b)** Extracted A-exciton energies as a function of strain. Light gray points show individual measurements, while black markers with error bars denote the mean energy at each strain with standard error of the mean (SEM). The orange line represents an unweighted linear fit to the averaged data, with the shaded region indicating the 95% confidence interval. Red points correspond to strain-relaxed flakes and are excluded from the fit.

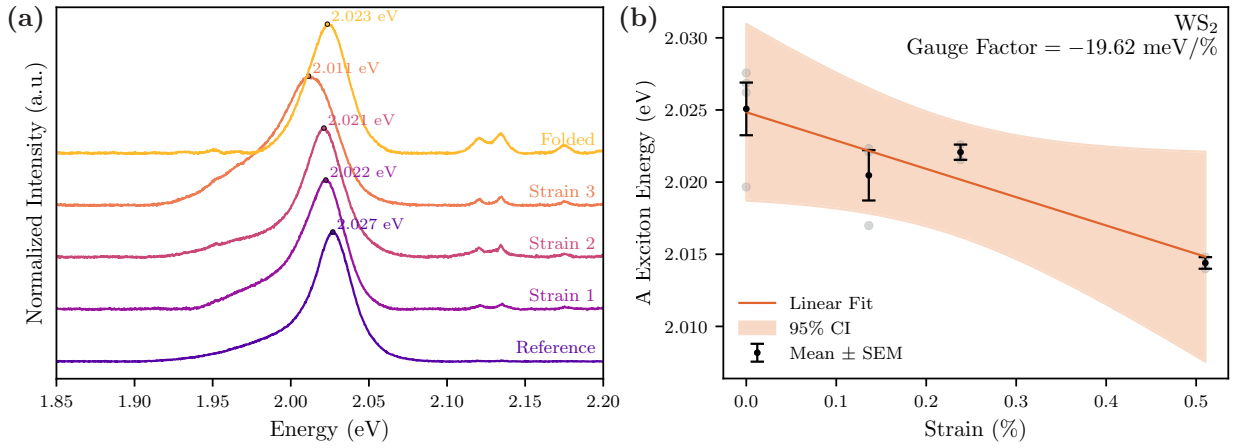

Figure C.2: Quantitative bending experiment for the strain-dependent PL response of monolayer WS_2 on a PET+PC substrate encapsulated by PC under varying uniaxial tensile strains. **(a)** Stacked, normalized PL spectra at increasing strain, vertically offset for clarity. Peak energies are labeled, and the selected spectra correspond to measurements exhibiting the largest strain-induced redshift. **(b)** Extracted A-exciton energies as a function of strain. Light gray points show individual measurements, while black markers with error bars denote the mean energy at each strain with standard error of the mean (SEM). The orange line represents an unweighted linear fit to the averaged data, with the shaded region indicating the 95% confidence interval.

Table C.1: Peak-fitted photoluminescence data for monolayer WS_2 on a PDMS substrate encapsulated by PC under uniaxial elongation, corresponding to the **main elongation experiment** (as depicted in Fig. 5.4). Each row represents the PL spectrum of a distinct, randomly selected flake.

Length (mm)	Strain (%)	PL Peak (eV)	A Exciton Peak (eV)	Trion Peak (eV)
Reference Measurement (Unmounted)				
–	–	2.0306	2.0310	2.0068
Mounted on Apparatus				
60.5	0.00	2.0261	2.0270	2.0095
60.5	0.00	2.0273	2.0275	2.0040
60.5	0.00	2.0271	2.0276	2.0040
63.1	4.30	2.0189	2.0191	1.9984
63.1	4.30	2.0286	2.0265	2.0044
63.1	4.30	2.0229	2.0229	2.0055
63.1	4.30	2.0248	2.0250	1.9975
67.5	11.57	2.0177	2.0176	1.9989
67.5	11.57	2.0110	2.0114	1.9920
67.5	11.57	2.0118	2.0136	1.9917
67.5	11.57	2.0110	2.0123	1.9911
67.5	11.57	2.0118	2.0126	1.9928
69.5	14.88	2.0049	2.0020	1.9698
69.5	14.88	2.0027	2.0034	1.9885
69.5	14.88	2.0157	2.0139	1.9747
69.5	14.88	2.0206	2.0201	2.0010
69.5	14.88	2.0211	2.0214	2.0019
69.5	14.88	2.0221	2.0221	1.9982
69.5	14.88	2.0049	2.0055	1.9842
69.5	14.88	2.0103	2.0123	1.9893
69.5	14.88	2.0066	2.0084	1.9890
69.5	14.88	2.0096	2.0108	1.9850
73.0	20.66	1.9952	1.9945	1.9876
73.0	20.66	2.0054	2.0015	1.9419
73.0	20.66	2.0023	2.0031	1.9811

Table C.2: Peak-fitted photoluminescence data for monolayer WS_2 on a PDMS substrate encapsulated by PC under uniaxial elongation, corresponding to the **alternate elongation experiment**. Each row represents the PL spectrum of a distinct, randomly selected flake.

Length (mm)	Strain (%)	PL Peak (eV)	A Exciton Peak (eV)	Trion Peak (eV)
Reference Measurement (Unmounted)				
–	–	2.0155	2.0192	1.9615
Mounted on Apparatus				
51.2	0.00	2.0212	2.0259	2.0027
51.2	0.00	2.0232	2.0278	1.9935
53.5	4.49	2.0168	2.0223	1.9895
53.5	4.49	2.0202	2.0230	1.9914
54.1	5.66	2.0195	2.0246	1.9973
54.1	5.66	2.0190	2.0235	1.9974
54.1	5.66	2.0200	2.0226	1.9933
56.5	10.35	2.0163	2.0212	1.9948
56.5	10.35	2.0146	2.0193	1.9918
58.0	13.28	2.0190	2.0247	1.9964
58.0	13.28	2.0141	2.0192	1.9932
58.0	13.28	2.0121	2.0179	1.9942
60.0	17.19	2.0129	2.0114	1.9644
60.0	17.19	2.0065	2.0163	1.9938
60.0	17.19	2.0031	2.0084	1.9864

Table C.3: Peak-fitted photoluminescence data for monolayer WS_2 on a PET substrate encapsulated by PC under uniaxial bending, corresponding to the **main bending experiment**. Each row represents the PL spectrum of a distinct, randomly selected flake, under under increasing strain conditions.

Scenario	PL Peak (eV)	A Exciton Peak (eV)	Trion Peak (eV)
Reference	2.0334	2.0349	1.9918
Reference	2.0359	2.0359	1.9904
Reference	2.0339	2.0360	1.9899
Strain 1	2.0314	2.0332	1.9797
Strain 1	2.0334	2.0349	1.9868
Strain 2	2.0012	2.0014	1.9517
Strain 2	2.0092	2.0123	1.9723
Strain 2	2.0402	2.0395	1.9988
Strain 2	2.0092	2.0088	1.9591
Strain 3	2.0141	2.0136	1.9601
Strain 3	2.0104	2.0130	1.9612
Strain 4	2.0014	1.9966	–
Strain 4	1.9921	1.9876	–
Strain 4	2.0124	2.0137	1.9709
Strain 5	2.0119	2.0174	1.9577
Strain 5	2.0151	2.0228	1.9786

Note: Missing peak values are indicated by "–", corresponding to spectra best fitted with a single Gaussian. Scenario labels correspond to measurements under qualitatively increasing strain conditions.

Table C.4: Peak-fitted photoluminescence data for monolayer WS_2 on a PET+PC substrate encapsulated by PC under uniaxial bending, corresponding to the **quantitative bending experiment**. Each row represents the PL spectrum of a distinct, randomly selected flake, under under increasing strain conditions (controlled by changing the radii of curvature).

Radius (mm)	Strain (%)	PL Peak (eV)	A Exciton Peak (eV)	Trion Peak (eV)
–	0	2.0264	2.0268	2.0061
–	0	2.0269	2.0276	2.0059
–	0	2.0202	2.0197	1.9833
–	0	2.0257	2.0262	1.9946
45.9	0.1362	2.0224	2.0223	1.9614
45.9	0.1362	2.0205	2.0170	1.9634
45.9	0.1362	2.0224	2.0221	1.9837
26.25	0.2381	2.0212	2.0215	1.9979
26.25	0.2381	2.0222	2.0226	1.9990
12.25	0.5102	2.0119	2.0148	1.9810
12.25	0.5102	2.0114	2.0140	1.9781
Folded	–	2.0234	2.0241	1.9945

Note: Strain values are estimated from the bending radius, assuming uniform curvature and negligible PC thickness. $t = 125\mu$m is used for the PET layer.

References

[1] Morasae Samadi et al. “Group 6 transition metal dichalcogenide nanomaterials: synthesis, applications and future perspectives”. In: *Nanoscale Horizons* 3.2 (Feb. 2018). Publisher: The Royal Society of Chemistry, pp. 90–204. ISSN: 2055-6764. DOI: 10.1039/C7NH00137A.

[2] Simone Bertolazzi, Jacopo Brivio, and Andras Kis. “Stretching and Breaking of Ultrathin MoS2”. In: *ACS Nano* 5.12 (Dec. 2011). Publisher: American Chemical Society, pp. 9703–9709. ISSN: 1936-0851. DOI: 10.1021/nn203879f.

[3] Rafael Roldán et al. “Strain engineering in semiconducting two-dimensional crystals”. In: *Journal of Physics: Condensed Matter* 27.31 (July 2015), p. 313201. ISSN: 1361-648X. DOI: 10.1088/0953-8984/27/31/313201.

[4] Álvaro Rodríguez et al. “Improved Strain Transfer Efficiency in Large-Area Two-Dimensional MoS2 Obtained by Gold-Assisted Exfoliation”. In: *The Journal of Physical Chemistry Letters* 15.24 (June 2024). Publisher: American Chemical Society, pp. 6355–6362. DOI: 10.1021/acs.jpclett.4c00855.

[5] Charalampos Androulidakis et al. “Graphene flakes under controlled biaxial deformation”. In: *Scientific Reports* 5.1 (Dec. 2015). Publisher: Nature Publishing Group, p. 18219. ISSN: 2045-2322. DOI: 10.1038/srep18219.

[6] Jerry A. Yang et al. “Biaxial Tensile Strain Enhances Electron Mobility of Monolayer Transition Metal Dichalcogenides”. In: *ACS Nano* 18.28 (July 2024). Publisher: American Chemical Society, pp. 18151–18159. ISSN: 1936-0851. DOI: 10.1021/acsnano.3c08996.

[7] Rui Yang et al. “Tuning Optical Signatures of Single- and Few-Layer MoS2 by Blown-Bubble Bulge Straining up to Fracture”. In: *Nano Letters* 17.8 (Aug. 2017). Publisher: American Chemical Society, pp. 4568–4575. ISSN: 1530-6984. DOI: 10.1021/acs.nanolett.7b00730.

[8] Eudomar Henríquez-Guerra et al. “Large Biaxial Compressive Strain Tuning of Neutral and Charged Excitons in Single-Layer Transition Metal Dichalcogenides”. In: *ACS Applied Materials & Interfaces* 15.49 (2023). PMID: 38033040, pp. 57369–57378. DOI: 10.1021/acsami.3c13281.

[9] Felix Carrascoso, Riccardo Frisenda, and Andres Castellanos-Gomez. “Biaxial versus uniaxial strain tuning of single-layer MoS2”. In: *Nano Materials Science*. Special issue on Graphene and 2D Alternative Materials 4.1 (Mar. 2022), pp. 44–51. ISSN: 2589-9651. DOI: 10.1016/j.nanoms.2021.03.001.

[10] Zhiwei Li et al. “Efficient strain modulation of 2D materials via polymer encapsulation”. In: *Nature Communications* 11.1 (Mar. 2020). Publisher: Nature Publishing Group, p. 1151. ISSN: 2041-1723. DOI: 10.1038/s41467-020-15023-3.

[11] Priya Johari and Vivek B. Shenoy. “Tuning the Electronic Properties of Semiconducting Transition Metal Dichalcogenides by Applying Mechanical Strains”. In: *ACS Nano* 6.6 (June 2012). Publisher: American Chemical Society, pp. 5449–5456. ISSN: 1936-0851. DOI: 10.1021/nn301320r.

[12] Zhiwei Peng et al. “Strain engineering of 2D semiconductors and graphene: from strain fields to band-structure tuning and photonic applications”. In: *Light: Science & Applications* 9.1 (Nov. 2020), p. 190. ISSN: 2047-7538. DOI: 10.1038/s41377-020-00421-5.

[13] Leah Isseroff Bendavid et al. “Strain-engineering in two-dimensional transition metal dichalcogenide alloys”. In: *Journal of Applied Physics* 132.22 (Dec. 2022), p. 225303. ISSN: 0021-8979. DOI: 10.1063/5.0120484.

[14] Gerd Plechinger et al. “Control of biaxial strain in single-layer molybdenite using local thermal expansion of the substrate”. en. In: *2D Materials* 2.1 (Mar. 2015), p. 015006. ISSN: 2053-1583. DOI: 10.1088/2053-1583/2/1/015006.

[15] G. Tsutsui et al. “Strain engineering in functional materials”. In: *AIP Advances* 9.3 (Mar. 2019), p. 030701. ISSN: 2158-3226. DOI: 10.1063/1.5075637.

[16] Kin Fai Mak et al. “Atomically Thin MoS_2: A New Direct-Gap Semiconductor”. In: *Phys. Rev. Lett.* 105 (13 2010), p. 136805. DOI: 10.1103/PhysRevLett.105.136805.

[17] Chia-Hui Lee et al. “Tungsten Ditelluride: a layered semimetal”. In: *Scientific Reports* 5.1 (June 2015). Publisher: Nature Publishing Group, p. 10013. ISSN: 2045-2322. DOI: 10.1038/srep10013.

[18] Georg Kresse and Jurgen Hafner. “Norm-conserving and ultrasoft pseudopotentials for first-row and transition elements”. In: *Journal of Physics: Condensed Matter* 6.40 (1994), p. 8245.

[19] Georg Kresse and Jürgen Furthmüller. “Efficiency of ab-initio total energy calculations for metals and semiconductors using a plane-wave basis set”. In: *Computational materials science* 6.1 (1996), pp. 15–50.

[20] Georg Kresse and Jürgen Furthmüller. “Efficient iterative schemes for ab initio total-energy calculations using a plane-wave basis set”. In: *Physical review B* 54.16 (1996), p. 11169.

[21] Georg Kresse and Daniel Joubert. “From ultrasoft pseudopotentials to the projector augmented-wave method”. In: *Physical review b* 59.3 (1999), p. 1758.

[22] Vei Wang et al. “VASPKIT: A user-friendly interface facilitating high-throughput computing and analysis using VASP code”. In: *Computer Physics Communications* 267 (2021), p. 108033. ISSN: 0010-4655. DOI: 10.1016/j.cpc.2021.108033.

[23] Vei Wang et al. “High-Throughput Computational Screening of Two-Dimensional Semiconductors”. In: *The Journal of Physical Chemistry Letters* 13.50 (2022). PMID: 36480578, pp. 11581–11594. DOI: 10.1021/acs.jpclett.2c02972.

[24] Dimitrios G Papageorgiou et al. “Mechanical properties of transition metal dichalcogenides: towards high-performance polymer nanocomposites”. In: *2D Materials* 12.1 (2024), p. 012002. DOI: 10.1088/2053-1583/ad9dfc.

[25] Riccardo Frisenda et al. “Biaxial strain tuning of the optical properties of single-layer transition metal dichalcogenides”. In: *npj 2D Materials and Applications* 1.1 (May 2017). Publisher: Nature Publishing Group, p. 10. ISSN: 2397-7132. DOI: 10.1038/s41699-017-0013-7.

[26] Zheng Liu et al. “Strain and structure heterogeneity in MoS2 atomic layers grown by chemical vapour deposition”. In: *Nature Communications* 5.1 (Nov. 2014). Publisher: Nature Publishing Group, p. 5246. ISSN: 2041-1723. DOI: 10.1038/ncomms6246.

[27] Felix Carrascoso et al. “Improved strain engineering of 2D materials by adamantane plasma polymer encapsulation”. In: *npj 2D Materials and Applications* 7.1 (Mar. 2023). Publisher: Nature Publishing Group, p. 24. ISSN: 2397-7132. DOI: 10.1038/s41699-023-00393-1.

[28] Hiram J. Conley et al. “Bandgap Engineering of Strained Monolayer and Bilayer MoS2”. In: *Nano Letters* 13.8 (2013). PMID: 23819588, pp. 3626–3630. DOI: 10.1021/nl4014748.

[29] Jason W. Christopher et al. “Monolayer MoS2 Strained to 1.3% With a Microelectromechanical System”. In: *Journal of Microelectromechanical Systems* 28.2 (Apr. 2019), pp. 254–263. ISSN: 1941-0158. DOI: 10.1109/JMEMS.2018.2877983.

[30] Felix Carrascoso et al. “Strain engineering in single-, bi- and tri-layer MoS2, MoSe2, WS2 and WSe2”. In: *Nano Research* 14.6 (June 2021), pp. 1698–1703. ISSN: 1998-0000. DOI: 10.1007/s12274-020-2918-2.

[31] Xin He et al. “Strain engineering in monolayer WS2, MoS2, and the WS2/MoS2 heterostructure”. In: *Applied Physics Letters* 109.17 (Oct. 2016), p. 173105. ISSN: 0003-6951. DOI: 10.1063/1.4966218.

[32] Iris Niehues et al. “Strain Control of Exciton–Phonon Coupling in Atomically Thin Semiconductors”. In: *Nano Letters* 18.3 (Mar. 2018). Publisher: American Chemical Society, pp. 1751–1757. ISSN: 1530-6984. DOI: 10.1021/acs.nanolett.7b04868.

[33] Keliang He et al. “Experimental Demonstration of Continuous Electronic Structure Tuning via Strain in Atomically Thin MoS2”. In: *Nano Letters* 13.6 (2013). PMID: 23675872, pp. 2931–2936. DOI: 10.1021/nl4013166.

[34] Ashby Phillip John, Arya Thenapparambil, and Madhu Thalakulam. “Strain-engineering the Schottky barrier and electrical transport on MoS2”. In: *Nanotechnology* 31.27 (Apr. 2020). Publisher: IOP Publishing, p. 275703. ISSN: 0957-4484. DOI: 10.1088/1361-6528/ab83b7.

[35] Joshua O. Island et al. “Precise and reversible band gap tuning in single-layer MoSe2 by uniaxial strain”. In: *Nanoscale* 8.5 (Jan. 2016). Publisher: The Royal Society of Chemistry, pp. 2589–2593. ISSN: 2040-3372. DOI: 10.1039/C5NR08219F.

[36] Lukas Mennel, Matthias Paur, and Thomas Mueller. “Second harmonic generation in strained transition metal dichalcogenide monolayers: MoS2, MoSe2, WS2, and WSe2”. In: *APL Photonics* 4.3 (Dec. 2018), p. 034404. ISSN: 2378-0967. DOI: 10.1063/1.5051965.

[37] Shou-Xin Zhao et al. “Strain-enhanced trion emission in monolayer WS2 modulated by an ion-gel electrochemical gate”. In: *Applied Physics Letters* 126.22 (June 2025), p. 221102. ISSN: 0003-6951. DOI: 10.1063/5.0269822.

[38] Martin E. P. Tweedie et al. “Inhomogeneous Strain Release during Bending of WS_2 on Flexible Substrates”. In: *ACS Applied Materials & Interfaces* 10.45 (Nov. 2018), pp. 39177–39186. ISSN: 1944-8244, 1944-8252. DOI: 10.1021/acsami.8b12707.

[39] Yanlong Wang et al. “Strain-induced direct–indirect bandgap transition and phonon modulation in monolayer WS2”. In: *Nano Research* 8.8 (Aug. 2015), pp. 2562–2572. ISSN: 1998-0000. DOI: 10.1007/s12274-015-0762-6.

[40] Jin-hui Chen et al. “Tunable and enhanced light emission in hybrid WS2-optical-fiber-nanowire structures”. In: *Light: Science & Applications* 8.1 (Jan. 2019). Publisher: Nature Publishing Group, p. 8. ISSN: 2047-7538. DOI: 10.1038/s41377-018-0115-9.

[41] Francesco Colangelo et al. “Local tuning of WS2 photoluminescence using polymeric micro-actuators in a monolithic van der Waals heterostructure”. In: *Applied Physics Letters* 115.18 (Oct. 2019), p. 183101. ISSN: 0003-6951. DOI: 10.1063/1.5122262.

[42] Fang Wang et al. “Strain engineering in monolayer WS2 and WS2 nanocomposites”. In: *2D Materials* 7.4 (Aug. 2020). Publisher: IOP Publishing, p. 045022. ISSN: 2053-1583. DOI: 10.1088/2053-1583/ababf1.

[43] Qianhui Zhang et al. “Strain Relaxation of Monolayer WS2 on Plastic Substrate”. In: *Advanced Functional Materials* 26.47 (2016), pp. 8707–8714. ISSN: 1616-3028. DOI: 10.1002/adfm.201603064.

[44] Robert Schmidt et al. “Reversible uniaxial strain tuning in atomically thin WSe2”. In: *2D Materials* 3.2 (June 2016). Publisher: IOP Publishing, p. 021011. ISSN: 2053-1583. DOI: 10.1088/2053-1583/3/2/021011.

[45] Wenshuai Hu et al. “Straining of atomically thin WSe2 crystals: Suppressing slippage by thermal annealing”. In: *Journal of Applied Physics* 132.8 (Aug. 2022), p. 085104. ISSN: 0021-8979. DOI: 10.1063/5.0096190.

[46] David Lloyd et al. “Band Gap Engineering with Ultralarge Biaxial Strains in Suspended Monolayer MoS_2”. en. In: *Nano Letters* 16.9 (Sept. 2016), pp. 5836–5841. ISSN: 1530-6984, 1530-6992. DOI: 10.1021/acs.nanolett.6b02615.

[47] Antonios Michail et al. “Biaxial strain engineering of CVD and exfoliated single- and bi-layer MoS2 crystals”. en. In: *2D Materials* 8.1 (Nov. 2020), p. 015023. ISSN: 2053-1583. DOI: 10.1088/2053-1583/abc2de.

[48] S. Patel et al. “Biaxial strain tuning of excitons in monolayer MoSe 2 by high-temperature physical vapor deposition”. en. In: *Physical Review B* 110.24 (Dec. 2024), p. 245310. ISSN: 2469-9950, 2469-9969. DOI: 10.1103/PhysRevB.110.245310.

[49] F. S. Covre et al. “Revealing the impact of strain in the optical properties of bubbles in monolayer MoSe2”. en. In: *Nanoscale* 14.15 (Apr. 2022), pp. 5758–5768. ISSN: 2040-3372. DOI: 10.1039/D2NR00315E.

[50] Ji Zhou et al. “Engineering Valley-Electronic Structures and Optical Properties of Monolayer WS_2 by Large Biaxial Strain”. en. In: *The Journal of Physical Chemistry C* 129.29 (July 2025), pp. 13322–13328. ISSN: 1932-7447, 1932-7455. DOI: 10.1021/acs.jpcc.5c03219.

[51] Shrawan Roy, Xiaodong Yang, and Jie Gao. “Biaxial strain tuned upconversion photoluminescence of monolayer WS2”. en. In: *Scientific Reports* 14.1 (Feb. 2024), p. 3860. ISSN: 2045-2322. DOI: 10.1038/s41598-024-54185-8.

[52] Antonios Michail et al. “Tuning the Photoluminescence and Raman Response of Single-Layer WS2 Crystals Using Biaxial Strain”. In: *The Journal of Physical Chemistry C* 127.7 (Feb. 2023), pp. 3506–3515. ISSN: 1932-7447. DOI: 10.1021/acs.jpcc.2c06933.

[53] G. Kourmoulakis et al. “Biaxial strain tuning of exciton energy and polarization in monolayer WS2”. In: *Applied Physics Letters* 123.22 (Nov. 2023), p. 223103. ISSN: 0003-6951. DOI: 10.1063/5.0167724.

[54] Burak Aslan et al. “Excitons in strained and suspended monolayer WSe2”. en. In: *2D Materials* 9.1 (Oct. 2021), p. 015002. ISSN: 2053-1583. DOI: 10.1088/2053-1583/ac2d15.

[55] Geun Ho Ahn et al. “Strain-engineered growth of two-dimensional materials”. en. In: *Nature Communications* 8.1 (Sept. 2017), p. 608. ISSN: 2041-1723. DOI: 10.1038/s41467-017-00516-5.

[56] Shrawan Roy, Jie Gao, and Xiaodong Yang. “Upconversion photoluminescence of monolayer WSe_2 with biaxial strain tuning”. EN. In: *Optics Express* 32.3 (Jan. 2024), pp. 3308–3315. ISSN: 1094-4087. DOI: 10.1364/OE.506243.

[57] Robert Oliva et al. “Strong Substrate Strain Effects in Multilayered WS2 Revealed by High-Pressure Optical Measurements”. In: *ACS Applied Materials & Interfaces* 14.17 (2022). PMID: 35442641, pp. 19857–19868. DOI: 10.1021/acsami.2c01726.

[58] Anubhav Jain et al. “The Materials Project: A materials genome approach to accelerating materials innovation”. In: *APL Materials* 1.1 (2013), p. 011002. ISSN: 2166532X. DOI: 10.1063/1.4812323.

[59] Alex M. Ganose, Adam J. Jackson, and David O. Scanlon. “sumo: Command-line tools for plotting and analysis of periodic *ab initio* calculations”. In: *Journal of Open Source Software* 3.28 (2018), p. 717. DOI: 10.21105/joss.00717.

[60] K. Kośmider, J. W. González, and J. Fernández-Rossier. “Large spin splitting in the conduction band of transition metal dichalcogenide monolayers”. In: *Phys. Rev. B* 88 (24 2013), p. 245436. DOI: 10.1103/PhysRevB.88.245436.

[61] Raj K. Sah et al. “Effect of strain on the band gap of monolayer MoS_2”. In: *Phys. Rev. B* 110 (14 2024), p. 144109. DOI: 10.1103/PhysRevB.110.144109.

[62] Aliaksandr V. Krukau et al. “Influence of the exchange screening parameter on the performance of screened hybrid functionals”. In: *The Journal of Chemical Physics* 125.22 (Dec. 2006), p. 224106. ISSN: 0021-9606. DOI: 10.1063/1.2404663.

[63] *HFRCUT – VASP Wiki*. The VASP Manual. Oct. 2023.

[64] W. H. Zachariasen. “Metallic radii and electron configurations of the $5f6d$ metals”. In: *Journal of Inorganic and Nuclear Chemistry* 35.10 (Oct. 1973), pp. 3487–3497. ISSN: 0022-1902. DOI: 10.1016/0022-1902(73)80357-4.

[65] F.R. Gamble. “Ionicity, atomic radii, and structure in the layered dichalcogenides of group IVb, Vb, and VIb transition metals”. In: *Journal of Solid State Chemistry* 9.4 (1974), pp. 358–367. ISSN: 0022-4596. DOI: 10.1016/0022-4596(74)90095-4.

[66] Xiangying Su et al. “Band gap modulation of transition-metal dichalcogenide MX2 nanosheets by in-plane strain”. In: *Physica E: Low-dimensional Systems and Nanostructures* 84 (2016), pp. 216–222. ISSN: 1386-9477. DOI: 10.1016/j.physe.2016.06.012.

[67] Ting Kang et al. “Strategies for Controlled Growth of Transition Metal Dichalcogenides by Chemical Vapor Deposition for Integrated Electronics”. In: *ACS Materials Au* 2.6 (2022), pp. 665–685. DOI: 10.1021/acsmaterialsau.2c00029.

[68] Matin Amani et al. “Growth-substrate induced performance degradation in chemically synthesized monolayer MoS2 field effect transistors”. In: *Applied Physics Letters* 104.20 (May 2014), p. 203506. ISSN: 0003-6951. DOI: 10.1063/1.4873680.

[69] Sung-June Baek et al. “Baseline correction using asymmetrically reweighted penalized least squares smoothing”. In: *Analyst* 140 (1 2015), pp. 250–257. DOI: 10.1039/C4AN01061B.

[70] John Kim. “Strain-Modulated Optical Properties of Monolayer Transition-Metal Dichalcogenide”. In: *Princeton University Library* (Apr. 2025).

[71] T. M. G. Mohiuddin et al. “Uniaxial strain in graphene by Raman spectroscopy: G peak splitting, Grüneisen parameters, and sample orientation”. In: *Phys. Rev. B* 79 (20 2009), p. 205433. DOI: 10.1103/PhysRevB.79.205433.

[72] Yunus Waheed et al. “Large trion binding energy in monolayer WS2 via strain-enhanced electron–phonon coupling”. In: *Communications Materials* 6.1 (Apr. 2025). Publisher: Nature Publishing Group, p. 86. ISSN: 2662-4443. DOI: 10.1038/s43246-025-00809-z.

[73] Ayse Berkdemir et al. “Identification of individual and few layers of WS2 using Raman Spectroscopy”. In: *Scientific Reports* 3.1 (Apr. 2013). Publisher: Nature Publishing Group, p. 1755. ISSN: 2045-2322. DOI: 10.1038/srep01755.

[74] Yalan Yan et al. “Tuning the physical properties of ultrathin transition-metal dichalcogenides via strain engineering”. In: *RSC Advances* 10.65 (Oct. 2020). Publisher: The Royal Society of Chemistry, pp. 39455–39467. ISSN: 2046-2069. DOI: 10.1039/D0RA07288E.

[75] Jae-Ung Lee et al. “Strain-shear coupling in bilayer MoS2”. In: *Nature Communications* 8.1 (Nov. 2017). Publisher: Nature Publishing Group, p. 1370. ISSN: 2041-1723. DOI: 10.1038/s41467-017-01487-3.

[76] Kathleen M. McCreary et al. “The Effect of Preparation Conditions on Raman and Photoluminescence of Monolayer WS2”. In: *Scientific Reports* 6.1 (Oct. 2016). Publisher: Nature Publishing Group, p. 35154. ISSN: 2045-2322. DOI: 10.1038/srep35154.

[77] Xiaotian Wang et al. “Effects of solvents and polymer on photoluminescence of transferred WS2 monolayers”. In: *Journal of Vacuum Science Technology B* 37.5 (Aug. 2019), p. 052902. ISSN: 2166-2746. DOI: 10.1116/1.5094543.

[78] John D. Porter, Michael P. Skinner, and Stephanie Simmons. "Polycarbonate-containing liquid chemical formulation and methods for making and using polycarbonate film". Pat. WO2001032764A1. May 2001.

[79] Delong Cui et al. "Enhanced Strain Modulation Efficiency in Two-Dimensional Materials via Optimal Annealing". In: *ACS Applied Nano Materials* 8.29 (2025), pp. 14811–14818. DOI: 10.1021/acsanm.5c02552.

[80] Saien Xie et al. "Coherent, atomically thin transition-metal dichalcogenide superlattices with engineered strain". In: *Science* 359.6380 (Mar. 2018), pp. 1131–1136. DOI: 10.1126/science.aao5360.

[81] Frank Ceballos et al. "Probing charge transfer excitons in a MoSe2–WS2 van der Waals heterostructure". In: *Nanoscale* 7.41 (Oct. 2015). Publisher: The Royal Society of Chemistry, pp. 17523–17528. ISSN: 2040-3372. DOI: 10.1039/C5NR04723D.

[82] Mingyuan Sheng et al. "Growth and Photoresponse of WS2/MoSe2 Lateral Heterostructure". In: *Advanced Electronic Materials* 10.8 (2024), p. 2300842. ISSN: 2199-160X. DOI: 10.1002/aelm.202300842.

[83] Neema Rafizadeh et al. "Type-I and type-II interfaces in a MoSe2/WS2 van der Waals heterostructure". In: *Applied Physics Letters* 126.4 (Jan. 2025), p. 042103. ISSN: 0003-6951. DOI: 10.1063/5.0253709.

[84] Jed Kistner-Morris et al. "Electric-field tunable Type-I to Type-II band alignment transition in MoSe2/WS2 heterobilayers". In: *Nature Communications* 15.1 (May 2024). Publisher: Nature Publishing Group, p. 4075. ISSN: 2041-1723. DOI: 10.1038/s41467-024-48321-1.

[85] Yuze Meng et al. "Electrical switching between exciton dissociation to exciton funneling in MoSe2/WS2 heterostructure". In: *Nature Communications* 11.1 (May 2020). Publisher: Nature Publishing Group, p. 2640. ISSN: 2041-1723. DOI: 10.1038/s41467-020-16419-x.

[86] Ze Wang et al. "Nonvolatile Memristor Based on WS2/WSe2 van der Waals Heterostructure with Tunable Interlayer Coupling". In: *Advanced Functional Materials* 35.32 (2025), p. 2501372. DOI: 10.1002/adfm.202501372.

[87] Miaomiao Liu et al. "2D TMD-Based Lateral Heterostructures: Preparation, Property, and Application". In: *Advanced Functional Materials* n/a.n/a (), p. 2500876. ISSN: 1616-3028. DOI: 10.1002/adfm.202500876.

[88] Zhengwei Zhang et al. "Robust epitaxial growth of two-dimensional heterostructures, multiheterostructures, and superlattices". In: *Science* 357.6353 (Aug. 2017). Publisher: American Association for the Advancement of Science, pp. 788–792. DOI: 10.1126/science.aan6814.

[89] Florence A. Nugera et al. “Bandgap Engineering in 2D Lateral Heterostructures of Transition Metal Dichalcogenides via Controlled Alloying”. In: *Small* 18.12 (2022), p. 2106600. ISSN: 1613-6829. DOI: 10.1002/smll.202106600.

[90] Nicola Marzari, Andrea Ferretti, and Chris Wolverton. “Electronic-structure methods for materials design”. In: *Nature Materials* 20.6 (June 2021). Publisher: Nature Publishing Group, pp. 736–749. ISSN: 1476-4660. DOI: 10.1038/s41563-021-01013-3.

[91] P. Hohenberg and W. Kohn. “Inhomogeneous Electron Gas”. In: *Physical Review* 136.3B (Nov. 1964), B864–B871. ISSN: 0031-899X. DOI: 10.1103/PhysRev.136.B864.

[92] W. Kohn and L. J. Sham. “Self-Consistent Equations Including Exchange and Correlation Effects”. In: *Physical Review* 140.4A (Nov. 1965), A1133–A1138. ISSN: 0031-899X. DOI: 10.1103/PhysRev.140.A1133.

[93] Matthias Ernzerhof and Gustavo E. Scuseria. “Assessment of the Perdew–Burke–Ernzerhof exchange-correlation functional”. In: *The Journal of Chemical Physics* 110.11 (Mar. 1999), pp. 5029–5036. ISSN: 0021-9606. DOI: 10.1063/1.478401.

[94] Pierpaolo Morgante and Roberto Peverati. “The devil in the details: A tutorial review on some undervalued aspects of density functional theory calculations”. In: *International Journal of Quantum Chemistry* 120.18 (2020), e26332. DOI: 10.1002/qua.26332.

[95] R.O. Jones. “Density functional theory: Its origins, rise to prominence, and future”. In: *Reviews of Modern Physics* 87.3 (Aug. 2015). Publisher: American Physical Society, pp. 897–923. DOI: 10.1103/RevModPhys.87.897.

[96] P. Geerlings, F. De Proft, and W. Langenaeker. “Conceptual Density Functional Theory”. In: *Chemical Reviews* 103.5 (May 2003), pp. 1793–1874. ISSN: 0009-2665, 1520-6890. DOI: 10.1021/cr990029p.